METAL OXIDE AND METAL NITRIDE NANOSTRUCTURES FOR LITHIUM-ION BATTERIES AND SUPERCAPACITORS

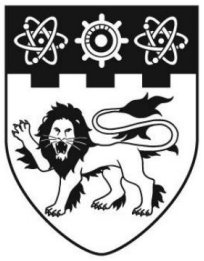

NANYANG TECHNOLOGICAL UNIVERSITY

METAL OXIDE AND METAL NITRIDE NANOSTRUCTURES FOR LITHIUM-ION BATTERIES AND SUPERCAPACITORS

ZHU CHANGRONG 2016

ZHU CHANGRONG

SCHOOL OF PHYSICAL AND MATHEMATICAL SCIENCES

2016

METAL OXIDE AND METAL NITRIDE NANOSTRUCTURES FOR LITHIUM-ION BATTERIES AND SUPERCAPACITORS

ZHU CHANGRONG

School of Physical and Mathematical Sciences

A thesis submitted to Nanyang Technological University

in fulfilment of the requirement for the degree of

Doctor of Philosophy

2016

ACKNOWLEDGEMENTS

"Nothing is impossible, impossible just takes longer time". This is the most suitable sentence to summarize my four-year PHD training. In this great journey, I grow from a bachelor who always follow the senior labmates to an independent PHD candidate who can fully complete a project in project analysis, experiment design/conduction, data collection and analyzing and manuscript drafting. For all my achievements, I would like to thank all the people that helped me.

I would like to express my deepest gratitude to my supervisor Prof. Fan Hong Jin and my co-supervisor Dr. Huang Hui. Under their guidance, I am very lucky to have several wonderful experiences publishing my work in high impact journals and won some amazing awards during the four years. They have been always supporting me and helping me out both in research work and in life. I feel so lucky to have both of them as my advisors during my PHD training. Both of them gave me great help on experiment design and data analysis. Prof. Fan is very patience helping revise my manuscript and even oral presentation slides. I am so blessed to have such a talented supervisor who is always willing to teach me step by step and boost my performance in all aspects. Dr. Huang always thinks good for me, whenever there is a chance, he would encourage me to achieve. I also learned a lot of communication skills and gained great confidence to lead a better life from them.

One of the greatest needs of human beings is a good companion. I feel so grateful to have so many wonderful labmates who always encourage me and help me. I would like to thank Dr. Xia Xinhui, Dr. Liu Monan, Dr. Li Xianglin, Dr. Luo Jingshan, Dr. Guan Cao, Dr. Xu Jing and Dr. Ku Zhiliang who had given me a lot of guidance in experiments. I also want to thank Mr. Yang Shancheng, Mr. Zhang Chiyuan, Dr. Gao Yuan and Mr. Li Zhengpeng for introducing me the physical training that makes me healthier and stronger. I especially thank all my friends around me for dragging me out when I want to give up.

I would like to thank all my collaborators Dr. Fan Zhanxi, Dr. Wang Xingli, Dr. Wang Xinghui, Mr. Zhang Xiao, Dr. Sun Jing, Mr. Yang Peihua for the great cooperation experience we have. Thank you all for opening my eyes.

Finally, my deepest gratitude goes to my husband Mr. Chao Dongliang and my parents. Thank you for loving me with your full heart and all the continuous support.

Table of Contents

Publications

1. Dongliang Chao, **Changrong Zhu**, Peihua Yang , Xinhui Xia , Jilei Liu , Jin Wang , Xiaofeng Fan , Serguei V. Savilov , Jianyi Lin , Hong Jin Fan, Ze Xiang Shen*, Array of Nanosheets Render Ultrafast and High Capacity Na-Ion Storage by Tunable Pseudocapacitance, ***Nat Commun*****,** Accepted
2. **Changrong Zhu**, Yanfeng Sun, Dongliang Chao, Xinghui Wang, Peihua Yang, Xiao Zhang, Hui Huang, Hua Zhang, and Hong Jin Fan*, A 2.0 V Capacitive Device Derived from Shape-Preserved Metal Nitride Nanorods, ***Nano Energy*****,** *26, 1-6 (2016)*
3. **Changrong Zhu**, Peihua Yang, Dongliang Chao, Xingli Wang, Xiao Zhang, Shi Chen, Tay, Beng Kang; Hui Huang; Hua Zhang, Wenjie Mai, Hong Jin Fan*, All Metal Nitrides Solid-State Asymmetric Wang, supercapacitors, ***Adv. Mater.*** *27, 4566-4571 (2015)*
4. Dongliang Chao, **Changrong Zhu**, Xinhui Xia, Jilei Liu, Xiao Zhang, Jin Wang, Pei Liang, Jianyi Lin, Hua Zhang, Zexiang Shen*; Hong Jin Fan*, Graphene Quantum Dots Coated VO2 Arrays for Highly Durable Electrodes for Li and Na Ion Batteries, ***Nano Lett****. 15, 565–573 (2015)*
5. **Changrong Zhu**, Peihua Yang, Dongliang Chao, Wenjie Mai, Hong Jin Fan*, Heterogeneous Nanostructures for Sodium Ion Batteries and Supercapacitors, ***Invited review***, ***ChemNanoMater*** *1, 458–476 (2015)*
6. **Changrong Zhu**, Dongliang Chao, Jing Sun, Bacho, Ignacio; Zhanxi Fan, Ng, Chin Fan; Xinhui Xia, Hui Huang, Hua Zhang, Zexiang Shen, Guqiao Ding*; Hong Jin Fan*, Enhanced Lithium Storage Performance of CuO Nanowires by Coatings of Graphene Quantum Dots, ***Adv. Mater. Interface*** *2, 1400499 (2015)*
7. Xinhui Xia, **Changrong Zhu**, Jingshan Luo, Zhiyuan Zeng, Cao Guan, Chin Fan Ng, Hua Zhang, and Hong Jin Fan*, Synthesis of Free-Standing Metal Sulfide Nanoarrays via Anion Exchange Reaction and Their Electrochemical Energy Storage Application, ***Small****, 10, 766-773, 2014*
8. **Changrong Zhu**, Xinhui Xia, Jilei Liu, Zhanxi Fan, Dongliang Chao, Hua Zhang, Hong Jin Fan*, TiO_2 nanotube@SnO_2 nanoflake core-branch arrays for lithium-ion battery anode, **Nano Energy** 4, 105-112, 2014
9. Dongliang Chao, Xinhui Xia, **Changrong Zhu**, Jin Wang, Jilei Liu, Jianyi Lin, Zexiang Shen*, and Hong Jin Fan*, Hollow Nickel Nanocorn Arrays as Three-Dimensional and Conductive Support for Metal Oxides to Boost Supercapacitive Performance, ***Nanocale*** *6, 5691-5697, 2014*

10. Huanwen Wang, Huan Yi, **Changrong Zhu**, Xuefeng Wang*, Hong Jin Fan*, Functionalized Highly Porous Graphitic Carbon Fibers for High-Rate Supercapacitive Electrodes*, **Nano Energy** 13, 658-669 2015*
11. Peihua Yang, Dongliang Chao, **Changrong Zhu**, Xinhui Xia, Yongqi Zhang, Xingli Wang, Peng Sun, Beng Kang Tay, Ze Xiang Shen, Wenjie Mai* and Hong Jin Fan*, Ultrafast-Charging Supercapacitors Based on Corn-Like Titanium Nitride Nanostructures, ***Advanced science**,* DOI: 10.1002/advs.201500299

Chapter 1 Background and Literature Survey

1.1 Introduction to nanostructured electrode materials

In the past two decades, sustainable clean energy resources have attracted great research attention with the promise of providing a better living environment as well as leaving more energy resources to the descendants to survive.[1, 2] Regarding the research of green energy devices, material scientists have put huge amount of efforts on searching for better electrode materials for lithium ion batteries and supercapacitors.[3, 4] To reach the best performance of a specific material, nanofabrication exhibits high efficiency in boosting electrode material properties due to the conclusion that at the nanoscale, materials can show surprisingly good properties such as high electrochemical conductivity,[5, 6] large surface area to volume ratio,[7] superb solubility[8] and mobility[9] as well as highly reaction activity.[4] Researchers even concluded that nano-manufacture sometimes even makes a material motivated to cooperate with other materials resulting in some amazing synergic effects.[3, 5, 7] Compared with compact materials, nanostructured materials mainly benefit the device performances in the following aspects: 1) Secure a larger surface area.[3, 7] Compared to bulk materials, nanostructured materials can provide more active points where electrochemical reactions happen and deliver the specific energy and power. As well, bigger surface area increases the contact between electrode materials and electrolyte or current collector. In both cases, the escalatory connection spots ensure more active ion and electron transportation paths which will lead to higher reaction efficiency and better electrochemical properties such as ultra-fast rate capability, specific power density, high coulombic efficiency as well as long cyclability. 2) Shorten the ion/electron diffusion length.[5, 6] Nanostructures with hierarchical intercalations between active materials or with both electrolyte and the current collector make the ions and electrons more easily to be transferred. Fast ion movements between active material and electrolyte

guarantees continuous electrochemical reactions and ion release and intake. Fluent electron transferring to the current collector insures the whole device efficiency for energy storage and release processes. These in return will lower the electrochemical impedance. 3) Enhance the electrode ability to accommodate ions. Special nanoarchitecture can release the strain of ions insertion/removal thus improve cycle life. 4) Enables the impossible reaction with bulk or micro-sized materials happen.[4, 7, 8] This point opens more potential for a specific material and motivated the fully usage of resources in the world. 5) Make the composition, size and structure of electrode material more controllable.[3, 5, 6] In nano-manufacturing, one can change the morphology and diameter/length/width/thickness of electrode materials by simply adjusting the reaction conditions (source material type/concentration; reaction temperature, time duration, pressure, step order, dealing gas, temperature ramping/cooling time et al.). These uncertainties are actually potential possibilities of a singular material making research full of challenging as well as promising.

When goes to nanoscale, varies types of nanostructures have been made and each of them have special optimized properties tightly related to the structure. To have an integral understanding of the entire area, we are going to discuss the nanostructured materials by classifying them to different dimensions. Furthermore, the typical synthesis methods will be discussed in the following parts.

1.1.1 Nanostructures: From 0 to 3 Dimensions

Though there is no standard classification about the dimensions of nanomaterials, but according to the size and morphology, we summarized the nanomaterials into zero dimensional (0 D), one dimensional (1 D), two dimensional (2 D) and three dimensional (3 D) and listed their typical representatives in Figure 1.1.1.

Nanoparticles and quantum dots are typical 0 D nanostructures since they are spherical structure with each dimension beneath 100 nm. 0 D nanostructures would normally benefit material performance due to the high surface area and structure tenability. 0 D nanostructures can be solid particle, hollow particle and even core-shell

homocentric sphere structure. Moreover, by tuning its surface, pores with suitable size can be added according to the application requirements. Examples of 0 D nanostructure materials application in both supercapacitors (silver nanoparticle,[10] NiO nanoparticle,[11] MnO_2 nanoparticle[12] and Fe_2N nanoparticle[13]) and lithium-ion batteries (Si nanoparticle and Si carbon nanoparticle composites[14, 15]) have been given, which proved the advantages of materials in this dimension.

Due to the direct ion/electron transportation pathway along its longitudinal axis direction, 1 D structures were widely studied in designing free standing electrode materials. Typical morphologies are nanorods, nanowires, nanotubes, and nanobelts. The difference between nanorod and nanowire is their ratio of diameter against length. Nanorods are usually short rods (short that 500 nm) with comparably higher ratio of diameter against length while nanowire is wire with length longer than 1 μm. To differentiate nanobelt from nanowire, AFM (atomic force microscope) is usually used to figure out the thickness and the diameter. If the thickness is of the similar size with the diameter, the structure can be considered as nanowire while when the thickness is much less than the diameter, the structure should be called nanobelt. Nanotube is hollow structure which is light compared to nanorod structure and should be considered a suitable backbone structure when constructing core-shell material. Due to the exposure of 1 D nanostructures surface, they are always preferred as core structure to be decorated by 0 D materials and 2 D flakes.

Two dimensional structure (2 D) can be defined as structure that with a few atomic layer thickness and other two dimensions beyond the nanometric size range such as nanosheet, nanowall and nanoflake. These three types of 2 D nanostructures can be differentiated from its width. Normally, nanosheet has the width at micrometer scale such as graphene and MoS_2. Nanoflake is with thinner thickness than that of nanowall and in both cases, the width is beneath 1 μm. These structures usually possess high surface area which is favorable as a supercapacitor electrode material and is able to be decorated with tiny dots to form heterogeneous nanocomposites electrode.

Three dimensional structure (3 D) nanomaterials show different size at each

dimensional and are usually special structures such as nano-flower, nano-honeycomb and nano-star. Those structures have stretched out towards three axises. Three dimensional structure can also be formed by the combination of 1 D and 2 D nanostructures, for instance, TiO_2 nanotube-SnO_2 nanoflake core-shell structure.[16]

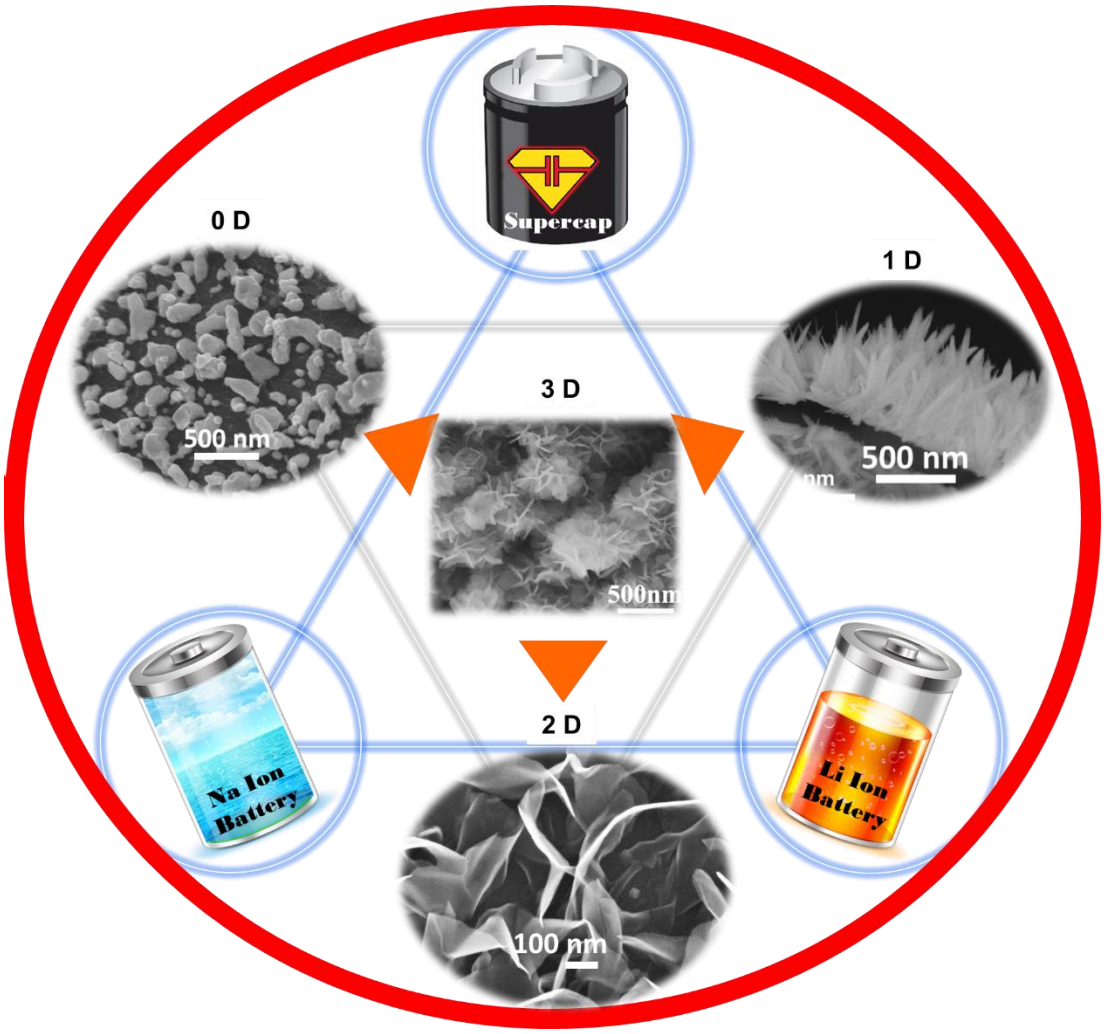

Figure 1.1.1 Represents of nanostructure materials with different dimensions and there applications in Lithium/sodium-ion batteries and supercapacitor.

1.1.2 Synthesis methods for nanostructured electrode materials

Regarding the synthesis methods, there are mainly three types: chemical, physical and electrochemical methods. This thesis will focus on chemical and electrochemical fabrication methods.

Typical chemical synthesis methods in nanofabrication are hydrothermal, solvothermal, chemical bath deposition and microwave processing. Hydrothermal, solvothermal and microwave processing share the same working mechanism in which the source materials start to decompose or react with each other when the vessel reaches the suitable temperature and pressure. The vessel has to be kept in the same react condition for a specific period of duration to obtain the designed crystal structure or morphology. In a hydrothermal synthesis process, preparations need to be done including: preparing solution, clean autoclaves and set electric oven. It can be used to grow powder materials as well as free standing electrode materials. For synthesis of free standing electrode materials, a holder is usually needed to support the substrate to control the exact position of the substrate in the autoclave. Important parameters in the hydrothermal fabrication process includes: temperature (depending on the electric oven), pressure (determined by the conditions of autoclave and the volume and amount of solution applied), the homogeneity of the temperature in the electric oven and the position of autoclaves in the electric oven. The advantage of hydrothermal synthesis is the that it is able to fabricate numerous kinds of metal oxides, sulfides and nitrides. By tuning the reaction temperature, pressure and time, one is able to control the morphology and size of the nanomaterial. Moreover, the hydrothermal synthesis is simple and low cost compared to other chemical methods.

The solvothermal synthesis is quite similar to hydrothermal synthesis. The difference is their source materials in the solution. In a solvothermal synthesis process, the precursor solution is usually not aqueous. The advantage of the solvothermal synthesis is the ability to precisely control the crystallinity, size, morphology and shape distribution of the metal oxide electrode materials. Through changing certain experimental parameters for instance, the solvent type, reaction temperature, time, surfactant and precursor type, it is able to alter the morphology and size of the nanomaterials.

Microwave processing is also similar to hydrothermal reaction but exhibit superiority as follows: First, the heat is more centralized on the vessel which makes the

heating more efficient. As a result, the synthesized material has better homogeneity. Moreover, because of this heating mode, the reaction time can be largely shortened. For instance, a 12 h hydrothermal synthesis process can be usually equally finished in a microwave within 1 h. In most cases, the latter can achieve higher mass loading due to the centralized heating. Second, the microwave can do more parallel fabrication study in one trial because it has more than 12 vessels that can be conducted together. This can facilitate the the recipe exploring process when start a new synthesis project. Besides, it is able to synthesis more samples in a singular trial, highly increase the work efficiency. Finally, the vessels used in microwave processing are usually quartz silica glass which can stand higher reaction temperature than the Teflon-autoclaves (limited to beneath 200 ^{o}C). Furthermore, the quartz silica glass vessels can get rid of most of the contaminations making them easier to clean while the Teflon-autoclaves are easy to be contaminated and may need nitrohydrochloric acid to clean.

Chemical bath deposition (CBD) method is easy to handle and suitable for making big electrodes. Taking $Ni(OH)_2$ for example, $Ni(OH)_2$ nanowall can be fabricated onto the Ni foam substrate in a short (10 mins) chemical bath deposition synthesis (Figure 1.1.2) process. Detailed steps are: first, a 500 ml beaker was washed and dried before use; second, the cleaned Ni substrate (10×24 cm^2) was pasted to the wall of the beaker with double-side tape; third, the reaction solution which consisted of 5 mM Ni_2SO4 and 20 mM $Na_2S_2O_8$ were resolved in 100 ml distilled water and stirred with magnetic stir at room temperature; finally, 5 ml ammonia solution was added to the beaker and stirred for another 10 mins till the final formation of the as synthesized $Ni(OH)_2$ nanowall on the substrate. This method is simple and in principle can be used for large scale fabrication when the bigger container and magnetic stirring can be realized.

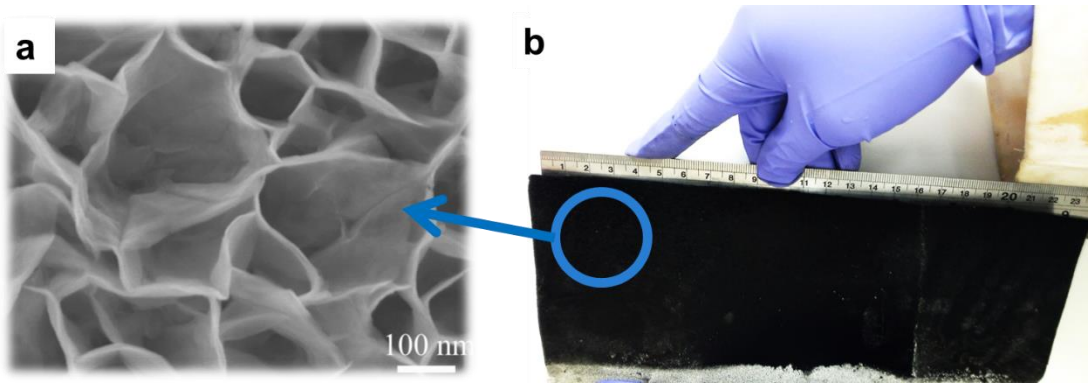

Figure 1.1.2 Synthesis of $Ni(OH)_2$ nanowall on Ni foam through chemical bath deposition process. a) SEM image of as synthesized $Ni(OH)_2$ nanowall. b) Real photo of $Ni(OH)_2$ nanowall grown on Ni foam substrate with a length ~ 24 cm and width ~ 10 cm.

All these synthesis methods are developed based on the requirements of different energy storage applications. Parameters of reactions can be tuned to satisfy different systems. In the following parts, we will mainly focus on lithium-ion batteries and supercapacitors and we will start with some basic introduction to these two types of energy storage systems.

1.2 Introduction to Lithium-ion batteries

Tracing back to the very beginning of lithium battery research, the first commercially available lithium battery was created in early 1970s after the pioneer work done by G.N. Lewis in 1912. Due to the intrinsic properties of Li (lowest in density, providing largest energy density over weight and high electrochemical potential), great efforts have been input in developing rechargeable lithium batteries. However, the instability of Li metal caused the charging safety problems and stops the battery to be rechargeable. Unlike Li metal, lithium ions exhibit high safety property although the energy density is slightly lower. Thus, researchers began to substitute the Li metal to lithium ions and shifted to the non-metallic lithium battery research. In 1991, the first lithium-ion battery was commercialized by Sony Corporation. Afterwards, rechargeable lithium-ion battery became the hot research topic since then and have

lasted for more than two decades. To have a direct view of the LIB against traditional rechargeable batteries, we list the important parameters in the Table 1.2.1 as follows:

Table 1.2.1 Properties comparison of LIB with traditional batteries. (data from http://batteryuniversity.com/learn/article/secondary_batteries)

Types / Contents	Lead-Acid	NiCd	NiMH	LIB		
				Co	Mn	Phosphate
Working voltage (V)	2	1.2	1.2	3.6	3.7	3.2 ~ 3.3
Energy density (Wh/kg)	30 ~ 50	45 ~ 80	60 ~ 120	150 ~ 250	100 ~ 150	90 ~ 120
Cycle life (80% DoD)	200 ~ 300	1000	300 ~ 500	500 ~ 1000	500 ~ 1000	1000 ~ 2000
Charge time (h)	8 ~ 16	1 ~ 2	2 ~ 4	2 ~ 4	2 ~ 4	1 ~ 2
Charge temperature (^{o}C)	-20 ~ 50	0 ~ 45		0 ~ 45		
Discharge temperature (^{o}C)	-20 ~ 50	-20 ~ 65		-20 ~ 60		
Coulombic efficiency	~ 90	~ 70 % slow charge ~ 90 % fast charge		~ 99		
Cost	Low	Moderate		High		
Toxicity	Very high	Very high	Low	Low		
Maintenance requirement	3 ~ 6 months	Full discharge every 90 days		Maintenance-free		
In use since	Late 1800s	1950	1990	1991	1995	1999

Charge cut off voltage (V/cell)	2.4	Full charge detection by voltage signature	4.2	3.6
Discharge cut off voltage (V/cell)	1.75	1.0	2.5 ~ 3.0	2.5

As can be seen clearly from the table 1.2.1, the working voltage of LIB is about twice than that of the standard NiCd battery and the energy density of LIB is twice of NiCd battery, which means nickel-based pack would require three 1.2-volt cells to be connected in series to satisfy the normal usage while with LIB one cell is enough to provide the required voltage and energy. Besides, LIB is a maintenance-free system which greatly lowered the cost of the battery usage. In addition, the self-discharge of LIB is much less than NiCd battery because of the solid-electrolyte-interface (SEI) layer, making it well suited for modern fuel gauge applications. Furthermore, LIB cells are easy to dispose and have less harm to the environment. However, LIB have some disadvantages as well. The aging and capacity deterioration problems are noticeable while the manufacturers stated that the LIB should be stored in a cool place to slow the aging and capacity fading.

To well understand the LIB and figure out the improvement space in this area, we summarized the advantages and disadvantages of the LIB as follows. Advantages: High energy density - potential for yet higher capacities; Does not need prolonged priming when new. One regular charge is all that's needed; Relatively low self-discharge - self-discharge is less than half that of nickel-based batteries; Low Maintenance - no periodic discharge is needed; there is no memory; Specialty cells can provide very high current to applications such as power tools. Disadvantages: Requires protection circuit to maintain voltage and current within safe limits; Subject to aging, even if not in use - storage in a cool place at 40% charge reduces the aging effect; Transportation restrictions - shipment of larger quantities may be subject to regulatory control;

Expensive to manufacture - about 40 percent higher in cost than nickel-cadmium; Not fully mature - metals and chemicals are changing on a continuing basis.

1.2.1 Cell configuration and working mechanism

The basic components of a LIB cell are current collector, anode, separator, cathode and electrolyte. Current collector is used to collect electrons from the active material during the battery charge discharge process. Regarding current collector materials, requirements are as follows: first, high conductivity. To secure fast energy delivering and low internal energy consuming, the current collector should have low electronic resistance, thus high conductivity always come the first. Second, high stability in battery electrolyte under different voltage range. For anode current collector materials, it should be stable in 0 ~ 3 V voltage range while that for a cathode current collector should be 1 ~ 5 V normally regarding to different battery design requirements. Recently, the most common anode current collector is Cu foil and Al foil for a cathode current collector. Other anode current collector materials can be Ni foam/foil, titanium plate, stainless steel plate, carbon based substrates such as carbon fiber and graphene foam. Anode and cathode materials will be discussed in the 1.2.3. Separator is used to separate the anode from the cathode in case of short cut. The separator should allow for a fast ion penetration and transportation as well as good sustainability. During battery cycling, Li metal tends to have dendrite growth and will impale through the separator to cause the cell failure resulting in short cut and even explosion. The mostly used separator is commercialized polymer such as polypropylene (PP) film (Cellgard 2400).

Regarding electrolytes, the traditional electrolyte consists of $LiPF_6$ dissolved in ethylene carbonate (EC)–dimethyl carbonate (DME) (1:1 in volume) electrolytes. The organic electrolytes though allow for the usage of Li foil and can sustain high working voltage (up to 5 V), the toxic property makes it difficult to dismiss after use. Thus recently more and more researchers are attracted to exploring aqueous electrolytes that can sustain high working voltage. Researchers have reported the applying of highly concentrated aqueous electrolyte that can sustain the voltage up to 3.0 V.[17]

To explain the battery working mechanisms, we drafted the illustration figures as follows in Figure 1.2.1:

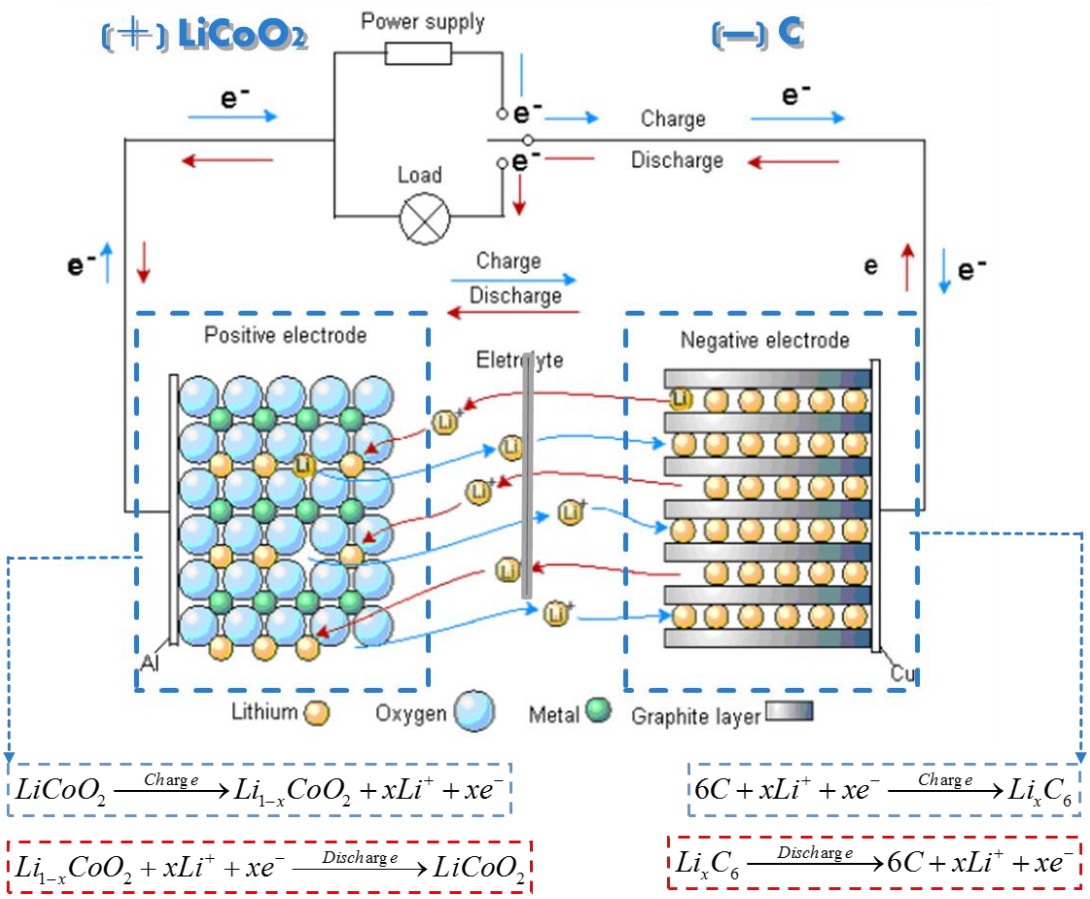

Figure 1.2.1. Cell configuration and working mechanism demonstration of lithium-ion battery

Taking TiO_2 as example to demonstrate the half-cell working process:

$$\chi Li^+ + TiO_2 + \chi e^- \leftrightarrow Li_\chi TiO_2 \quad (0 \leq \chi \leq 1)$$

When discharge, Li^+ moves towards the TiO_2 side through the separator to insert into the TiO_2 lattice and form the final $Li_\chi TiO_2$ ($0 \leq \chi \leq 1$) and deliver energy as well. When charge, Li^+ moves the opposite ways to store energy.

1.2.2 Parameters of LIB evaluation

To evaluate the performance of a lithium-ion battery cell, parameters should be

considered such as energy density, power density, working voltage, cyclic voltammetry (polarization information), rate performance, cycling performance, charge-discharge property, self-discharge and safety (under different temperature and pressure).

Before battery test, the anode, cathode, separator and electrolyte are always assembled in glovebox which has extreme low content of O_2 and H_2O. The coin cell or other types of cell configurations will be taken out after being thoroughly sealed. A multi-meter is usually used to test the open circuit voltage of the cell to determine whether the as assembled cells are worth to be tested or not. The good cells would be standing overnight before any test to allow the electrolyte merged thoroughly to the electrodes and separator. First test will be the cyclic voltammetry (CV) test to figure out the exact working potential for the battery and possible cathodic and anodic peak locations. The mostly tried scan speed for battery system is 0.2 mV s^{-1}. In the first cycle, sharp peaks of polarization are usually noticed which will disappear after first three cycles. During charge-discharge test, different current density will be tried with reference to the theoretical capacity to define the 1 C. Rate performance will be studied began with the ~ 0.1 C and increased up to 100 C and go back to 0.1 C to figure out the charge reaction of electrode materials towards current density variation. Cycling performance test will be conducted to thousand times at moderate current density to establish the sustainability and lifespan of the battery. Energy density and power density will be calculated based on the capacity and working voltage data.

1.2.3 LIB electrode materials

Regarding the lithium ion battery materials, there are mainly three types classified according to the reaction mechanisms: intercalation, conversion and alloying (see Figure 1.2.2). Intercalation is the reversible insertion and extraction of lithium ions into the host anode material matrix. Typical intercalation typed anode materials are TiO_2, VO_x (V_2O_5, VO_2, V_6O_{13}, LiV_3O_8), $Li_4Ti_5O_{12}$, $LiTi_2O_4$, $LiCrTiO_4$, $TiNb_2O_7$, $SrLi_2Ti_6O_{14}$, $Li_3Nd_3W_2O_{12}$, $LiTi_2(PO_4)_3$, $Li_3V_2(PO_4)_3$, $LiVPO_4F$, TiS_2. Compared to graphite, the

intercalation type materials exhibit advantages of high power density, no solvent co-intercalation, no SEI required for the safe operation of the cell, no electrolyte decomposition, and easy to synthesis.

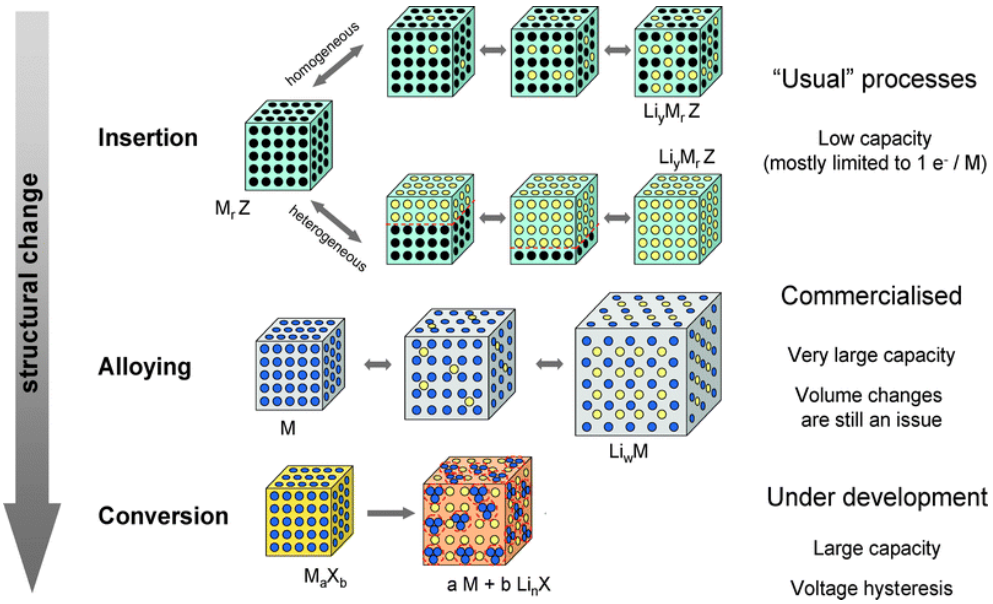

Figure 1.2.2. Three typical reaction mechanisms for lithium ion batteries.[18]

Alloying type anode materials will allow the insertion/extraction of Li into the crystal structure of the anode material lattice and the lithium ions are added to the reactant phase. The reaction equation can be described as:

$$Li + xM \Leftrightarrow LiMx$$

Where the reactant M can be an element or a compound and depending on whether or not a phase transformation takes place, these reactions can be further divided into two types as: first, solid-solution reaction. In a solid-solution reaction, no phase or structure change occurs in the reactant M when Li enters into its framework structure (that is a topotactic reaction); Second, addition reaction. In an addition reaction the phase structure of the lithiated LiMx is different from the parent phase M; thus, the reaction involves phase change from M to LiMx. Li insertion/extraction in crystalline

Si, Sn, Al and Sb are considered as addition reactions because of the very limited solubility of lithium in these elements. The reactions of Li with Mg and amorphous Si are regarded as solid-solution reactions. The purpose of using compound alloys is to create a Li-insertion host that maintains a strong structural relationship with the intermediate and the lithiated phases to minimize the volume expansion during reaction. The voltage curves of smaller alloy particles tend to be round-shaped. Alloy anodes have been considered as one of the most promising electrode materials for next-generation lithium-ion batteries due to their high energy densities, relatively low cost, environmental compatibility and safe operation potentials. The disadvantages of alloy anodes include their short cycle life and high irreversible capacity loss as a result of the large volume expansion during lithium insertion. Alloying active elements with inactive elements can reduce volume expansion, leading to improved cycle life and it also maximize the energy density. Typical alloying typed anodes are Si, Sn, Ge and their related derivatives. The biggest problem among this typed anode is the huge volume variates during the lithiation and delithiation process which will cause serious failure of the electrode because of the pulverization of the anode. Methods have been tried with created carbon matrix/encapsulates to protect the entire electrode.

Conversion reactions are lithiation reactions in which the active material is fully reduced by lithium to the metal according to the following equation

$$Mz+Ny + zLi \rightarrow M^0 + yLiz/yN$$

where M stands for a cation and N for an anion. When discharged, the conversion reaction anodes such as metal oxide (MOx) react with Li+ ions and form metal nano-domains (M^0) dispersed in the Li_2O matrix. Then, during charging steps, the M^0 and Li_2O components are converted into the metal oxide (MOx). In conversion mechanism, decomposition and formation process takes place. Typical conversion typed anode materials are Fe_2O_3, Fe_3O_4, CuO, MnO, Mn_2O_3, CoO, Co_3O_4, FeS, MoS_2. These types anode material have multiple electron reactions with Li^+, thus are able to deliver higher reversible capacity than insertion-typed materials. However, the unavoidable

electrolyte decomposition usually occurs at the first cycle which leads to the formation of a SEI layer on the surface of the active particle (predominantly composed of insoluble inorganic by products, polymeric films, etc.). In sequence, there will be a huge irreversible capacity loss at the first cycle. Worse still, the large volume expansion and higher redox potential will result in the poor cycle-ability. Researchers try to alleviate the issue by coating carbon materials or forming composites with carbonaceous material or other structural stable materials. Though, the problem cannot be solved thoroughly, those previous trial expressed some achievement in enhancing the anode performance.

1.3 From Lithium-ion batteries to Supercapacitors

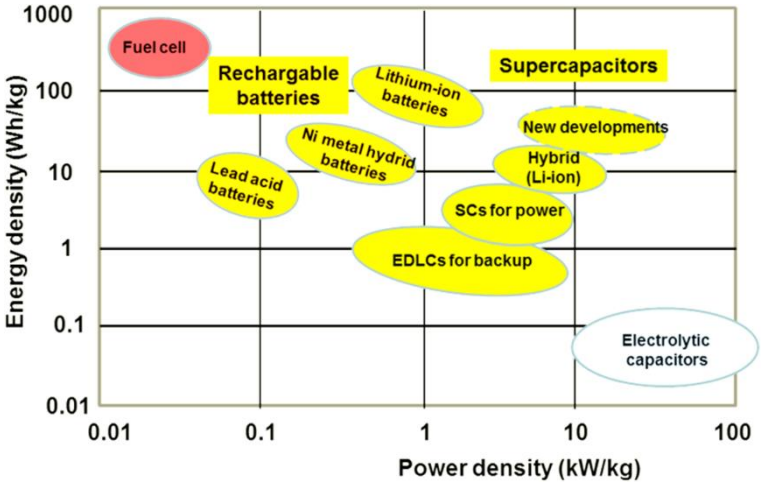

Figure 1.3.1. Ragone plot of different energy storage devices (data from Wikimedia commons: https://commons.wikimedia.org/wiki/File:Supercapacitors-vs-batteries-chart.png)

Supercapacitors are devices that store electrical energy in two dominating mechanisms: the charge accumulation on electrode material surface and fast redox reactions or rapid intercalation processes on electrode material. The energy density (Wh/kg) against power density (kW/kg) as defined Ragone plot of different energy storage devices was listed in Figure 1.3.1 and table 1.3.1. As can be seen, Supercapacitors exhibit much higher power density than battery systems. Moreover, supercapacitors expressed the possibility to reach high energy density as high as lithium

ion battery. Still, supercapacitor needs shorter time to be charge as short as few seconds while lithium ion batteries need hours to be charged.[19-24] With fast energy delivering property, supercapacitors express wide applications potential in areas of electrical vehicles, wind, solar and tide energies.

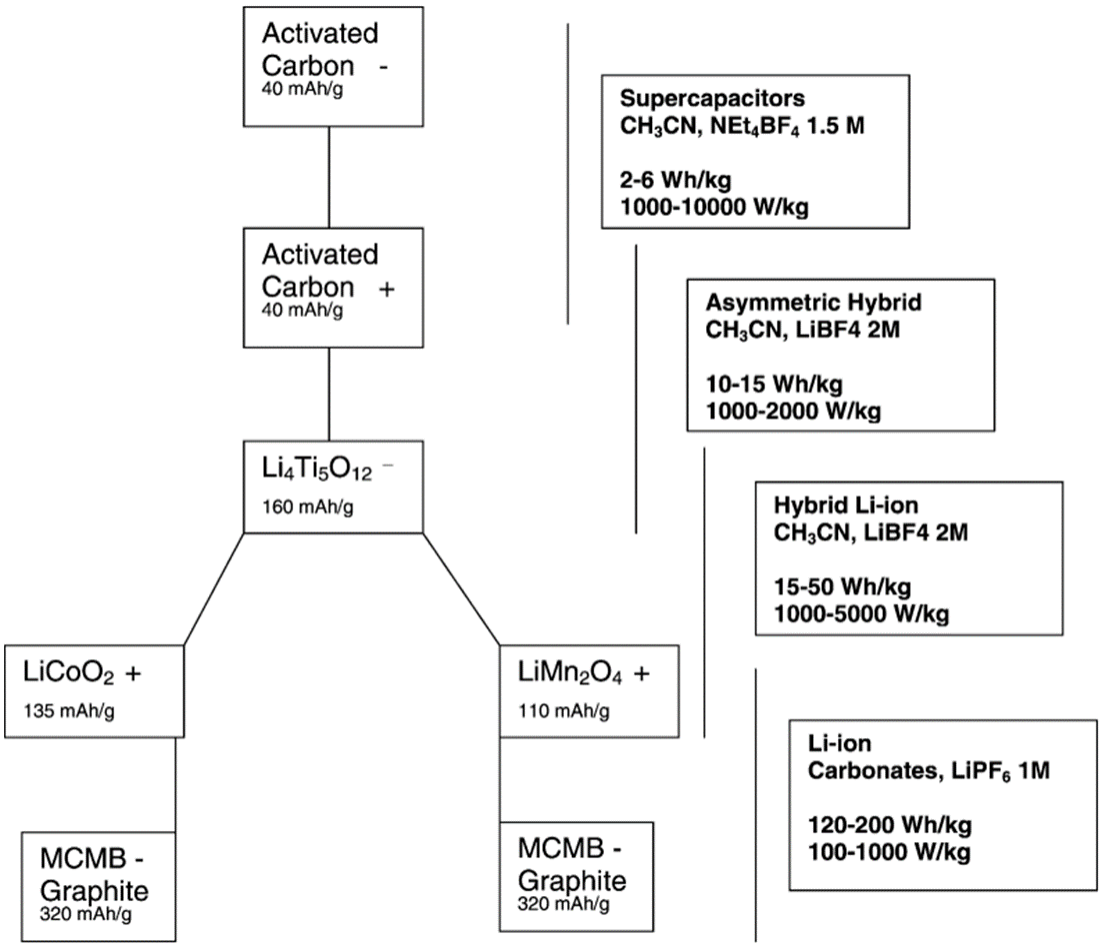

Figure 1.3.2. Summary of the typical components used in industry energy storage devices. Copy right 2003, Elsevier.[25]

The major difference that leads to the different charge storage properties of supercapacitor and lithium ion battery is the electrochemical processes occurring during charge-discharge process. In supercapacitors, the charges are stored on the electrode surface in a fast physical adsorption and or surface redox reaction process not like batteries where the charges come from the chemical reactions.

Through electrochemical measurements, such as potentiostatic and galvanostatic methods, the battery behavior and pseudo-capacitance behavior can be differentiated. If the CV curves are standard rectangle shape, normally, the majority

capacitance/capacity should be EDLC plus surface redox reaction while when there are peaks in CV curves or the CV curves are not standard rectangular shape, there should be ion diffusion controlled process. Regarding the charge-discharge curves, when the curves are standard triangular shape, it means that the capacitance are mainly EDLC and pseudo-capacitance, otherwise there should be ion-diffusion behavior. When EDLCs and pseudo-capacitance are dominant, the current response to potential change will be very rapid resulting in high power density and high rate performance while the ion-diffusion controlled behavior will lower the power density though contributes more to the capacitance.[19] Dunn *et al*. presented the method to calculate the exact capacitance contribution ratio from EDLC plus pseudo-capacitance and the ion-diffusion controlled process based on the research of Nb_2O_5.[26, 27] It is demonstrated that pseudo-capacitive materials can achieve battery-level energy density together with high power density. The promising potential makes the research of oxide typed supercapacitors meaningful.[28]

Table 1.3.1 Key parameters comparison between supercapacitor lithium-ion battery (data from: http://batteryuniversity.com)

Devices / Parameters	Lithium-ion battery	Supercapacitor (EDLC)
Cycle life	500 ~ 1000	1 million
Cell voltage	3.6 V	2.3 ~ 2.75 V
Charge time	1 ~ 2 h	1 ~ 10 seconds
Specific energy (Wh/kg)	120 ~ 240	5 ~ 50
Specific power (kW/kg)	1 ~ 3	Up to 10
Lifespan	5 ~ 10 years	10 ~ 15 years
Cost ($/kWh)	250 ~ 1000	10000

1.4 Introduction to Supercapacitors

The supercapacitor, also known as electrochemical capacitor inhibits the fast energy delivering property of traditional capacitor but differs from it with much higher capacitance. When a voltage differential is applied between the cathode and anode

plates, cations and anions will be absorbed and separated to anode and cathode respectively to store energy by means of a static charge as been called the EDLCs (electrical-double-layer capacitances). Meanwhile, in a supercapacitor, fast redox reductions will also happen on the electrode surface and this is the majority contribution to the entire capacitance as was called pseudo-capacitance.

Tracking down to the research history of supercapacitors, the first supercapacitor was made in 1957, but for a long time, there were no known reported commercialized applications of supercapacitors. Important progress was made in 1966 when the double-layer capacitor was noticed by accident and the double-layer greatly improved the charge storage ability. Then the supercapacitor was used as computer memory backup in 1978. It was not until the 1990s that marvelous efforts and improvement have been made towards supercapacitors when the energy resources research become hot.

In recent years, though numerous new types of supercapacitor electrode materials have been developed to achieve higher energy density, the mostly stable and commercialized electrode materials are carbon-based materials. Other typed electrode materials will be discussed in 1.4.3.

As was clearly noticed from the 1.3 part, the supercapacitor is not comparable to lithium-ion batteries on cell working voltage and energy density. According to the energy density equation $E = ½ CU^2$, the working potential is key to increase the energy density. Thus efforts have been made towards electrolyte,[17] electrode materials[29] and membrane. All capacitors have voltage limits. While the electrostatic capacitor can be made to withstand high volts, the supercapacitor is confined to 2.5 ~ 2.7 V. Voltages of 2.8V and higher are possible, but at a reduce service life. To get higher voltages, several supercapacitors are connected in series. Serial connection reduces the total capacitance and increases the internal resistance. Strings of more than three capacitors require voltage balancing to prevent any cell from going into over-voltage. Lithium-ion batteries share a similar protection circuit.

The specific energy of the supercapacitor ranges from 1 ~ 30 Wh/kg, which is 10 ~ 50 times less than Li-ion batteries. The discharge curve is another disadvantage.

Whereas the electrochemical battery delivers a steady voltage in the usable power band, the voltage of the supercapacitor decreases on a linear scale, reducing the usable power spectrum. Take a 6V power source that is allowed to discharge to 4.5V before the equipment cuts off. With the linear discharge, the supercapacitor reaches this voltage threshold within the first quarter of the cycle and the remaining three-quarters of the energy reserve become unusable. An optional DC-DC converter helps to recover the energy dwelling in the low voltage band, but this adds costs and introduces loss. A battery with a flat discharge curve, in comparison, delivers 90 to 95 percent of its energy reserve before reaching the voltage threshold.

In the following part, we will explain the detailed working mechanisms of supercapacitor, parameters to evaluate a supercapacitor device and supercapacitor electrode materials.

1.4.1 Device configuration and working mechanism

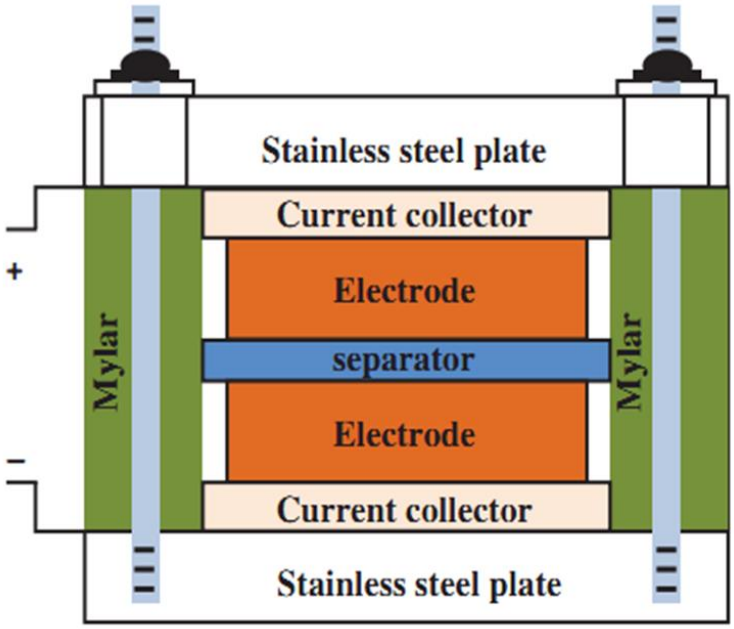

Figure 1.4.1. Cell configuration of supercapacitor device. Copyright Taylor and Francis Group, 2012.

A typical supercapacitor device is shown in figure 1.4.1.[30] The basic components are similar to a battery: the electrodes, separator, electrolyte and current collectors. Due to the relatively lower working voltage, the current collector which can act as the substrate do not need to sustain high voltage thus more substrate can be used as current collectors. In most circumstances, the electrolyte used in the supercapacitors are aqueous-based, thus the membrane normally used is the glass fiber based membrane. Before going to the discussion of electrode material designing, the working mechanism of supercapacitor should be figured out. As was discussed in the former part, there are mainly two types of capacitance contributions: first, the electro-double-layer-capacitance (EDLCs); second is the pseudo-capacitance.

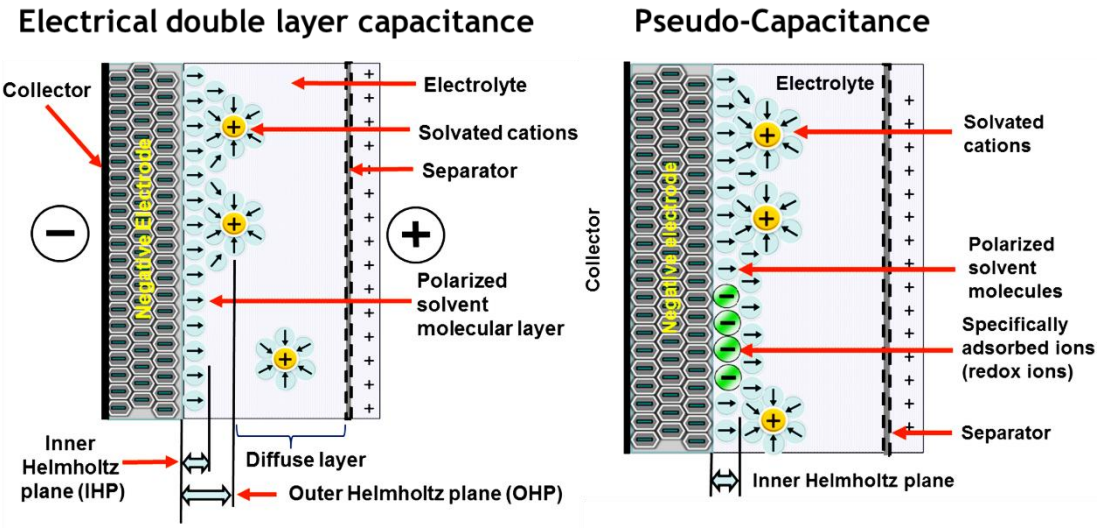

Figure 1.4.2. Illustration for the EDLC and Pseudo-capacitance processes in supercapacitor. Copyright Royal Society of Chemistry, 2009.[31]

In a supercapacitor system, the surface areas of the electrode are usually modified which would be much increased than the limited charge storage areas in conventional capacitors. Besides, the distance between the two charged plates can be largely lowered unlike in the traditional supercapacitors where the existed geometric constrains always limit the distance that two electrodes can be close. The large interfacial area and the atomic range of charge separation distances are two major reasons that supercapacitors based on the EDLC mechanism can store much charges than the conventional capacitor.

Regarding the EDLC mechanisms, several types of the working process were developed during the past two decades. As schematically illustrated in Figure 1.4.2, the first EDLC model is built by von Helmholtz in the 19th century, where the opposite ions are absorbed by the related electrode to form the electrode/electrolyte interface and are separated by an atomic distance which is very similar to the two-plate conventional capacitors.[32] This simple Helmholtz EDLC model was built under an ideal situation where the ions in the solution will not affect the double layer. Thus further modification was made by Gouy and Chapman,[33, 34] on consideration of the real electrolyte solution where there should be a continuous distribution of electrolyte ions. They added a thermal driven layer near the electro-double layer however, the Gouy–Chapman model will lead to overestimated capacitance because the capacitance of two separated arrays of charges increases inversely along the separation distance. Actually, there will be a very large capacitance value arising close to the electrode surface. To revise the model, Stern[35] combined the two modes together to confirm the two regions of ion distribution—the inner region called the Stern layer and outer layer the diffuse layer.

The EDLC behavior will be affected by the types of electrolyte ions, the solvent in which the electrolyte ions are dissolved, the electrical field across the electrode, and the chemical affinity between the adsorbed ions and the electrode surface. Because of the high porous structure of normally used electrode materials, the EDLC behavior at the pore surface is more complex than other effects such as the space constrain inside the pores, the tortuous mass transfer path, the wetting behavior of the pore surface by the electrolyte, and the ohmic resistance associated with the electrolyte. Thus the capacitance of a supercapacitor can be express as: $C = A \varepsilon_r \varepsilon_0/d$. A is the specific area, d is the distance between cathode and anode, ε_r is the electrolyte dielectric constant, ε_0 is the permittivity of a vacuum.

Pseudo-capacitance can be defined as the electrochemical storage of electricity in an electrochemical capacitor device. The main contribution to this type of capacitance comes from two parts: first, the fast sequence of reversible faradaic redox reaction; second, the electrosorption or intercalation of ions on the surface of suitable electrodes.

Accompanied by electron charge transportation process, pseudo-capacitance is determined by ion transportation between electrolyte and electrode which is limited by ion de-solvation and adsorption. The unit for pseudo-capacitance is Farad which means one electron per charge. In the adsorption process, there is no chemical reaction involved (no chemical bonds arise since only a charge-transfer take place). While the Faradaic pseudo-capacitance would normally be accompanied by static double-layer capacitance where both pseudo-capacitance and EDLC contribute to the total capacitance. The value of pseudo-capacitance depends on the electrode surface area, electrode active material and detailed structure of the electrodes. The value of pseudo-capacitance is much higher than that of EDLC with the same surface area (almost one hundred times bigger). The value can be linearly proportional to the working voltage. For pseudo-capacitance, the state of art material is ruthenium and ruthenium related oxide. The reaction equations can be described as:

$$RuO_x(OH)_y + \delta H^+ + \delta e^- \Leftrightarrow RuO_{x-\delta}(OH)_{y+\delta}$$

While pseudo-capacitance is more than EDLC capacitance, it suffers from a low power density and stability during cycling due to the poor electrical conductivity and reaction time needed to fulfil the entire charge collecting process.

1.4.2 Parameters of SCs Evaluation

Similar to lithium-ion battery, important parameters to evaluate the supercapacitor device are: energy density, power density, working potential, cycling performance, electrochemical impedance and rate performance. We summarized the calculation of capacitance, energy density and power density in different situations.

For single electrode material, electrochemical property is more suitable to define the related “performance”. The specific capacitance can be calculated based on the CV curves or charge-discharge curves. Single electrode is usually tested in a standard three-electrode system where the electrode is applied as working electrode, Pt plate as counter

electrode together with related reference electrode to conduct the test. If the charge-discharge curves are of triangular shape, the specific capacitance can be calculated as:

$$C_m = \frac{I \times \Delta t}{\Delta U \times m} = \frac{I}{m(\Delta U / \Delta t)} \quad (1)$$

where C_m (F g^{-1}) is the specific capacitance, $\Delta U/\Delta t$ is the linear slope of the discharge curve after initial IR voltage drop, and m is the active material mass of the working electrode. If pseudocapacitor electrode that the discharge curve is nonlinear, the capacity is voltage dependent, so the obtained capacitance by Eq. (1) is only an average value. There is a trend that people treat the nonlinear discharge curve with obvious plateau as battery behavior and calculate mAh/g accordingly. If the charge-discharge curves are not in triangular shape, capacitance can be calculated based on CV curves in the below equation:

$$C_m = \frac{Q}{\Delta U \times m} = \frac{\int IdU}{2mv\Delta U} \quad (2)$$

where C_m (F g^{-1}) is the specific capacitance, Q (C) is the average charge, ΔU (V) is the potential window, v is the scan rate, and m is the active material mass of the working electrode. There is a factor 2 because one CV cycle includes charge and discharge process, and the integral contains the charge of these two processes. The integral contains the charge of these two processes.

Regarding the two electrode systems or packaged full cell devices, the specific capacitance can be calculated according to their GCD plots as:

$$C_{s,cell} = \frac{Idt}{MdU} = \frac{I}{M(dU / dt)} \quad (3)$$

where I is the constant current in discharging, dU/dt is the slope of discharge curve after IR drop (in case of EDLC), and M is the total mass active materials in both electrodes. Significant errors can also be introduced by calculating the slope of (dU/dt) because sometimes it is subjective to choose the straight line. In case of oxide pseudo-capacitors or hybrid supercapacitors (battery-type electrode || EDLC-type electrode), the discharge curve is nonlinear and usually have plateau, and capacitance varies with voltage. The capacity is voltage dependent, so the obtained capacitance by taking ΔU/Δt is an average value. In this circumstances, the method recommended is to use two date points from the discharge curve with equation 4:

$$\frac{dU}{dt} = \frac{V_{\max} - \frac{1}{2}V_{\max}}{T_2 - T_1} \quad (4)$$

For full cells, because of series connection, the textbook reciprocal relation between overall capacitance of the device (Ccell) and that of each individual electrode (C+ and C–) is:

$$\frac{1}{C_{s,cell}} = \frac{1}{C_+} + \frac{1}{C_-} \quad (5)$$

For symmetric capacitors, C+ = C– (F), the measured capacitance (F) for one electrode is:

$$C_{cell}(F) = \frac{1}{2}\mathrm{C_s(F)} \quad (6)$$

The relationship for specific capacitance (F/g) is therefore:

$$C_{s,cell}(F) = \frac{C_{cell}}{M} = \frac{1}{4} C_s (\text{F/g}) \quad (7)$$

where C_{cell} (F) and $C_{s,\ cell}$ (F/g) is the measured capacitance and specific capacitance, respectively, for the full cell, and M is the total mass of active materials in both electrodes. The multiple of 4 adjusts the capacitance of the cell and the combined mass of two electrodes to the capacitance and mass of a single electrode. For example, a single carbon electrode (with a surface area of 1000 m^2/g) exhibits the capacitance of 10 μF/cm2. This gives rise to a specific capacitance of 100 F/g for one electrode. For a symmetric cell, two electrodes with half the total capacitance and doubled weight results in 25 F/g for the active capacitor. For asymmetric capacitors, Eqs (6) and (7) are not suitable. First, one must have mass balance based on charge equivalence on both electrodes:

$$\frac{m_+}{m_-} = \frac{C_- V_-}{C_+ V_+} \quad (8)$$

Where the capacitance of individual electrodes is estimated from three-electrode or two electrode testing mentioned above, before they are fabricated into full cell. The specific capacitance can be evaluated from the discharging curve according to Eq (9)

$$C_{s,cell}(F/g) = \frac{I}{dV/dt}\left(\frac{1}{m_+} + \frac{1}{m_-}\right) \quad (9)$$

The coulombic efficiency (η) of the supercapacitors can be characterized by charge/discharge process according to

$$\eta = 100 \times \frac{Q_{dis}}{Q_{ch}} \quad (10)$$

Where Q_{dis} and Q_{ch} refer to discharge capacity and charge capacity, respectively. The Δt_d and Δt_c refer to discharging and charging time, respectively. It is different from Li-ion batteries.

The standard method to obtaining the ED and PD is based on the discharge curves. The safest way is to integrate the area below the galvanostatic discharge curves:

$$E_{\max}(Wh/kg) = \frac{\int UdQ}{M} = \frac{\int UIdt}{M} = \frac{I\int Udt}{M} \quad (11)$$

$$P_{\max}(W/kg) = \frac{U^2}{4R_s M} \quad (12)$$

$$P_{Ave}(W/kg) = \frac{E_{\max}}{\Delta t} \quad (13)$$

$$R_s = \frac{U_{IR}}{2I} \quad (14)$$

where I is the discharge current (constant), U is the maximum cell operating voltage which is determined by the thermodynamic stability of an electrolyte, M is the total mass of active materials in a supercapacitor device, R_s is the equivalent series resistance (ESR) of the cell, U_{IR} is the initial iR drop. The factor 2 in Eq. (14) is due to current change from I to –I at highest voltage point. Sometimes people can estimate the effective capacitance of a device (C_{eff}, F) based on measured energy:

$$E\ (Wh) = \frac{1}{2} C_{eff} U^2 \quad (15)$$

Where the E represents maximum energy stored in a capacitor. In commercial evaluation, only 0.75 E_{max} can be effectively used (discharge $V_{max} \rightarrow 0.5\ V_{max}$). Therefore, in Eq. (15) one can add a factor of 0.75 in right side. C_{eff}/M gives the specific capacitance.

1.4.3 SCs electrode materials

Electrode material is of key importance for a supercapacitor device to reach high electrochemical performance. Towards high performance, the common characteristics of good electrode candidates are mainly: high surface area, high conductivity, high overpotential against oxygen/hydrogen evolution and high stability in electrolytes. The supercapacitor electrode materials can be classified in two types according to the functional mechanisms: first is the functioning as EDLCs and second is functioning rely on redox reactions or so called "Faradic materials".

Pure EDLCs typed materials are normally carbon-related materials. This typed electrode materials tend to show rectangle or quasi rectangle shaped CV curves even at a low scan speed. Research efforts have been input towards activated-carbon, carbon nanotubes and graphene-related materials. These typed electrodes functioning well in acid (H_2SO_4), alkali (KOH) and neutral (LiCl) electrolyte. They show great advantage on reaching high safe working voltage in aqueous electrolyte with high value reported over 2 V.

Pseudo-capacitance dominant electrode materials can be classified as: conducting polymers (PPy, PANI, PEDOT et. al.), metal oxides/hydroxides, metal sulfides/carbides/nitrides etc.

Metal oxides/hydroxides as supercapacitor exhibit the advantage of high capacitance. Though debate exist of the "battery behavior" in these type electrodes, they are promising to work as high energy density supercapacitor electrode active materials. Regarding the capacitance contribution differentiation, Dunn et. al. has promoted the calculation methods based on the CV curves as follows:

First, the current against scan speed be expressed in the equation:

$$i = av^b \quad (1)$$

where i is the measured current, v is the sweep rate, a and b are adjustable parameters.

When b equals 1, the current is fully contributed by capacitive behavior and when b equals 0.5, the current is fully ion-diffusion controlled contribution.

Then, the equation can be expressed in logarithm:

$$\log i = b \log v + \log a \quad (2)$$

In the charge storage process, we separate the charges coming from two resources, thus the charges q can be expressed as:

$$q = q_s + q_d \quad (3)$$

where q is the total charges, q_s stands for the capacitive contribution while q_d stands for the ion-diffusion controlled contribution.

Furthermore, the current with voltage can be expressed as follows in CV curves:

$$i(V) = k_1 v + k_2 v^{1/2} \quad (4)$$

Thus, divided by $v^{1/2}$, the equation can be written as:

$$i(V) / v^{1/2} = k_1 v^{1/2} + k_2 \quad (5)$$

With a series test of CV curves under different scan speed, the k_1 and k_2 can be precisely valued since the charge can be expressed as:

$$Q = \frac{\int I \bullet dE}{vS} \quad (6)$$

Therefore, the capacitance contribution from ion-diffusion is:

$$Q_d = \frac{\int k_2 v^{1/2} dE}{vS} = \frac{k_2}{Sv^{1/2}} \int dE \qquad (7)$$

And the capacitance contribution from capacitive behavior is:

$$Q_s = \frac{\int k_1 v dE}{vS} = \frac{k_1}{S} \int dE \quad (8)$$

Generally, the materials that with high capacitive behavior contribution can sustain fast scan and thus resulting in high rate performance and being preferred.

Metal sulfides/nitrides/carbides are emerging cathode material candidates for supercapacitor applications. They stand out because of the high stability and conductivity in aqueous electrolyte and thus are promising to improve the power density further emphasizing the fast energy delivering advantage.

1.5 Motivations and scope

In this thesis, the focusing point is to fabricate high performance nano-electrodes to satisfy different energy storage applications. Specifically, regarding the Lithium-ion battery research, we aim at increase the cyclability by stabilizing the structure of its electrode materials. For supercapacitors, the target is to increase the energy density by enlarging the device working voltage. we will focus on the electrode morphology and structure tuning according to the different requirement for different systems.

Regarding the battery applications, structure stability is the key point in this project. Thus, with maximum efforts to keep the high capacity (applying active materials with

high theoretical capacity such as SnO_2 and CuO) we added structural stabilizing material such as TiO_2 nanotube backbone and graphene quantum dots (GQDs) covering to do two dimensional and one dimensional enhancement separately. The successful realization of TiO_2 nanotube @ SnO_2 nanoflake demonstrates the idea of facet-preferable growth effect in synthesis core-branch electrode nanoarrays. Without the suppress of the volume expansion which is the main reason for high capacity, the entire electrode successfully inhibited the advantages of both TiO_2 (structural stability) and SnO_2 (high capacity). While the fully homogeneous coverage of GQDs to the CuO sustained one thousand cycles at high current density manifests the wisely structure design idea.

Although metal oxides have high theoretical capacity, they suffer from poor conductivity which remains to be weak spots. To figure out more synthesize methods for new generation electrode materials, we selected metal nitrides as new exploring objects. Due to the intrinsic properties of metal nitrides, we judge them to be more suitable as supercapacitor electrode materials. With introducing high capacitance electrode materials, we aim at achieving high energy density supercapacitors. In supercapacitor applications, there is no SEI layer issues. Thus we seek high surface area of the electrode materials. Efforts have been put in finding high surface area substrate as well as making nanostructured electrodes. With vertically aligned graphene nanosheets well obtained from our collaborators, ALD was applied to deposit the electrode materials to fully use the high surface area. Regarding making nanostructured-electrodes, method was tried to form core-shell structure.

Detailed design process will be discussed in following chapters.

Chapter 2 Metal Oxides for lithium-ion batteries

2.1 TiO_2 nanotube@SnO_2 nanoflake for LIB

2.1.1 Introduction

With the world-wide concern of energy crisis, green efficient energy storage devices research is attracting more attention recently.[36-39] Among all the explored clean power sources, lithium-ion batteries (LIBs) have become the most widely consumed secondary batteries because of the advantages of high voltage and energy density.[40-44] The pursuit of high-performance LIB never stops although it still cannot satisfies the human development requirements.

In the past decades, researchers have devoted great efforts to searching for suitable anode materials with high-performance properties. Among all the available oxide materials, SnO_2 stands out[36, 38, 41, 45-62] due to its high potential capacity (782 $mAhg^{-1}$), twice as much of the commercialized graphite (372 $mAhg^{-1}$) anode.[43] However, SnO_2 based anode normally suffers from a large volume expansion (300% volume expansion upon Li^+ alloying) which results in a severe capacity fade during cycling.[63] Worse still, the low conductivity of SnO_2 makes it to be easily aggravated and deteriorated especially when the current density is high. To alleviate these drawbacks, it is highly important to modify the SnO_2 anode by forming core-shell hybrid structures with other stable materials that have low volume expansion.[61, 64, 65]

Among all the materials that with low volume expansion, TiO_2 is popular because of its super low cost.[66-69] Though with a low theoretical capacity (178 $mAhg^{-1}$), it has been demonstrated with excellent structural and cycling stability. The semiconducting nature makes it a suitable backbone to sustain long battery cycling.

In previous research, the combination of TiO_2 and SnO_2 have been studied and

enhanced electrochemical performance have been reported. Radio frequency sputtering method have been used to fabricate the TiO_2/SnO_2 core-branch structure.[70] The composites show controllable thickness of each of the active material with homogeneous distribution. However, using silica as the substrate cannot be applied as a flexible electrode. Other method of electrochemical and solvothermal growth have been tried to prepare the SnO_2 @ TiO_2 nanotube structure.[71] Though a rather stable capacity was demonstrated, the energy density cannot be considered as high due to the structure design failure that the amount of SnO_2 encapsulated into the TiO_2 tubes is limited. Electrospinning process has applied to control the size of bicomponent TiO_2/SnO_2 nanofibers.[72] However, in this design, TiO_2 and SnO_2 are tightly connected in one side while they have quite different volume expansion during lithiation delithiation processes. This will be a serious structure unstable problem since they will apart each other during the lithium-ion battery cycling process. Other trials aiming at protecting SnO_2 by enwrapping SnO_2 inside TiO_2 thus to suppress the volume expansion of the SnO_2 have been reported [54, 56, 57]. However, in this design, the outer TiO_2 can block and retard the direct access of Li^+ into SnO_2 which should be the main capacity contributor. In order to secure enough contact for the SnO_2 with the electrolyte, the SnO_2 should be released in the outside of the core-shell structure. Thus, the SnO_2 can have a direct contact with the Li ions. Moreover, as a low capacity material, the amount of TiO_2 should be controlled to have a lower mass ratio compared with SnO_2.

Hence, in this chapter, a hierarchically porous TiO_2 nanotube @ SnO_2 nanoflake core-branch nanoarrays are reported as the LIB electrode active material. The whole structure is synthesized by combining atomic layer deposition (ALD) and hydrothermal growth process. The as obtained core-branch anode has a unique nanoflake structure and are tightly connected to the vertical-standing TiO_2 nanotube backbones, forming a nano-forest on the Ni foam substrate. The spaces between SnO_2 nanoflakes are acting as the buffer space to accommodate the volume expansion and assure the full access of the Li^+. In comparison with the commercial SnO_2 powder anode, the as synthesized core-branch electrodes exhibit much higher gravimetric capacity and enhanced rate

capability.

2.1.2 Experiments

Materials synthesis: The core-branch arrays were fabricated mainly by the combination of hydrothermal synthesis and ALD process. Before the growth, Ni foam substrates were cut into unified size (4×5 cm^2) and washed in acetone, ethanol and distilled water (DI water) for 10 mins, respectively and dried with Nitrogen gas. Then, the back sides of the substrates were covered uniformly with a polytetrafluoroethylene tape to keep the back side of the substrate clean in order to keep the high conductivity of the substrate and stay away from the unwanted particles in the solution. The growth of backbone material TiO_2 is a template-sacrificing process. First, self-supported $Co_2(OH)_2CO_3$ nanorod were grown to the Ni foam through a facile hydrothermal synthesis process which the solution was mixed by dissolving 10 mmol of $CO(NH_2)_2$, 2 mmol of $Co(NO_3)_2$ and 5 mmol NH_4F in 50 mL of DI water. The resulted solution was transferred into 40 ml Teflon-lined stainless steel autoclaves and maintained at 105 ºC for 5 h. After the synthesis, the samples were cooled down to room temperature with the furnace. The samples were then washed thoroughly with DI water and dried overnight in the box furnace at 90℃. Second, coating the samples with a homogeneous layer of 20 nm TiO_2 through ALD (Beneq TFS200) process at 120℃. After the TiO_2 shell was coated, the samples were then dipped into 1M HCl for 20 min to remove the inside $Co_2(OH)_2CO_3$ nanorod template. To increase the TiO_2 nanotubes crystallinity as well as tighter their connection to the substrate, a preheat treatment was conducted to the obtained TiO_2 nanotubes at 200℃ for 2 h. Third, grow SnO_2 nanoflakes with a second hydrothermal process. The annealed TiO_2 nanotubes were put in the 80 ml Teflon-lined autoclave which contains 50 ml 0.5 mM $SnCl_4 \cdot 5H_2O$ and 10 mM NaOH. The autoclave was sealed and the hydrothermal synthesis was conducted in an electric oven at 200 ºC for 3 h. After the growth, the samples were washed thoroughly with DI water and dried overnight at 90 ºC. Finally, the as synthesized samples were annealed

in the furnace under 200 ºC for 2h. Regarding the control sample, commercial SnO_2 powders purchased from Sigma Aldrich and used without further purification. The powder was mixed with PVDF and super P (conductive additives) with a mass ratio of 8:1:1 and grinded for 40 min. The mixed powder was then transferred into a 50 ml beaker dipped by 5 ml N-methyl pyrrolidinone (NMP) and sonicated for 30 min to form the uniform slurry. To make the electrode, the sluffy was pasted on the surface of a clean uni-sized Ni foam and dried overnight in the furnace at 80 ºC.

Materials Characterization: The morphology of the samples was imaged by scanning electron microscopy (SEM, JEOL 2100), and transmission electron microscopy (TEM, JEOL JEM-2010F) at 200 kV.

Battery assembling and electrochemical measurements: The core-branch and SnO_2 powder materials were cut into the same size (diameter: ~ 13 mm) and assembled to a coin cell with Li foil as anode (half-cell). The cyclic voltammetry measurements, and electrochemical impedance spectroscopy were tested on a CHI760e electrochemical workstation (Chenhua, Shanghai). The charge/discharge tests were performed on a LAND battery testing system.

2.1.3 Results and Discussion

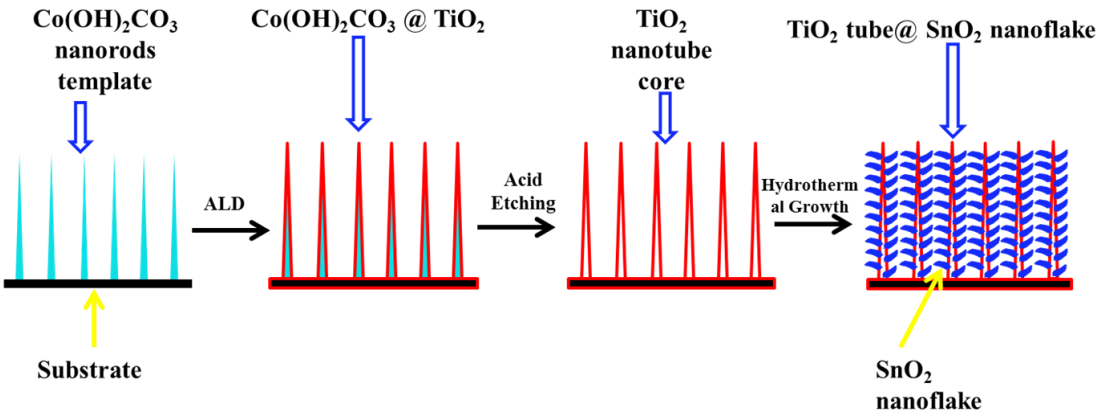

Figure 2.1.1 Schematics of the core-shell anode growth process: combination of ALD and hydrothermal synthesis.

The illustration above in Figure 2.1.1 demonstrated the core-branch nanowire

formation process through a template sacrificial method combined by atomic layer deposition and hydrothermal reaction. The backbone material TiO_2 nanotube is prepared by first ALD on $Co_2(OH)_2CO_3$ nanorods template which is synthesized in the hydrothermal reaction (details are described in experimental part). Then, the template was removed via immersing in a mild acid solution for 20 mins (the material turn totally white after the removal). As a following step, SnO_2 nanoflakes shell were fabricated in a second hydrothermal process after which the final TiO_2 nanotube/SnO_2 nanoflake core-branch anode is formed.

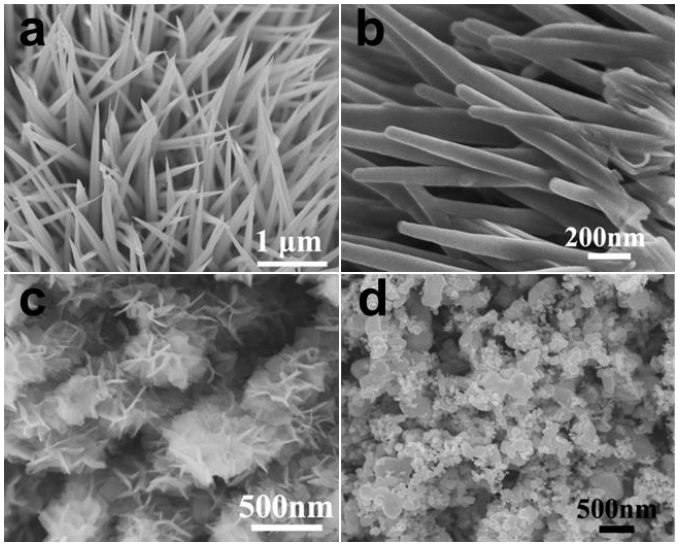

Figure 2.1.2 Morphology study of the samples at different stages. SEM Characterizations of core-branch nanowires and commercial SnO_2 powder: (a) $Co(OH)_2CO_3$ nanorods; (b) $Co(OH)_2CO_3$ nanorods covered with a 20 nm thick TiO_2 layer (inset is the TiO_2 nanotubes after the acid bath); (c) TiO_2 core @SnO_2 nanobranches; (d) Commercial SnO_2 powder used for comparison.

The morphologies of samples at different fabrication stages are shown in Figure 2.1.2. The hydrothermal-synthesized sacrificial $Co_2(OH)_2CO_3$ nanorods template is uniformly grown on the substrate with a length of ~1 μm and diameter of ~50 nm (Figure 2.1.2a). The surface of the template nanorod became smooth after ALD of a 20 nm TiO_2 layer and the diameter (~90 nm) of the rod enlarges (Figure 2.1.2b). After the removal of the template nanorods and the followed hydrothermal synthesis, the TiO_2 nanotubes are wrapped by SnO_2 nanoflakes homogeneously and formed the final

hetero-core-branch nanostructured nanoforest (Figure 2.1.2c). The commercial SnO_2 powder is composed of particles that is not homogeneous and with a wide size range up to 500 nm (figure 2d).

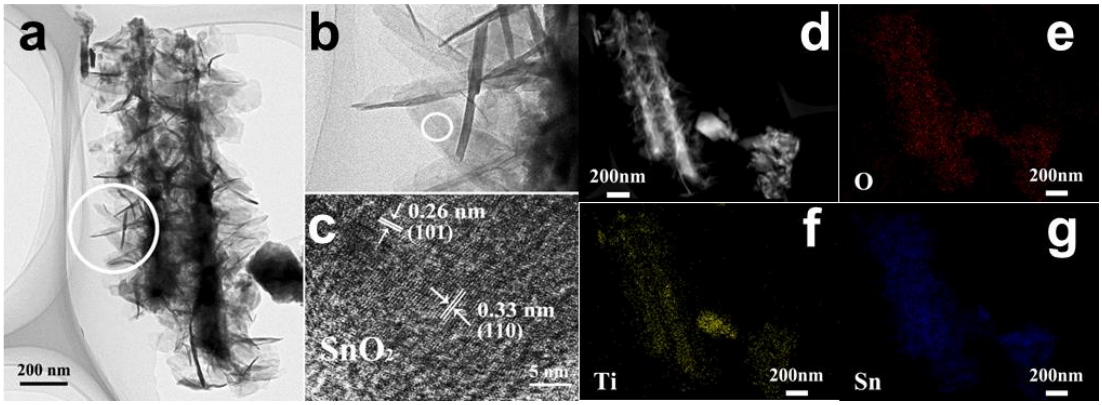

Figure 2.1.3 Crystal structure study by TEM. TEM Characterization of the TiO_2 nanotube @ SnO_2 nanoflake core-branch nanostructures: (a) TEM image of the integrated tube-flake core-branch structure. (b) Magnified image of the SnO_2 nanoflakes. (c) High resolution image of the SnO_2 nanoflake from the circled area in (b). (d - g) TEM elemental mapping images of the core-branch structure.

To unveil the detailed crystal structure, high-resolution transmission electron microscopy characterization (HRTEM) is introduced. As was shown in Figure 2.1.3a, the integrated core-branch structure is well realized and the nanoflakes can be clearly seen in Figure 2.13a and b. Moreover, TEM mapping is conducted. The element mapping of O, Ti and Sn correspond well to the profile of the core-branch hetero-structure (Figure 2.1.3d-g). In addition, the lattice fringes of 0.26 and 0.33 nm are observed which correspond to the (101) and (110) planes of the tetragonal SnO_2 in the HRTEM image (Figure 2.1.3c).

With the designed structure well realized, we proposed the advantages of this configuration as LIB anode are as follows: *Firstly,* the TiO_2 nanotubes which is ultra-stable can provide a stable backbone which can sustain long-term cycling and contributes to an improved cycling ability. *Secondly,* the ultrathin nanoflake shell can secure a higher surface area than the bulk powder particles. While the spaces between

the flake can accommodate the volume expansion of the shell during lithiation process. *Finally,* The SnO_2 nanoflakes have interface pairing with TiO_2 and are directly connected to the backbone. Besides, the entire core-branch structure is in a direct contact with the conductive substrates. This self-supported free-standing nano array anode reduces the dead mass by eliminating the usage of polymers binders and conductive additives.[65] Thus, we expect the entire design to be successful and should result in an improved lithium storage property.

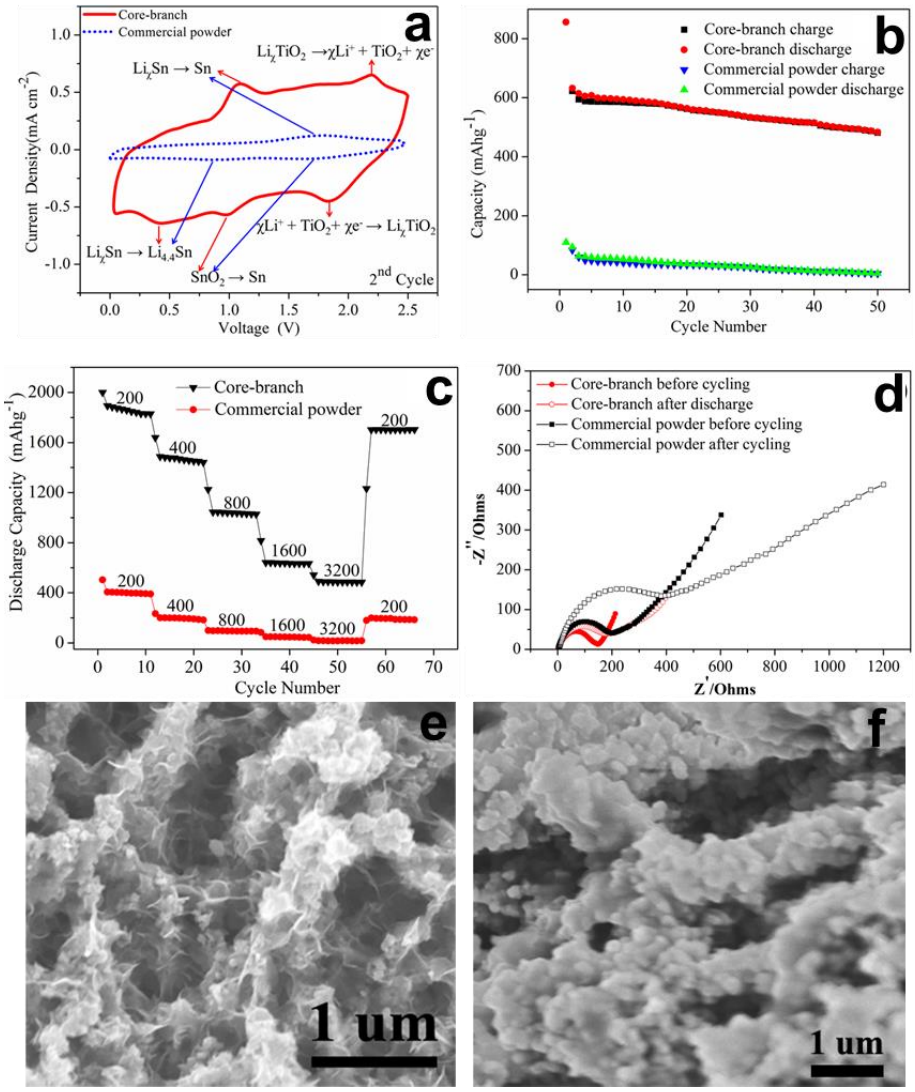

Figure 2.1.4 Electrochemical properties study. Comparison of the electrochemical properties between the TiO_2@SnO_2 core-branch nanostructure and commercial SnO_2 powder acting as the

anode for LIBs: (a) Cyclic voltammetry at a scan rate of 0.5 mV s^{-1} between 1 mV–2.5 V; (b) Cycling performance of the charge/discharge processes at a current density of 1.6 A g^{-1} with a voltage window of 0.01–2.5 V; (c) Rate performance against the cycle number at various current densities (unit: mA g^{-1}); (d) Nyquist plots of the TiO_2@SnO_2 core-branch and commercial SnO2 powder electrodes before and after 50 cycles. Test conditions: voltage range = 0.005–2.5 V versus Li/Li^+. Morphologies of the electrode material after 50 cycles. SEM images of structures comparisons of core-branch nanowires and commercial powder before and after cycles. TiO_2@SnO_2 core-branch electrode (a) before cycling and (b) after 50 cycles. Commercial SnO_2 powder electrode (c) before cycling and (d) after 50 cycles.

To verify the structural design methodology and the former proposal, electrochemical properties comparison of the obtained TiO_2 nanotube @ SnO_2 nanoflake core-branch nanowire arrays and the commercial powder are evaluated and plotted together. As was reported, the electrochemical reaction of SnO_2 with Li^+ as a LIB anode can be expressed in the following equations[43]

$$SnO_2 + 4Li^+ + 4e^- \rightarrow Sn + 2Li_2O \quad (1)$$

$$Sn + \chi Li^+ + \chi e^- \leftrightarrow Li_\chi Sn \quad (0 \leq \chi \leq 4.4). \quad (2)$$

Regarding the backbone TiO_2 nanotube, the reaction process is usually described as follow[73]:

$$\chi Li^+ + TiO_2 + \chi e^- \leftrightarrow Li_\chi TiO_2 \quad (0 \leq \chi \leq 1) \quad (3)$$

In Figure 2.1.4a, the cyclic voltammetry (CV) curves of the core-branch nanoarrays and commercial SnO_2 powder anode were compared (2^{nd} cycle with a scan speed of 0.5 mV s^{-1}). A cathodic peak ~ 1.6 V was detected for the commercial SnO_2 powder in the discharge process which should be ascribed to the reaction of SnO_2 transferring to metallic Sn as was described in equation (1).[71] While the peak ~0.8 V should be caused by the phase transformation of $Li_\chi Sn$ to $Li_{4.4}Sn$ in equation (2). The corresponding reverse reaction, which is the desertion of Sn from the $Li_\chi Sn$, is located ~1.7 V. Regarding the as-obtained core-branch anode, the irreversible phase change from SnO_2 to Sn is happened ~ 1.0 and the lithiation and delithiation pairing peaks of

Sn are located at 0.4, and 1.2 V, respectively which is similar to previous work.[71] We noticed that there are large peaks shifts in the commercial powder SnO_2. This should be resulted from the size and structure effects. Regarding the bone material, the redox peaks of 1.8 and 2.3 V are observed as was described in equation (3).

It is noticed that the weight ratio of the backbone TiO_2 in the entire nanocomposites is ~ 20%. Therefore, the tubular backbone can serve as a structural scaffold as well as contribute some capacity. The main capacity contributor is the nanoflake SnO_2 shell due to its high theoretic specific capacity. In the long battery cycles (Figure 2.1.4b), the charge-discharge cycling is tested at a current density of 1.6 A g^{-1}. The core-branch anode delivers much higher charge/discharge capacities than the commercial powder anode. Furthermore, the high capacity around 580 $mAhg^{-1}$ is maintained within 50 cycles for the as synthesized core-branch nanoarray anode at the current density of 1.6 A g^{-1}. While the capacity of the commercial SnO_2 powder electrode is almost zero. This further demonstrates the advantages of the core-branch architecture. The flake structure of SnO_2 secures higher reaction areas for the lithiation and delithiation reactions and the SnO_2 nanoflakes accessed by Li^+ freely contributing to the charges accumulation. The as observed low initial coulombic efficiency (~ 69.5%) is due to the formation of irreversible solide-electrolyte-interface (SEI) film at the first cycle. After the first cycle, the coulombic efficiency increases to nearly 100% and retained in the rest of the cycles as manifested by the nearly overlapped cycling curves of the charge and discharge processes. The higher capacity is also observed in the rate performance test. Though capacity drop is obvious when increasing the current density for both the commercial powder and the as obtained core-branch array anode, with no circumstances that the latter exhibit almost twice more of the capacity values (Figure 2.1.4c). When charge-discharge at a high current density of 3.2 A g^{-1}, the core-branch anode exhibits a capacity of 498 mAh g^{-1} and nearly 90 % of the capacity is retained after switching back to same current density of 0.2 Ag^{-1}. While for the commercial powder, the capacity fading is all the way down to nearly zero. Worse still, the capacity retention is less than 20% when the scan current density is recovered to 0.2 A g^{-1} again.

Galvanostaic charge-discharge curves of 1st, 2nd, and 50th cycles of the as synthesis core-branch electrode are plotted together. In the 1st discharge and charge curves, the plateaus correspond well with the CV in Figure 2.1.4a. From the 2nd and 50th cycles, we see the slightly capacity drop in accordance with the cycling curves in figure 2.1.4b.

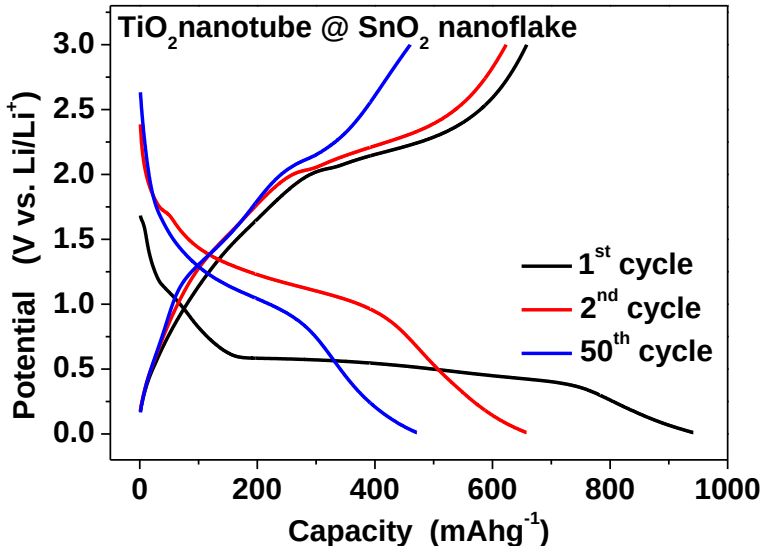

Figure 2.1.4 Galvanostatic charge discharge curves of the TiO_2 nanotube @ SnO_2 nanoflake core-shell electrode.

To figure out the electrochemical reasons, Nyquist plots of the two types of anodes are plotted together before and after cycling (Figure 2.1.4d). It is obvious that after cycling, the electrochemical impedance increases for both electrodes. However, the core-branch anode delivers lower impedance both before and after cycling demonstrating the fast ion/electron transportation which is the main reason for the much higher capacity. After cycling, both electrodes materials were taken out in a glovebox and washed with acetone and ethanol thoroughly before taking SEM images. After checking the SEM images of the two electrodes (Figure 2.1.4e and f), compared with their original morphology as shown in Figure 2.1.2c and d, it can be concluded that the structure of the as obtained core-branch anode is almost kept while severe aggregation problems are noticed for the commercial powder material which further manifests the successful structure design. Thus the core-branch architecture is table in long cycles.

To find the research position of our design, we list the performance comparisons

of our material with the recent research regarding the composites of SnO_2 and TiO_2 n table 2.1.1. At similar charge-discharge current density, our material delivers the highest capacity which should owe to the following advantages of our material design: first, the high mass ratio of SnO_2 in our design comparing to those work with solid TiO_2 or thick TiO_2 tubes makes the mass ratio of TiO_2 to high in the entire structure; second, in our design, the SnO_2 flake nanostructure is directly contacted with electrolyte ions and the volume expansion which is the main source of the high capacity is not suppressed.

Table 2.1.1. Performance comparison of TiO_2-SnO_2 composites as the LIB anode.

Material	Current density	Capacity after 30 cycles	Ref.
SnO_2 nanocrystals on self-organized TiO_2 nanotubes (array)	20 mA cm^{-2}	35 μAh cm^{-2}	[74]
SnO_2@TiO_2 double shelled nano-spheres (powder)	1720 mA g^{-1}	128 mAh g^{-1}	[75]
TiO_2 nanocones@SnO_2 nanoparticles (powder)	1720 mA g^{-1}	350 mAh g^{-1}	[58]
SnO_2/TiO_2 nanocomposite (powder)	156 mA g^{-1}	581 mAh g^{-1}	[59]
SnO_2@TiO_2 nanotube hybrids (array)	0.1 mA cm^{-2}	160 μAh cm^{-2}	[71]
ALD amorphous thin layer SnO_2 anode directly on stainless steel substrate	5 μA cm^{-2}	641 mAh g^{-1}	[46]
SnO_2@TiO_2 hollow microtubes (array)	200 mA g^{-1}	805 mAh g^{-1}	[54]
SnO_2@TiO_2 double-shell nanotubes (array)	1500 mA g^{-1}	232 mAh g^{-1}	[56]
SnO_2@TiO_2 core-shell composites (powder)	1000 mA g^{-1}	659 mAh g^{-1}	[57]
SnO_2 nanoflakes on TiO_2 nanotubes (array)	**1600 mA g^{-1}**	**530 mAh g^{-1}**	**this work**

2.1.4 Conclusion

In this chapter, we presented the fabrication of core-shell nanoarrays through the

combination methods of atomic layer deposition (ALD) and hydrothermal synthesis. We successfully synthesized the TiO_2 nanotube@SnO_2 nanoflake core-branch anode and proved the Li ion storage performance enhancement compared to the commercial SnO_2 powder. The as obtained electrode exhibits drastically higher specific capacity and better cycling stability than the commercial powder. The unique core-branch architecture and the ultra-thin property of the flake SnO_2 shell, which can provide direct ion/electron transfer and good structural stability should be the two main reasons for the enhanced electrochemical property. The successful fabrication and electrochemical performance enhancement demonstrates the usefulness of ALD TiO_2 as backbones for constructing high-performance metal oxide core-shell electrodes for batteries (lithium/sodium-ion battery) and supercapacitors.

2.2 CuO nanowire @ Graphene Quantum Dots for LIB

2.2.1 Introduction

In lithium-ion battery (LIB) research, searching for better electrode materials that with higher capacitance, conductivity and stability are always the key rules.[44, 76-82] Among all the metal oxide, copper oxide (CuO) stands out as a promising LIB anode candidate because of its advantages of high theoretical capacity (674 mAh g^{-1}), low cost and environmental benignity. Nevertheless, the practical applications of CuO as LIBs anode are stacked by the low conductivity (p-type semiconductor) and large volume expansion (174 %).[83] These problems will cause particle pulverization of the anode which is the most critical disadvantage of this material. To deal with this issue, major efforts have been put on making heterogeneous-structures and doing the surface coatings to the CuO anode. Efforts have been put on fabricating kinds of CuO nanostructures.[84-89] Though better electrochemical performance was achieved compared with the bulk powder materials, the reported low cycle numbers which is less than 100 are insufficient to demonstrate its long-term cyclability. Regarding the surface coating, researchers studied the heterogeneous-nanostructures of CuO/Cu_2O,[90, 91] and Fe_3O_4/CuO hybrid wires.[92] These core-shell composites though with higher capacity are still suffered from large volume expansion and low electric conductivity and thus their cycling stability is usually low. Thus, to have a long-term lifespan, it is important to introduce highly conductive protective layer to the CuO anode. Researchers have attempted to make stable additive surface layer by coating with carbon/polymer materials, such as glucose,[93, 94] PEDOTs,[95, 96] graphene,[97] and carbon nanotube.[98, 99]

To alleviate the low initial coulombic efficiency (~35 %,[85, 100] ~65 %[86, 87, 89, 101-105]) problem of CuO as LIB anode, efforts have been tried to coat a Cu conductive layer to the Cu_2O nanoparticles surface. With this trial, they achieved a higher (77%) coulombic efficiency.[106] Thus we try to graft this approach to our CuO anode. However, the effectiveness of the Cu layer alone will weaken upon cycles since the

metallic Cu layer will be corroded in organic electrolyte. Thus to further enhance the structural stability and sustainability, carbon materials coating is needed. Recently, graphene quantum dots (GQDs) have shown high solubility in various solvents,[107, 108] and the capability of conformal wrapping to well-textured nanostructures by simple electrophoresis method.[109] As a highly conductive material, the GQDs coating is expected to decrease the electrode electrochemical impedance which will facilitate the ion/electron transportation. Previous literatures have reported the chemically modified GQDs applied in many energy storage systems such as supercapacitors,[109] solar cells,[110-112] oxygen reduction reaction electrodes,[113] bio-analysis and sensors.[114] Therefore, we want to try the GQDs in LIBs electrodes to see its possible effects.

Herein, in this chapter, we are going to discuss the design and synthesize of CuO+Cu+GQDs (referred as CCG) triaxial nanowire arrays as LIB anode. Comparing with un-protected CuO+Cu (referred as CC) core/shell nanowire electrodes, we see the surface conductivity and the stability of the unique GQDs soft protection to the entire nanowire array structure. The as obtained CCG anode delivers a higher rate capability and better long term cyclability that is up to 1000 times. These results indicate the great effect of GQDs in enhancing the battery electrodes materials (such as Sn or SnO_2, Si) with high volume expansion.

2.2.2 Experiments

Graphene quantum dots (GQDs) Synthesis: Graphene powder was used directly as purchased to synthesize the GQDs via a modified Staudenmaier process where 4 g of the graphene powder was added to acid solution mixed of H_2SO_4 (150 mL) and HNO_3 (80 mL). The mixture was stirred at 15 °C for 2 h after which 40 g of $NaClO_3$ was added gradually while the temperature was lowed to below 5 °C. And then, the mixture was stirred for another 5 h at 15 °C. Distilled water (80 mL) was added to terminate the reaction and the PH value was adjusted to 7 with NaOH. Finally, the

mixture was filtered with an alumina inorganic membrane of which the pore size is 20 nm. To purify the GQDs and remove excess salt, the obtained light yellow solution was dialyzed in a 3500 Da dialysis bag in deionized water for a week. The obtained lighter yellow solutions were transferred to autoclaves and heated at 200 °C for 5 h to reduce the oxygen-containing groups.

Synthesis of CuO-based electrode materials: All reagents were directly used as they were purchase from Sigma-Aldrich without further purification. In this work the Cu foams as substrates were first compressed and then cut into unified-sized pieces (1×1 cm^2). A small rectangle holder (0.4×1 cm^2) was left at the middle of one side of each substrate to be the connection part. Before the electrochemical fabrication, all the substrates were washed step by step in acetone, ethanol and distilled water and then dried with N_2 gas (in case of oxidization, the substrate should not be dried with any heat). We covered the back side of the substrate with tape, and then synthesized the copper hydroxide in an anodization process in 1M NaOH solution conducted on a CHI 760d using chronopotentiometry technique. The final deposition current is 10 mA. After 10 min anodization, the substrates surface turned into pure blue which is proven to be $Cu(OH)_2$ nanowires. The samples of CuO were obtained by annealing the $Cu(OH)_2$ nanowires in air under 200 ^oC for 2 h. The samples of CuO+GQDs were obtained by anchoring the well dispersed GQDs to the CuO nanowire surfaces through an electrophoresis process (voltage: 6 V; time: 10 min) in a standard two-electrode deposition system with CuO as working electrode and platinum as counter electrode. The samples of final CuO+Cu+GQDs triaxial structure (CCG) was formed by annealing the former samples in Ar+5% H_2 (1.3 slm (standard liters per minute)) under 200 ^oC for 30 min. The control sample of CuO+Cu coaxial nanowires (CC) was fabricated through annealing the CuO nanowires under the same condition without the pre-step of electrophoresis of the GQDs.

Morphology and crystal structure characterization: All the morphology tests were conducted with scanning electron microscopy (SEM JEOL 2100), and transmission electron microscopy (TEM, JEOL JEM-2010F) operated at 200 kV. The crystal

structures of the samples were characterized with X-ray diffraction (XRD, RigakuD/Max-2550 with Cu Kα radiation), XPS measurements (VG ESCALAB 220i-XL system utilizing a monochromatic Al Ka1 source, 1486.6 eV) and Raman spectra (WITec-CRM200 Raman system with a laser wavelength of 532 nm, 2.33 eV). To calibrate the wavenumber, Si peak at 520 cm^{-1} was used as the reference.

Battery assembling and electrochemical test: The electrochemical tests were performed in standard CR2032-type coin cells which were assembled with the CuO-based electrode materials (CC and CCG) in an argon-filled glove box (Mbraun, Unilab, Germany). The electrolyte solution is 1 M $LiPF_6$ dissolved in ethylene carbonate (EC)–dimethyl carbonate (DME) (1:1) solution. The separator is a polypropylene (PP) film (Cellgard 2400). Regarding the electrochemical tests, charge discharge cycles were tested in Neware battery testing system with different current densities at a voltage range of 0.01 and 3.0 V vs Li/Li^+. While the CV measurements were conducted in a CHI-760d electrochemical work station with a scan speed of 0.1 mV s^{-1} with the same voltage range. Electrochemical impedance spectroscopy (EIS) was tested with the amplitude of the sine perturbation signal was 5 mV, between the lowest (5 mHz) frequency and the highest frequency (10 kHz).

Determination of the active materials mass loading: the samples were weighed after each step treatment with an analytical balance (d = 1 μg). We listed the mass values in the following table 2.2.1.

Table 2.2.1 Mass of samples at different synthesize procedures

Steps	Dealing steps	Products after the step	Mass (mg)
0	Substrate after clean for CC	pure Cu foam	S_0=101.724
0’	Substrate after clean for CCG	pure Cu foam	$S_{0'}$=101.719
1	Cu foam after anodization (CC)	$Cu(OH)_2$ on Cu foam	S_1=102.534
1’	Cu foam after anodization	$Cu(OH)_2$ on Cu foam	$S_{1'}$=102.529

	(CCG)		
2	Annealing in air (CC)	CuO on Cu foam	S_2=102.109
2’	Annealing in air (CCG)	CuO on Cu foam	$S_{2'}$=102.102
3’	Electrophoresis of GQDs	CuO+GQDs on Cu foam	$S_{3'}$=102.157
4	CuO annealing in Ar+H_2	CC on Cu foam	S_4=102.071
4’	CuO+GQDs annealing in Ar+H_2	CCG on Cu foam	$S_{4'}$=102.118

The calculations are based on the mass measurement above as below steps:

(1) From step 0 to 2 (step 0’ to 2’), the mass increase is due to the introducing of O, and the mass of O gained for CC sample can be calculated as $m_O = S_2 - S_0 = 0.385$ mg and meanwhile for CCG sample: $m_{O'} = S_{2'} - S_{0'} = 0.383$ mg. The reaction is

$$Cu \rightarrow CuO$$

Thus the mass of CuO in sample CC is $m_{CuO} = m_O \times M_{CuO}/M_O = 0.385\ \text{mg} \times 80/16 = 1.925$ mg; While the mass of CuO in sample CCG is $m_{CuO'} = m_{O'} \times M_{CuO}/M_O = 0.383\ \text{mg} \times 80/16 = 1.915$ mg.

(2) From step 2 to 4, the mass decrease is due to the loss of O, the O loss for CC anode is $\triangle m = S_2 - S_4 = 0.038$ mg, therefore the mass of CuO in sample CC is $m_{CC} = m_{CuO} - \triangle m = 1.925 - 0.038 = 1.887$ mg.

(3) From step 2’ to step 3’, the mass increase is caused by GQDs adding to the CuO, so the mass of GQD is $m_{GQD} = S_{3'} - S_{2'} = 0.055$ mg. From step 3’ to step 4’, the mass decrease is due to the O loss $\triangle m' = S_{3'} - S_{4'} = 0.039$ mg. Thus the mass of CuO+GQDs in CCG sample is $m_{CCG} = m_{CuO'} - \triangle m' + m_{GQD} = 1.931$ mg.

2.2.3 Results and Discussion

The entire growth design of the CCG triaxial is shown in Figure 2.2.1 the route 2 (as referred R2). In detail: first step is the anodization growth of $Cu(OH)_2$ nanowires (nucleation on the Cu foam surface first, Figure 2.2.1 f) and transferring to the oxide active material CuO through annealing the precursor at 200 ^oC in air for 2 h; second step is an electrophoresis process which aims at covering the CuO surface with a homogeneous layer of GQDs; final step is to anneal the CuO+GQDs and CuO (as

control sample) in Ar+H_2. Figure 2.2.1 f-i described the detailed illustration of the change from $Cu(OH)_2$ precursor to CCG triaxial nanowire where three layer of CuO, Cu and GQDs can be easily seen for the final heterogeneous nano-structure.

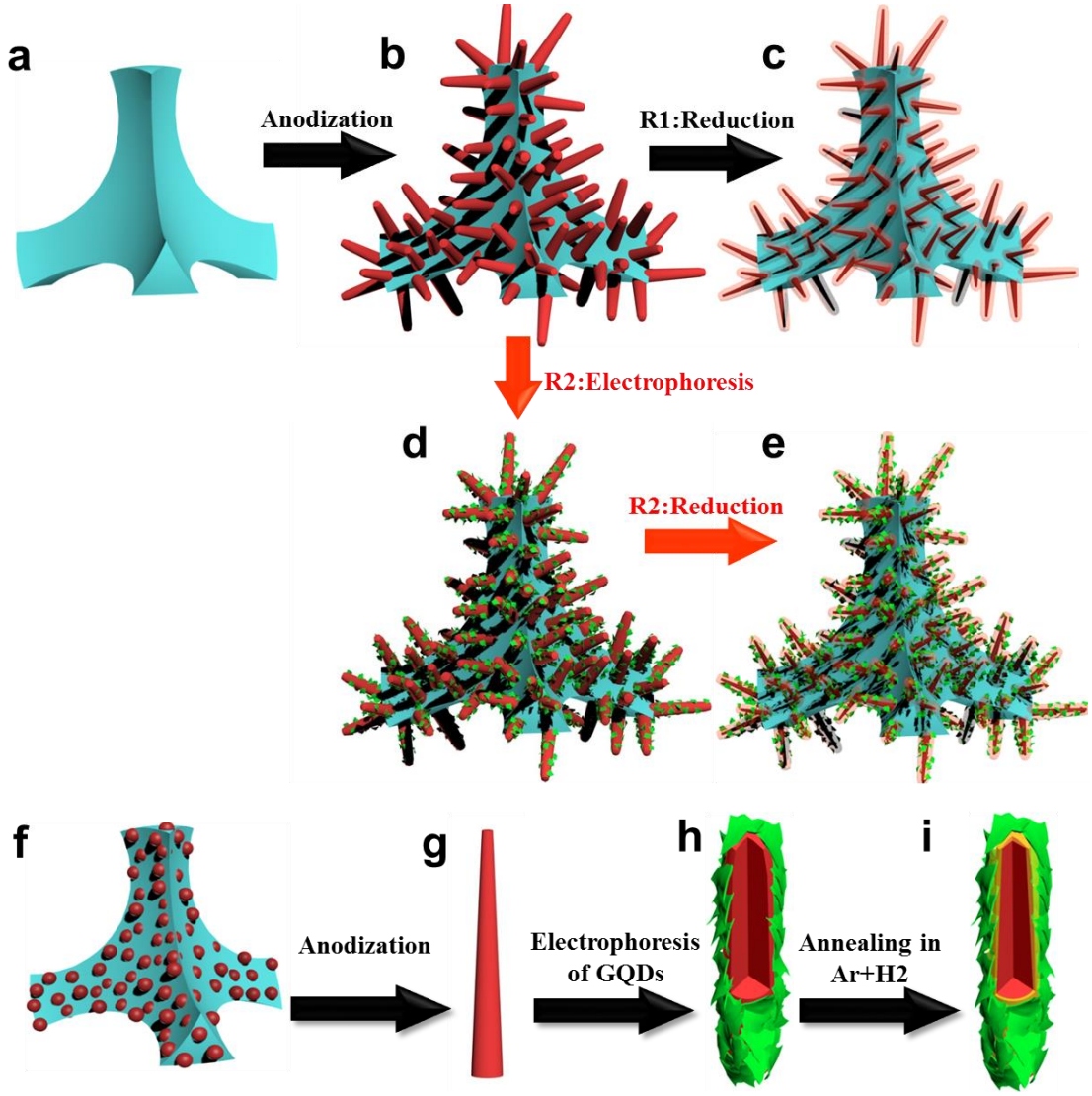

Figure 2.2.1 Illustration of the detailed synthesize processes of electrode materials. Route 1 and 2 are the demonstration of the fabrication process of controlled sample CuO+Cu (CC) core/shell nanowires and CuO+Cu+GQD (CCG) triaxial nanowires, respectively. a) Pristine copper foam, b) CuO nanowire obtained by a first anodization reaction and followed by a second step of annealing in air under 200 °C, c) CC core/shell nanowires synthesized by annealing CuO nanowires in an Ar + H_2 atmosphere under 200 °C, d) CuO nanowires with a layer of GQDs deposited by a further step of electrophoresis deposition of GQDs on b. (e) CCG triaxial nanowires achieved by reduction annealing of sample d in an Ar + H_2 atmosphere under 200 °C. f-i) **Detailed illustration of the**

CCG triaxial nanowires growth process.

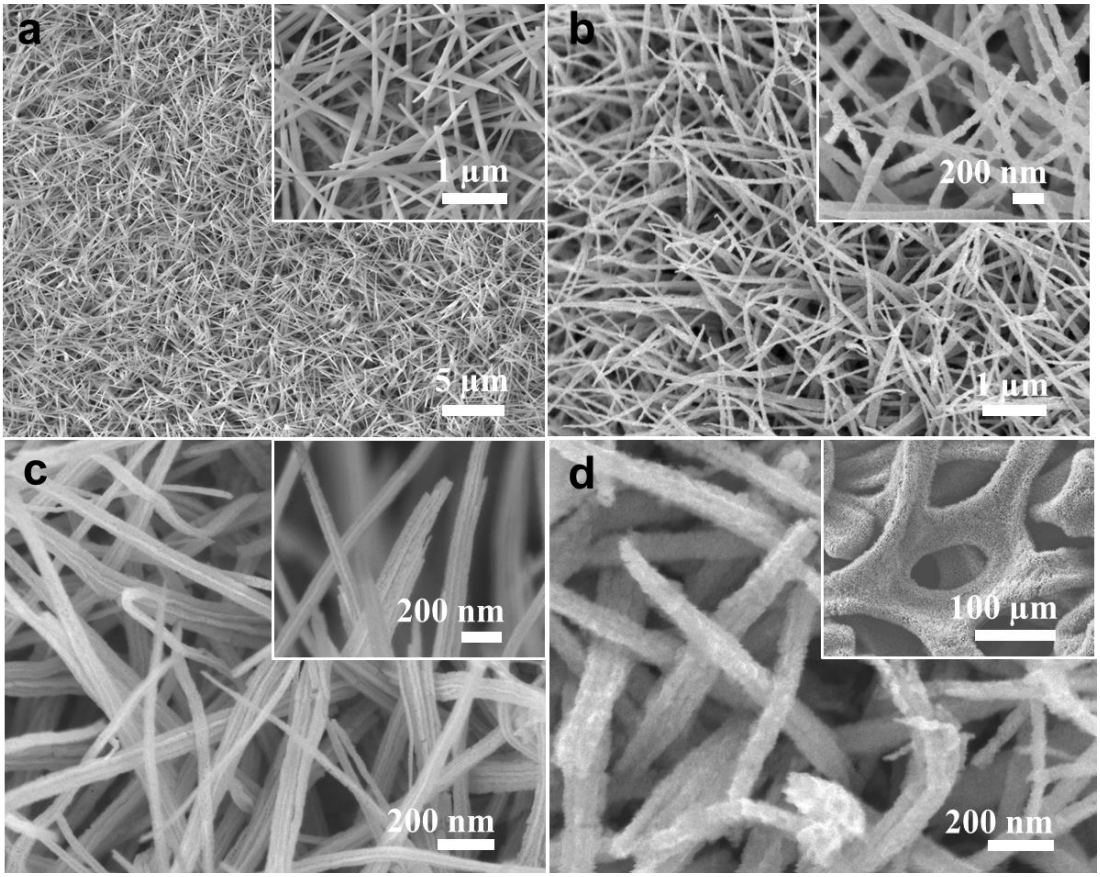

Figure 2.2.2 SEM images of the samples a) the $Cu(OH)_2$ nanowires source material, b) CuO nanowires after annealing sample a in air at 200 ^oC, c) CuO+Cu core/shell nanowires and d) CuO+Cu+GQD triaxial nanowires. Insets in figure a, b and c are the related high magnification views while the insets in figure d is the corresponding low magnification view.

Scanning electron microscopy (SEM) were utilized to image the corresponding images of the samples at different fabrication stages (Figure 2.2.2). Through tuning the concentration of the anodization solution, the density of nanowires can be adjusted. And the length of the anodized precursor $Cu(OH)_2$ nanowires can be adjusted by controlling the deposition time and current that applied. Since we don't focus on this part, the final deposition recipe was determined as was described in the experimental parts. Here the $Cu(OH)_2$ source material nanowire is with a diameter ~ 100 nm and a length ~ 1.5 μm (Figure 2.2.2a). After annealing the $Cu(OH)_2$ nanowires in air, the material surface turns rough (Figure 2.2.2b inset) which indicate higher surface area. Meanwhile, the

nanowire array structure is well maintained (Figure 2.2.2b). As the control sample, the CuO+Cu coaxial nanowires (Figure 2.2.2c) is obtained by annealing the CuO nanowire directly in Ar+H_2 for 0.5h and the inset figure shows its core-shell structure with a smooth surface. Regarding the CCG sample, it is clearly to see that the surface of CCG triaxial nanowires is mossy (Figure 2.2.2d) after the electrophoresis of an outer layer of GQDs. After the Ar+H_2 annealing, the surface of CCG sample keeps the fluffy property (Figure 2.2.2d inset) and this rough surface indicates larger surface area. Moreover, it indicates that there are more connection points for the electrochemical reactions which implies that the CCG layer coating may result in extra more capacity than the smooth surface of CC nanowire anode as discussion above.

To have more detailed information of the morphology and crystal structure of the CuO based anode materials, transmission electron microscopy (TEM) characterizations were conducted. Figure 2.2.3a shows the low-magnification TEM image of the GQDs with the inset the corresponding size distribution. As can be seen in the figure, the GQDs are well dispersed in NMP solution with the majority dot-size around 2-3 nm. Furthermore, when it goes to high resolution TEM (Figure 2.2.3b), the typical lattice parameter of 2.1Å correspond well to the (1100) lattice plane of GQDs which is also detected in latter characterization of CCG samples in Figure 2.2.3d. Figure 2.2.3c shows the HRTEM image of coaxial CC nanowires with the lattices of CuO (111) and Cu (011) detected and the inset figure shows the smooth layer of Cu ~ 15 nm. Regarding the final CCG triaxial nanowire (Figure 2.2.3d), the mossy morphology is confirmed with the SEM images in Figure 2.2.2d. Clear lattice planes of CuO (111) and Cu (011) are observed and at the edge of the sample, the carbon (1100) lattice is detected manifesting the successful coating of GQDs. To figure out the exact element distribution, TEM mapping (Figure 2.2.3e) shows the distribution of Cu, O and C, respectively. As can be seen clearly from the distribution figure, the profile of Cu is nearly identical to that of C while the profile of O is narrower than those of Cu and C. This indicates the formation of CuO+Cu+GQD triaxial sandwich structure uniformly.

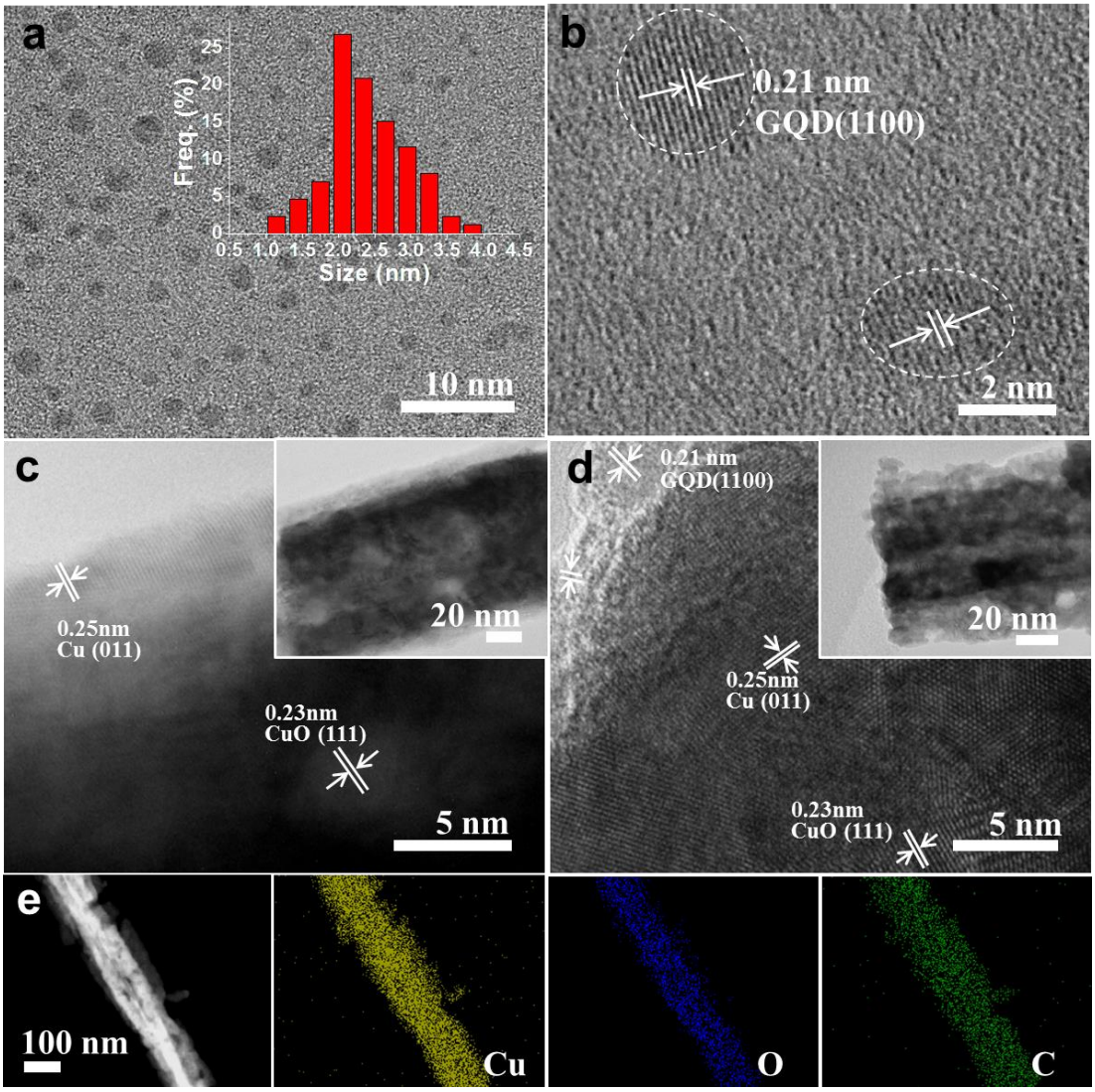

Figure 2.2.3 Detailed morphology and structure characterizations of the GQDs and CuO-based nanowires by TEM. a) TEM image of original GQDs. Inset is the corresponding size distribution. b) HRTEM of two GQDs shown the (1100) interface. HRTEM image of c) HRTEM image of CC core/shell nanowire and d) CCG triaxial nanowire. Insets are the related low-magnification view. e) TEM elemental mapping of the CCG triaxial nanowire.

To gain more evidence about the crystal phase and final compositions of the CuO based anode materials, more characterizations are conducted with the X-ray diffraction (XRD) (Figure 2.2.4a to c), Raman (Figure 2.2.4d), and X-ray photoelectron spectroscopy (XPS) techniques (Figure 2.2.4e and f). Grew on Cu foam, the XRD spectra of $Cu(OH)_2$ sample was detected the typical peaks from both metallic Cu and

$Cu(OH)_2$. After annealing, the commercial CuO powder exhibits the peaks from metallic Cu compared with the original conditions of CuO peaks only. Figure 2.2.4c shows that after annealing in $Ar+H_2$, both CC and CCG were observed with CuO and Cu peaks while CCG sample also shows the slight peak of C which should be caused by the surface GQDs. More evidence from Raman are presented in Figure 2.2.4d where the spectra show clearly peaks from GQDs[115, 116] of G band (1592 cm^{-1}) and D band (1347 cm^{-1}). Meanwhile, both CC and CCG samples revealed three main phonon modes of CuO nanowire, located at 291, 340 and 623 cm^{-1} and corresponded to the A_g, B_g^1 and B_g^2 symmetries[117-122], respectively. In addition, from the wide scan XPS spectra of CC and CCG nanowires (Figure 2.2.4e), it can be concluded that the intensity of C 1s peak of CCG sample is much higher than that from sample of CC, indicating the existence of graphene-related material. The weak C 1s signal in CC sample might come from the air and the carbon tape that used during the testing. The O 1s peak in Figure 2.2.4e is weak after annealing in $Ar+H_2$ which implies the low defect of GQDs and this should be the reason of the high conductivity of the CCG anode. In Figure 2.2.4f inset, the peaks of C 1s (C–C: 285.4 eV, C–O: 286.8 eV, O=C–OH: 289.3 eV) are corresponding well to those of graphene-related materials[123, 124], further verified the final electrode structure. Therefore, the conclusion can be draw that we have successfully fulfilled the fabrication of the integrated electrode in a uniform triaxial nanowires structure and fully covered the copper foam surfaces.

With the structure well realized, we propose the possible advantages of our CuO-based trilayer nanoarray structure as follows: first, a Cu surface layer should have a passivation effect of the sample surface.[106] Besides, in our experiment, the thin Cu layer was generated directly from the CuO nanowire and thus should have chemical bonding with the CuO core. This in return will ensure a good conductivity between active material and the electrolyte and thus high rate capacity can be expected. Furthermore, after the first charge process, this Cu layer can be anodized to CuO again thus lead to a compensation for the initial coulombic efficiency. Second, the GQDs may have served as a mechanically buffer and electrically conductivity “armor” that can

reduce the electrode polarization, increase the charge collection efficiency, and preserve the structural integrity of the CuO nanowire. Moreover, the GQD layer will contribute to initial coulombic efficiency through preventing the formation of solid electrolyte interfaces (SEI) layer on the electrode. Hence, we can expect the whole trilayer nanowire electrode to have high initial coulombic efficiency and capacity, rate capability and long-term cyclability. In the following part, the electrochemical performance will be presented to verify the hypothesis here.

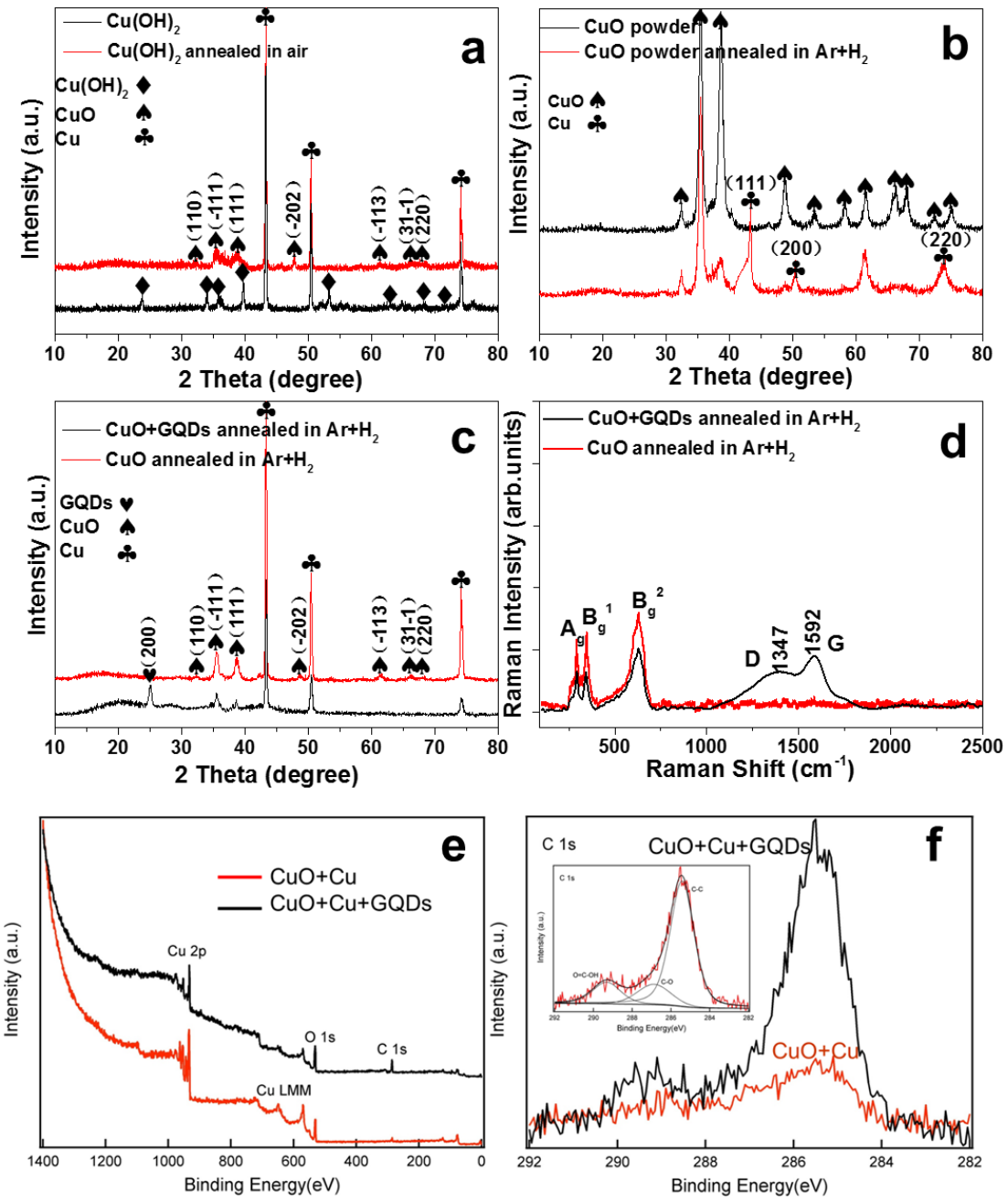

Figure 2.2.4 XRD pattern of a) anodized $Cu(OH)_2$ source material and CuO after annealing of the former sample, b) purchased CuO powder and the powder annealed in $Ar+H_2$ under 200 ^oC for 0.5 h and c) CuO and CuO+GQDs annealed in $Ar+H_2$ under 200 ^oC for 0.5 h. d) Raman spectra of CuO and CuO+GQDs annealed in $Ar+H_2$ under 200 ^oC for 0.5 h. XPS pattern comparison of sample CuO and CuO+GQDs annealed in $Ar+H_2$: e) Wide scan; f) C 1s peaks. Inset is the C 1s spectra from CCG triaxial nanowires with fitting results.

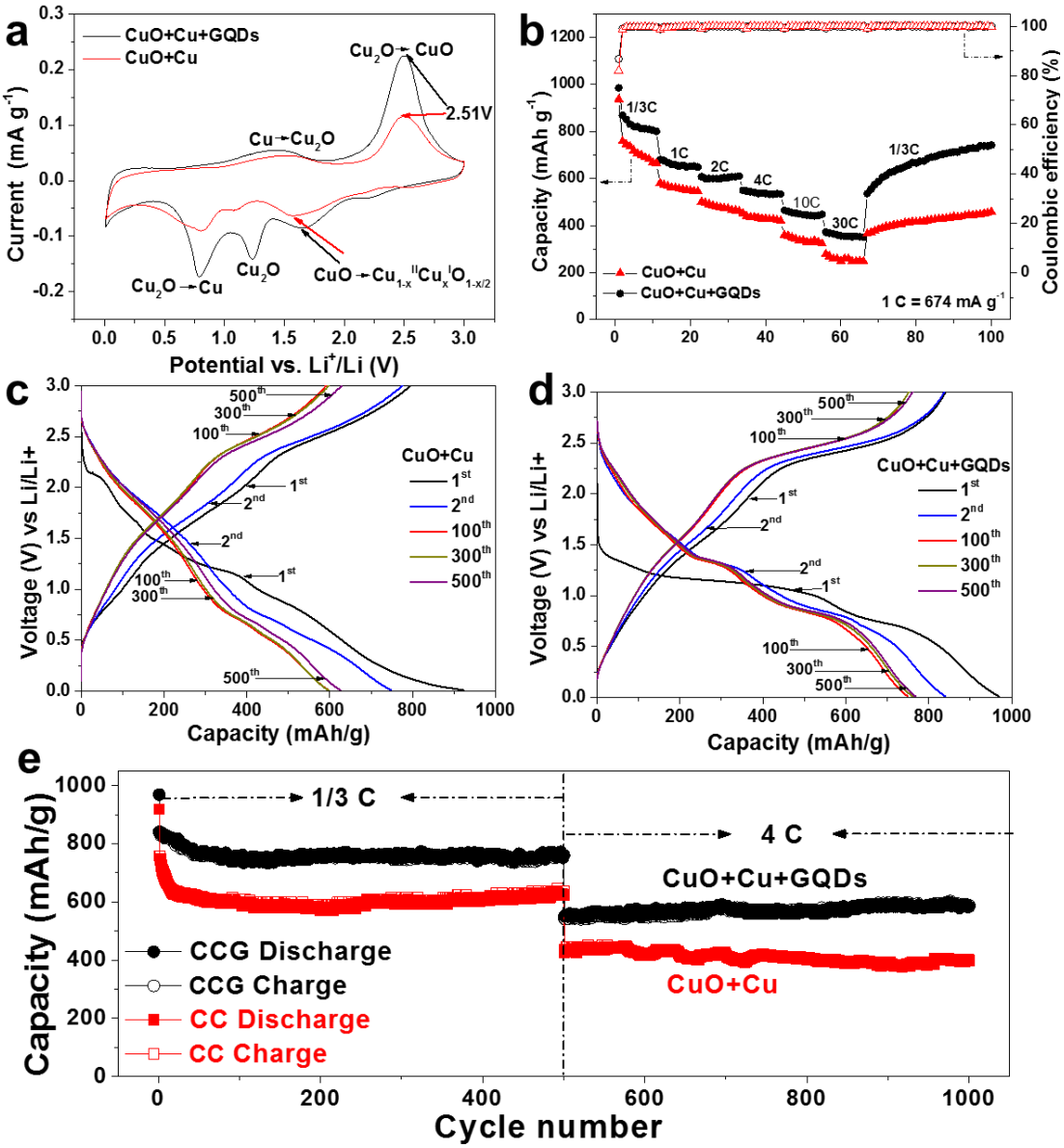

Figure 2.2.5 Electrochemical characterization of CC and CCG anodes. a) CV curve. b) Rate performance and coulombic efficiency. c) and d) Charge-discharge curves (current density: 225 mA g^{-1}, which is 1/3 C) at different cycles for CC and CCG nanowire electrode, respectively. e) Cycling performance at 1/3 C for the first 500 cycles and 4C for the rest 500 cycles. All the specific capacities are calculated based on the total mass of the active materials (CuO, Cu and GQDs in the CC and CCG nanowires).

To figure out the advantages of the entire structure design methodology, we conducted the test of full electrochemical properties comparisons of the triaxial CCG nanowire and coaxial CC nanowire anodes. First of all is the cyclic voltammetry (CV)

test of both anodes in a coin cell against Li plate. As can be observed from the Figure 2.2.5a, three cathodic peaks are located at 1.8, 1.25 and 0.78 V and corresponded to the three discharge plateaus in the charge-discharge curves in Figure 2.2.5d of 2.0–1.5 V, 1.5–1.01 V and 1.01–0.01 V for the CCG nanowires anode, respectively. According to the literature, these peaks should correspond to the formation of $Cu_{1-x}^{II}Cu_x^{I}O_{1-x/2}$, Cu_2O and Cu respectively, as shown in the follow equations:[104, 125]

$$CuO + 2Li^+ + 2e^- \leftrightarrow Cu + Li_2O \quad (1)$$

$$CuO + xLi^+ + xe^- \rightarrow Cu_{1-x}^{II}Cu_x^{I}O_{1-x/2} + \frac{x}{2}Li_2O \quad (2)$$

$$Cu_{1-x}^{II}Cu_x^{I}O_{1-x/2} + (1-x)Li^+ + (1-x)e^- \rightarrow \frac{1}{2}Cu_2O + \frac{1-x}{2}Li_2O \quad (3)$$

$$\frac{1}{2}Cu_2O + Li^+ + e^- \rightarrow Cu + \frac{1}{2}Li_2O \quad (4)$$

Equation (1) is the overall reaction progress which can be divided into three sub-procedures as shown in following Eq. (2–4). Two anodic peaks of 2.51 and 1.52 V correspond to two charge plateaus of 1.75–2.8 and 0.01–1.75 V responsible for the formation of Cu_2O and CuO separately.[105]

As comparison, the CCG anode exhibits better rate property than the CC anode (Figure 2.2.5b). The specific capacity retention for the CCG triaxial nanowires anode is ~ 42.3% when current density varies from 1/3 C (780 mAh g^{-1}) (1 C = 674 mA g^{-1}) to 30 C (330 mAh g^{-1}). While for the CC coaxial anode, the capacity retention is only ~ 28 % at the same current density change. Besides, the specific capacity of CC anode is lower at each rate from 1/3 C to 30 C. After went to high rates for several cycles, we applied the same current density as the start of the test which is 1/3 C. The CCG triaxial nanowires anode shows a higher capacity recovery (~85 %) more than the CC coaxial anode (~70 %) after recovered from the high current density of 30 C.

As was discussed in the introduction part, the CuO related anodes usually suffer from low initial coulombic efficiency due to the formation of SEI layer and the volume expansion (174 %) of CuO. In our design, the additional metallic Cu layer can protect the inner CuO as well as suppress the SEI formation at the 1st discharge process (CuO → Cu). Besides, this Cu layer can also compensate for the charge capacity because of the anodization of Cu (Cu → CuO) during charging. Moreover, the outer GQDs layer

will further prevent the forming of SEI layers. As a result, the trilayered CCG electrodes achieved a high initial coulombic efficiency of ~ 87 % higher than that of bare CuO ~ 82 % which is only with the single Cu layer protection.

To see the cycling stability, charge-discharge curves of both CC (Figure 2.2.5c) and CCG (Figure 2.2.5d) were plotted with 1^{st}, 2^{nd}, 100^{th}, 300^{th} and 500^{th} cycles. As can be seen in Figure 2.2.5c and d, the charge-discharge curves of 500^{th}, 300^{th} and 100^{th} cycles are almost overlapped with each other, which indicates the good cycling stability both CuO based anode materials. It is obviously that the CCG electrode has a much stable charge/discharge plateau than that of CC anode, implying less electrochemical polarization resulted from the better electric conductivity and of CCG anode. To figure out the special structure stabilizing benefits of GQDs, the long-term cycling properties were tested for both electrodes with the same current densities as shown in Figure 2.2.5e. The cycling tests were performed up to 1000 times with the first 500 cycles tested at 1/3 C and the rest 500 cycles at 4C for the CCG and CC nanowire anodes. There is a fierce capacity drop (~ 35 %) during the first 80 cycles or the CC coaxial nanowires anode unlike the CCG nanowires anode which shows less than 20 % capacity drop lasting to even 300 cycles. These sharp capacity drop was observed in previous work, where possible reasons were given as the poor electric conductivity of the electrode material and the serious decomposition problem of the active materials.[85, 86, 126] However, slight capacity increase was also detected after 200 cycles which is similar to the reported study of oxide anode materials such as CuO,[104] SnO_2[127] and Fe_3O_4.[128] In the literature, it was proposed that the increased capacity should be ascribe to some side reactions that exhaust electrolyte and form side products of Li_2O, LiOH and LiH during lithiation process.[129] Regarding the property of our CuO based electrode, other possible reason can be the oxidation of Cu shell to CuO which will add to the active material during charging, because the as transferred CuO can act as the fresh active material and contribute to the overall capacity. There is a sudden drop of capacity from the 1/3 C to 4 C caused by the huge current density increase. During the longer cycles (> 500 cycles) at higher current density (4C), there is an obvious capacity fade

of the CC electrode. In contrast, the GQD-protected electrode successfully maintained its overall capacity all the way to 1000 cycles without obvious capacity drop. This should be the positive effect of GQDs to suppress the volume expansion of CuO active material and stabilize the entire electrode structure as can be verified by the SEM images of the CCG samples after cycles showing the well preserved rough wire morphology of the electrode (Figure 2.2.6b inset). While the CC nanowires were suffering serious volume expansion especially with the continuous exhausting of Cu protection layer, the CC nanowires shows serious aggregation problems as was shown in the Figure 2.2.6a inset. The positive effects of GQDs are further verified by the Nyquist plots of CCG and CC anodes before and after 500 cycles (Figure 2.2.6). The resistance is simulated using equivalent circuit of $R_S(Q(R_{ct}Z_W))$ as was shown in Figure 2.2.6b the inset, where R_{ct} is the charge transfer resistance; R_S is the ohmic resistance of solution and electrodes; Z_W is the Warburg impedance and Q is the double layer capacitance. With careful simulation, the R_{ct} of samples at different stages were given. It is clear that the charge transfer resistance of both CC (285 Ω) and CCG (108 Ω) increased after 500 cycles (pristine samples of CC: 75 Ω; CCG: 50 Ω). Comparing the CCG and CC anodes, it is clear that the CCG anode shows much lower charge transfer resistance both before and after cycling (before cycling: Rct value of CCG: 35 Ω while that of CC: 72 Ω; after cycling: Rct value of CCG: 119 Ω while that of CC: 291 Ω). The lower electrochemical resistances indicate a faster surface charge transportation and a higher Li^+ ion diffusing efficiency according as was reported previous work.[130] The lower Rct also indicates less formation of SEI which in return will lead to a less electrode material and electrolyte waste and thus a higher capacity. This is manifested by the electrical resistance test of Cu foam substrate, sample of CuO, CC and CCG as plotted in Figure 2.2.7a. As can be seen clearly, with the adding of Cu and GQDs layer, the conductivity increased greatly compared with the bare CuO sample. The CCG sample exhibits the lowest resistance among CuO and CC samples which implies the conductivity enhancement effect of GQDs layer. Figure 2.2.7b-e shows the real photos of the samples at different stages from the original Cu(OH)2, to CuO, CuO+Cu and

CuO+Cu+GQDs anodes. The colors changed from blue to red and finally black of the CCG samples.

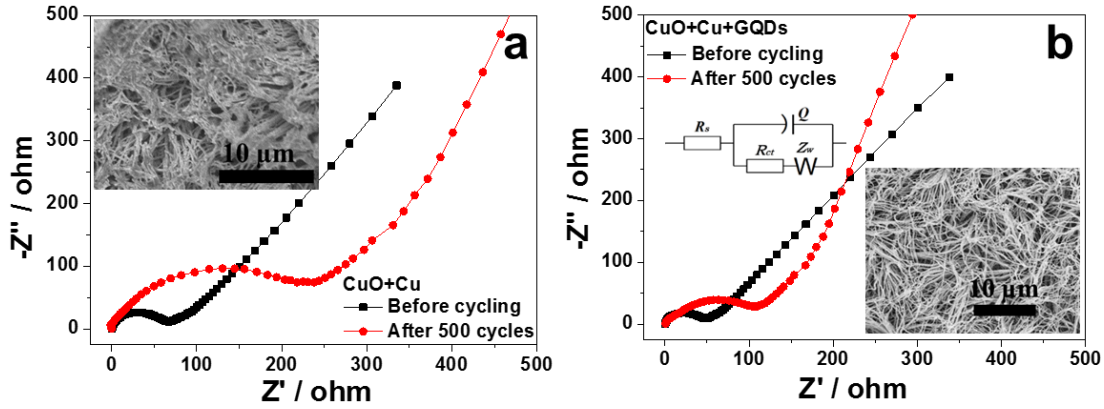

Figure 2.2.6 Electrochemical impedance spectroscopy test and analysis. Nyquist plots of a) CC and b) CCG nanowires anodes comparisons of the sample before and after 500 cycles, respectively. Inset images are the SEM images of the related samples after 500 cycles.

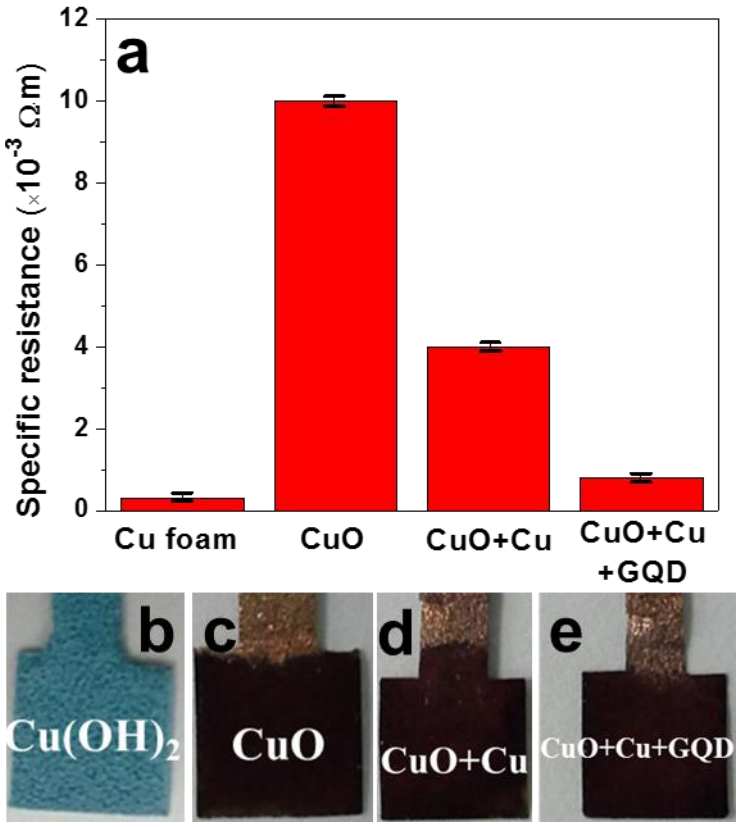

Figure 2.2.7 a) Electrical resistance of Cu foam substrate, samples of CuO, CC and CCG anode calculated over five specimens for each sample with the error bars for standard deviation shown in

the figure. b-e) real photos of $Cu(OH)_2$, CuO, CC and CCG samples.

2.2.4 Conclusion

In this chapter, we presented the fabrication of a novel copper oxide/Cu/graphene quantum dots (CuO/Cu/GQD) triaxial nanostructure electrode and applied it as Lithium-ion battery anode. The as obtained electrodes exhibited ultra-stable and ultra-fast Li ion storage properties leading to the higher capacity, better rate capability and cycling stability than the control sample of CuO/Cu nanowires. As was proved in the results discussion part, both Cu and GQDs layers play important roles in electrochemical performance enhancement. The final CCG triaxial nanowire electrodes exhibit high capacity retention in the first 100 cycles and a high rate capability with high capacity retention achieved after cycled at super high rate of 30 C. Moreover, a high initial coulombic efficiency of 87% is achieved which should be resulted from a synergetic contribution of the Cu and GQDs layers. These performance improvements indicate that GQDs is suitable to be applied in LIB electrode materials. This work unveils the potential application of GQDs in other rechargeable batteries.

Nanomaterials as lithium-ion battery electrode show decent battery performance. However, this fascinating performance are based on low electrode material mass loading beneath 5 mg/cm2 which trigger a concern about the industrialization besides its high cost. Moreover, the regarding the anode research, suitable materials which exhibit low voltage beneath 1 V should be more studied considering the final match with practical cathode materials. In the future research, low-cost fabrication method should be studied as well as increasing the active material loading to push nanomaterials further forward to the practical applications.

Chapter 3 Metal Nitrides for Supercapacitors

3.1 Solid state Asymmetric Supercapacitor device based on Fe_2N anode and TiN cathode

3.1.1 Introduction to metal nitride materials in supercapacitors

Due to the fast energy delivery capability (up to tens of seconds) of supercapacitor and the ultra-long cycle life (~ 10^5 cycles), supercapacitors stand out as a highly promising system among all the electrochemical energy storage devices.[131-134] However, compared with the traditional battery systems, supercapacitor is of relatively low energy density, particularly with carbon materials as the electrode materials.[135-137] Normally, in asymmetric supercapacitors (ASCs) devices, the energy density can be improved greatly since the working voltage of the full devices is enlarged according to $E = \frac{1}{2}CV^2$.[138-142] Previous research on ASCs has mainly been focused on utilizing metal oxides as electrode active materials due to their high pseudo-capacitance in a fast reversible redox reactions. But the low electrical conductivity and stability always make metal oxides suffer from high capacitance fading in long cycles. Therefore, recently, metal nitrides are attracting more attentions because of their superb electrical conductivity (4000–55500 S cm^{-1}) and improved sustainability.[143, 144]

Among all the reported work on metal nitrides, Fe_2N and TiN received majority attention due to their high conductivity and theoretical capacitance (TiN as supercapacitor cathode: ~ 150 F g^{-1}; Fe_2N as lithium ion battery anode: ~ 900 mAh g^{-1}).[145, 146] Although Fe_2N has been studied in lithium ion batteries [147, 148] as an anode materials, the non-obvious charge-discharge voltage plateaus[147] indicates its capacitive property and thus should be considered to be a suitable electrode material for the supercapacitor applications. While for TiN, varies types of nanostructures have

been successfully fabricated and tested as supercapacitive electrode (one dimensional nanoparticle;[143] two dimensional: nanotube,[149-151] mesoporous microsphere[152] and nanosheets).[153] Still, TiN was reported to be easily oxidized in water based electrolytes ($TiN + 2H_2O \rightarrow TiO_2 + \frac{1}{2}N_2 + 4H^+ + 4e^-$, $2TiN + 2O_2 \rightarrow 2TiO_2 + N_2$).[154] Thus, to reduce the oxidation problem, TiN is always combined with carbon materials and conductive polymers. Methods has been tried with carbon nanotube encapsulation[155, 156] and carbon coating[154, 157, 158]; graphene wrapping;[159-162] forming core-shell structures with other materials such as TiO_2,[163] VN,[164] and MnO_2;[165] decoration with polymers such like polypyrrole,[166] polyaniline,[167, 168] and PEDOT.[169] Those methods expressed excellent effects in improving TiN stability.

Regarding substrate materials, graphene stands out because of its large surface area, high conductivity and light-weight property.[170] However, the stacking problem of graphene always result in large waste of its surface area. Thus, making vertically aligned graphene nanosheets (GNS) which can alleviate the problem greatly is of great importance since the increased surface area can lead to a high capacitance (for electro-double-layer-capacitance: the available active surface sites are favored for charge absorption; pseudo-capacitance: redox reactions relies highly on surface area). As was reported, the GNS substrates have been applied to growing ZnO and SnO_2 as LIB anode materials and showed improve LIB performance.[171, 172] But large surface area also means more solid-electrochemical-interlayer which can be bad for a battery performance. Thus, in our consideration, the GNSs should be more suitable as supercapacitor substrate materials.

Therefore, in this chapter, metal nitrides nanostructures are fabricated on GNSs substrate for a high-power, high energy and ultra-stable solid state ASCs. During the fabrication, Atomic layer deposition (ALD) was introduced for source material deposition since it can assure the maximum use of the conductive GNS surfaces and source materials will fully cover with substrate with a tight connection.[173] To avoid the oxidation problem of metal nitrides in aqueous electrolyte, poly(vinyl alcohol) (PVA)-based solid state electrolyte was utilized.[174-176] As a result, the ASCs device

constructed with Fe_2N@GNSs anode, TiN@GNSs cathode and PVA)-LiCl gel electrolyte exhibits high irreversible capacitance of ~ 58 F g^{-1} at 4 A g^{-1} and is stable within 20,000 cycles. Moreover, the devices obtain both high energy density (~ 0.55 mWh cm^{-3}) and power density (~ 220 mW cm^{-3}) at a high current density (~ 8 A g^{-1}).

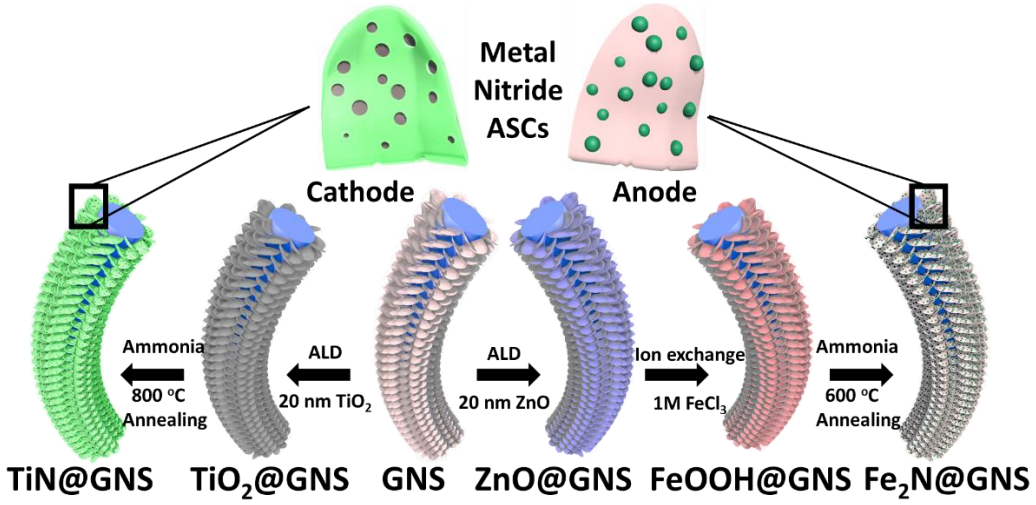

Figure 3.1.1 Illustration of experimental design

As was shown in Figure 3.1.1 the illustration of the fabrication processes of electrode materials, thin films of 20 nm TiO_2 and ZnO were coated by ALD to the GNS substrates as cathode and anode source material, respectively. Detailed synthesis method and process will be discussed in next part the experiments and methods.

3.1.2 Experiments and methods

Fe_2N@GNS Anode preparation: All chemicals were bought from Sigma Aldrich and used directly without purification. Graphene nanosheets (GNS) (area per mass: 467 m^2 g^{-1}) were provided by INCUBATION ALLIANCE, INC. as the substrate. Before ALD, the GNS substrates were treated with oxygen plasma at 200 W for 10 minutes with an O_2 gas flow of 100 sccm, 70 mTorr. Regarding the anode material synthesis, it is mainly an atomic layer deposition (ALD) plus ammonia annealing process. First, sacrificial material ZnO (20 nm) was deposited on GNS (with oxygen plasma

pretreatment) with ALD under 200 °C. To have a thorough transformation from ZnO to FeOOH, the ZnO@GNS was then immersed in 1 M $FeCl_3$ solution for 2 h.[177] The anode material of Fe_2N@GNS was finally gained by annealing the FeOOH@GNS sample in NH_3 atmosphere at the temperature of 600 °C. A piece of FeOOH@GNS with a unified size (0.6×1 cm^2) was taken as the control sample.

TiN@GNS Cathode preaparation: The cathode fabrication process is also composed of two steps: first, TiO_2 deposition by atomic layer deposition (ALD); and second, transferring to nitride through annealing in ammonia (NH_3) atmosphere. In a typical ALD (Beneq TFS 200) process, 120 °C was selected as the deposition temperature for TiO_2 with $TiCl_4$ and water as the titanium and oxygen source, respectively. To obtain 20 nm TiO_2 coating, 166 cycles (~ 1.2 Å per cycle) deposition process was conducted when the reaction chamber was maintained at a steady N_2 steam of 300 sccm (cubic centimeter per minute) under 1.0 mbar. The sample of TiO_2@GNS was then annealed in NH_3 atmosphere at 800 °C for 1 h with a gas flow of 50 sccm and heating rate of 20 °C per minute. A piece of TiO_2@GNS with a unified size (0.6×1 cm^2) was taken as the cathode control sample.

GNS capacitance contribution exploring: Two pieces of bare GNS substrates with the unified size (0.6×1 cm^2) were put into the ammonia atmosphere and annealed in 800 and 600 °C separately. The CV curves of bare GNS, GNS annealed in 600 and 800 °C were tested with the control sample as working electrode, Ag/AgCl as reference electrode and Pt as counter electrode in 1 M LiCl aqueous electrolyte.

Morphology and Structural Characterization: The morphologies of all the control samples and anode and cathode were imaged by SEM (JEOL 2100) conducting at 5 kV. Detailed morphologies were characterized by the HRTEM (JEOL JEM-2010F) which operates at 200 kV. The detailed crystal structures of all the samples were verified using XRD (RigakuD/Max-2550 with Cu Kα radiation) and XPS measurements (performed with a VG ESCALAB 220i-XL system using a monochromatic Al Ka1 source (1486.6 eV)). Raman spectra was obtained with a WITec-CRM200 Raman system at a laser wavelength of 532 nm (2.33 eV). To calibrate the wavenumber, the Si peak at 520 cm^-

[1] was applied as the reference.

Device assembling and electrochemical performance test

For single electrode performance study, a standard three-electrode testing system was built with the as synthesized anode/cathode as working electrode, a piece of platinum as counter electrode and Ag/AgCl as reference electrode in 1M LiCl aqueous electrolyte. Full devices were made into standard two-electrode system with Fe_2N@GNS as anode, CKK membrane as separator, 1 M LiCl-PVA as electrolyte and TiN@GNS as cathode. Detailed steps are: first, a piece of Fe_2N@GNS anode was put on a transparent plastic film (5 x 6 cm^2); second, NKK membrane was dipped in LiCl-PVA electrolyte for 5 mins to be penetrated thoroughly by the gel electrolyte before being put on the top of the anode; third, a piece of TiN@GNS cathode was soaked in the LiCl-PVA gel electrolyte for 5 mins and put on the top. Both electrodes were conducted with Pt wire as the conducting current collector. The whole device was then sealed with transparent tape before the testing.

Calculations of gravimetric capacitance, energy density and power density

1. Capacitance calculated based on CV curves and charge-discharge curves, please refer to the equations in Chapter 1, equation (1) and (2), respectively.

2. Calculation of energy density and power density of full device

Volumetric energy density (E_{volume}, mWh cm^{-3}) and power density (P_{volume}, mW cm^{-3}) were calculated from the discharge curves as the follows:

$$E_{volume} = \frac{1}{2}\frac{CU^2}{V} = \frac{I\Delta tU}{2\times 3600\times V} \quad (7)$$

$$P_{volume} = \frac{E_{volume}}{\Delta t} = \frac{1}{2}\frac{IU}{V} \quad (8)$$

Where I (mA) is the discharge current (constant), Δt (s) is the discharge time (divided by 3600 to transfer the unit to h), U (V) is the maximum cell operating voltage (1.6 V), V is the volume (cm^3) of the ASC full device (including the active electrode

material, the solid state electrolyte/separator and the GNS substrate).

Determination of mass loading

The homogeneous GNS substrate (7×7 cm^2) were provided by the Incubation Alliance Inc. The substrate was then cut into three pieces and divided for different usage (anode fabrication: 7×3 cm^2, marked as GNS-A; cathode fabrication: 7×3 cm^2, marked as GNS-C; control experiment: 7×1 cm^2, marked as GNS-B). To reach the maximum accuracy, an analytical balance (RADWAG, MYA 21, resolution: 1 μg) was used to weigh the mass of each sample before and after the whole related dealing process. All the samples were dried thoroughly at 80 ºC for 24 h before weighing. The mass loading of active material (anode: Fe_2N and cathode: TiN) were calculated by mass difference dividing the total area (21 cm^2). The mass values and active material mass density were listed below in table 3.1.1. Thus, it is clear that the mass loading of Fe_2N and TiN and are ~ 0.8 and ~ 0.5 mg cm^{-2}, respectively.

Table 3.1.1 Mass of samples after related dealing steps

Sample	**Mass before dealing (mg)**	**Mass after annealing (mg)**	**Mass density (mg cm^{-2})**
GNS-C	351.429	362.375	0.521
GNS-A	351.424	368.229	0.809
GNS-B	117.143	117.151	

Balance the charge of electrodes in MNASC device

As for a full device, anode and cathode should be balanced to achieve the best performance. In asymmetric supercapacitor device, the charge balance should follow the relationship $Q^+ = Q^-$. The charge stored by each electrode charge can be described as:

$$Q = C_m \times m \times \Delta E \qquad (9)$$

where C_m is the specific capacitance, ΔE is the potential range for the charge/discharge process and m is the mass of the electrode active materials.

It is noted that, at 40 mV s^{-1}, the mass balancing of cathode to anode can be calculated as:

$$\frac{m_{Fe_2N}}{m_{TiN}} = \frac{C_+ \times \Delta E_+}{C_- \times \Delta E_-} = \frac{170.5 \times 0.8}{118.5 \times 0.8} = 1.44 \qquad (10)$$

Therefore, the calculated mass ration between the Fe_2N anode and TiN cathode is about 1.44, which is very closed to the mass loading ratio of the Fe_2N and TiN (0.809 : 0.521 = 1.55). Thus, the same area of anode and cathode can be used in the full device as a well-balanced full device.

3.1.3 Results and discussions

In this study, graphene nanosheets (GNS) which vertically aligned on the surface of carbon fiber is applied as substrates (thickness: ~ 5 nm, figure 3.1.2 a and b). Compared with anode (Fe_2N) and cathode (TiN), the capacitance contribution from GNS substrates are negligible (less than 0.01 % considering the areas of CV curves, figure 3.1.2 c, detailed testing procedures are presented in experimental part).

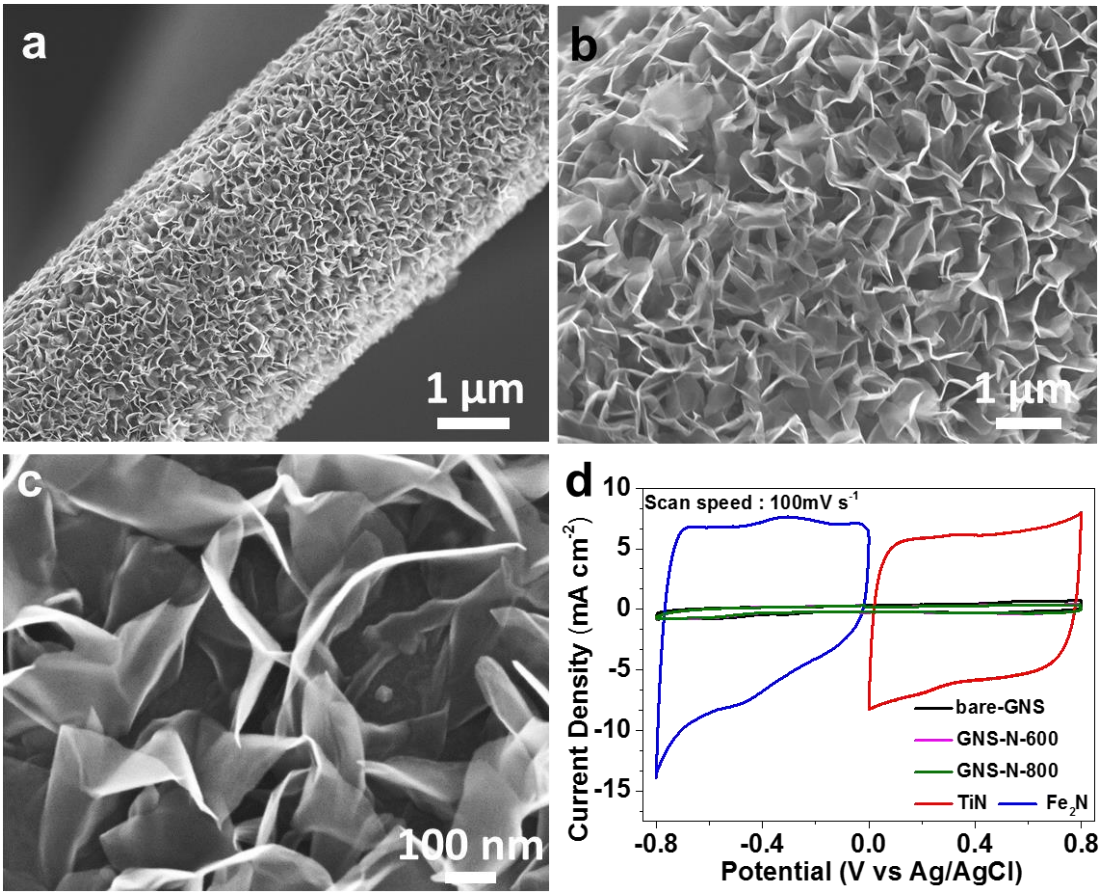

Figure 3.1.2 a) - c) SEM images of graphene nanosheets substrate at different magnification. c) **Analysis of possible capacitance contribution from substrates under different annealing circumstances.** CV curves comparison of bare-GNS, GNS annealed in ammonia at 800 °C (GNS-N-800) and 600 °C (GNS-N-600), Fe_2N and TiN electrode tested in a standard three-electrode system

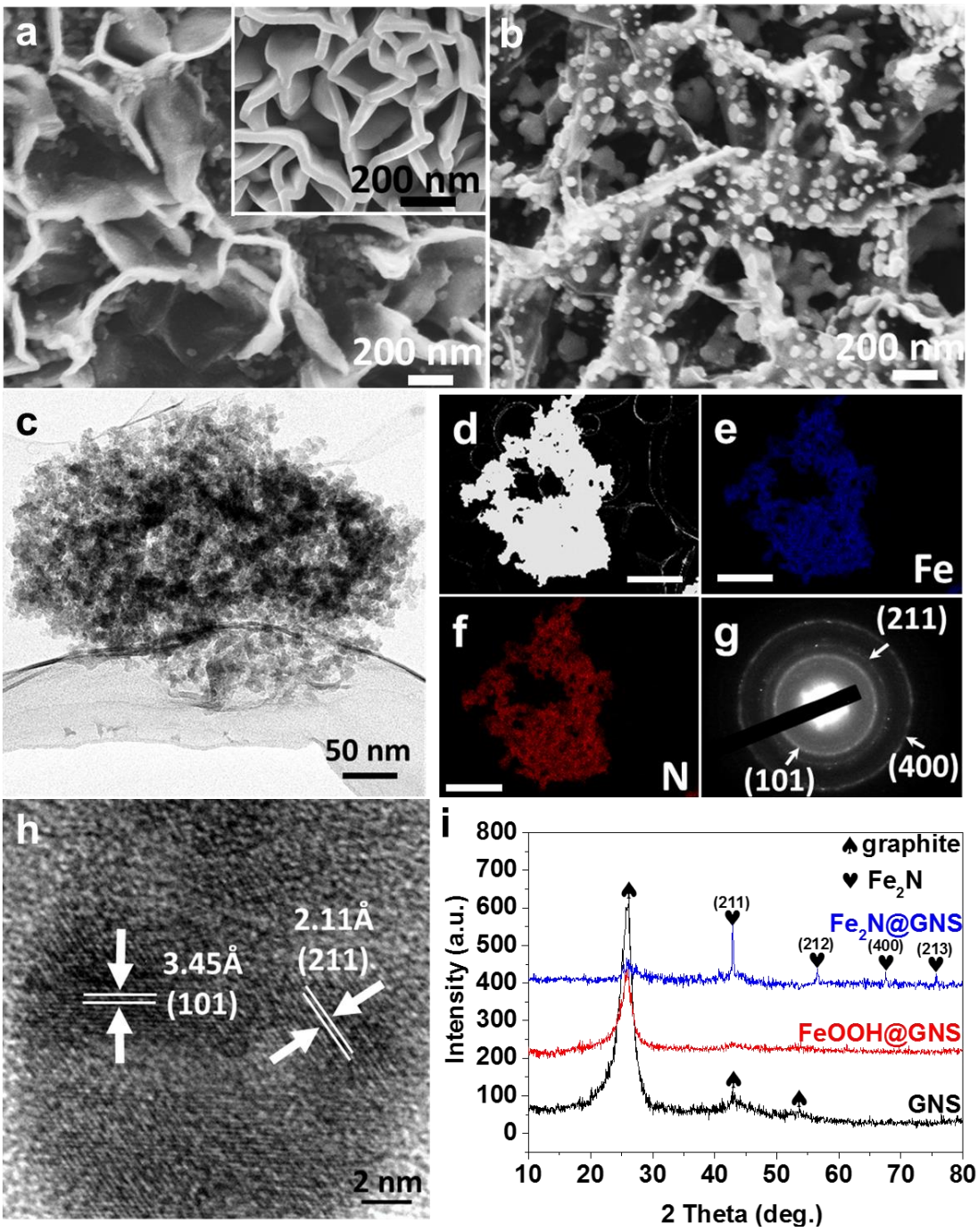

Figure 3.1.3 Morphology and structure of Fe_2N anode. SEM images of a) FeOOH@GNS (inset is the sample of ZnO@GNS) and b) Fe_2N@GNS. c) TEM image of Fe_2N particles. d-f) TEM elemental mapping of Fe_2N particles (scale bar, 50 nm). g) SAED pattern showing (211), (101) and (400) lattice planes of Fe_2N. h) HRTEM image of Fe_2N showing the (211) and (101) lattice planes of Fe_2N. i) XRD patterns of the sample at different fabrication stages.

The anode was synthesized through a template sacrificing method in which the

ZnO@GNS acting as a sacrificial template (Figure 3.1.3a inset) was dipped in 1 M $FeCl_3$ solution for 2h. The thin film becomes thinner with a thickness ~ 10 nm (Figure 3.1.3a), which is as reported to be FeOOH@GNS.[178] After the ammonia annealing, the FeOOH thin film is converted to Fe_2N nanoparticles that are dispersed uniformly on the surface of GNS (Figure 3.1.3b) with an average diameter ~ 10 nm. Figure 3.1.3c showed the fine-particle morphology of Fe_2N with a diameter ~ 10 nm. TEM mapping of element Fe (blue, Figure 3.1.3e) and N (red, Figure 3.1.3f) correspond well with the image profile of Fe_2N particles in Figure 3.1.3 d. Selected area electron diffraction (SAED) pattern (Figure 3.1.3g) showed polycrystalline nature of the Fe_2N according to the series of well-defined rings which are assigned to various diffraction planes of (101), (211), and (400) of face centered cubic (fcc) structure of Fe_2N. HRTEM image (Figure 3.1.3h) presented the clear lattice fringes with d-spacings of 2.11 and 3.45 Å which conforms well to the crystal face of (101) and (211), respectively. XRD spectrum of sample at different fabrication stage were provided in Figure 3.1.3 i to demonstrate the transformation process of the anode material. The comparison clearly showed that the pure phase of Fe_2N was successfully achieved after the transformation reaction of amonia annealing. The related diffraction peaks of 43°, 56°, 68°, and 75° were well matched to fcc Fe_2N lattice of (211), (212), (400), and (213) (JC-PDS, #06-0656).[148, 179]

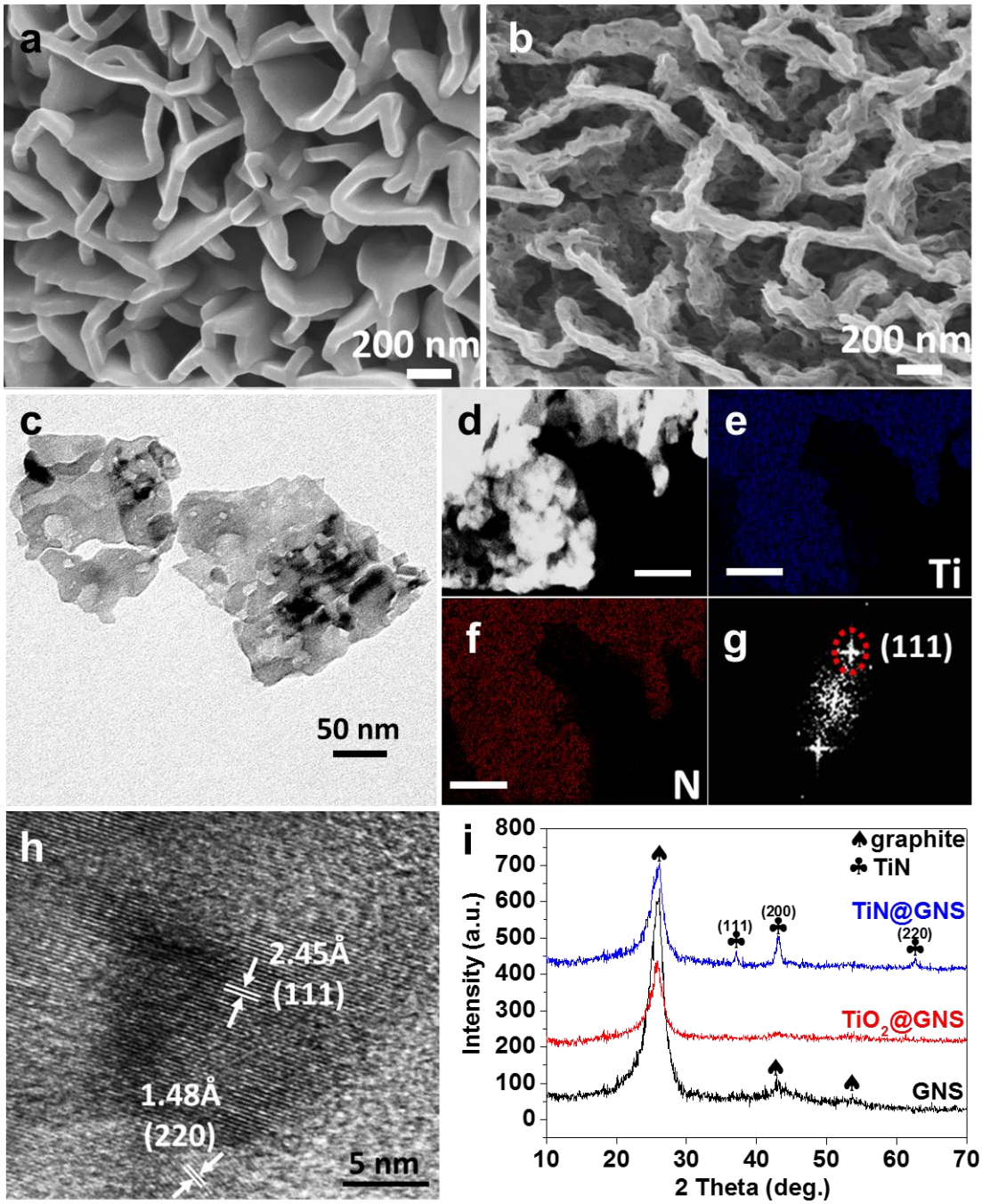

Figure 3.1.4 Morphology and structure of TiN cathode. SEM images of a) TiO_2@GNS and b) TiN@GNS. c) TEM image of TiN sheet. d-f) TEM elemental mapping of TiN (scale bar, 50 nm). g) FFT pattern corresponding to the (111) lattice in (h) and (i). h) The HRTEM image of TiN showing the (111) and (220) lattice planes of TiN. i) XRD spectra of the cathode material at different fabrication stages.

Same characterization was conducted to the cathode material. The smooth surface (Figure 3.1.4a) of the original ALD TiO_2@GNS becomes porous (Figure 3.1.4b) after the annealing process which is expected to enlarge the specific surface area and in return leading to an increased capacitance. In order to reveal the detailed nanostructure and phase of the electrode materials, transmission electron microscopy (TEM) characterizations were conducted. As can be seen in Figure 3.1.4c, TiN shows the pore size varying from 3-10 nm. High resolution transmission electron microscopy (HRTEM) reveals the lattice of (111) planes (d-spacing 2.45 Å) and (220) ones (d-spacing 1.48 Å) of TiN (Figure 3.1.4h), which is in agreement with the fast Fourier transfer (FFT) generated from the same area (Figure 3.1.4g). Furthermore, TEM mapping exhibited the consistent element distribution of Ti (Figure 3.1.4e) and N (Figure 3.1.4f) with the dark field TEM image in Figure 3.1.4d. To track down the transition process, XRD spectra of bare GNS after oxygen plasma (see the detailed experimental process in part 3.1.2), GNS after 20 nm TiO_2 ALD, and TiO_2@GNS after amonia annealing were plotted together in Figure 3.1.4i. Three typical peaks of graphite were detected clearly in the XRD spectrum of bare GNS. After the coverage of ALD added TiO_2, two weaker peaks (located at 44 ^{o} and 54 ^{o}) of graphene were almost disapeared. Due to the amorphous property of ALD deposited material, peaks of TiO_2 was not detected. After high temperature annealing in pure NH_3 gas atmosphere, three diffraction peaks of fcc TiN at 37^{o}, 44^{o} and 63^{o} appear and correspond well to the crystal face of (111), (200) and (220), respectively (JC-PDS, # 65-0715).[159, 180]

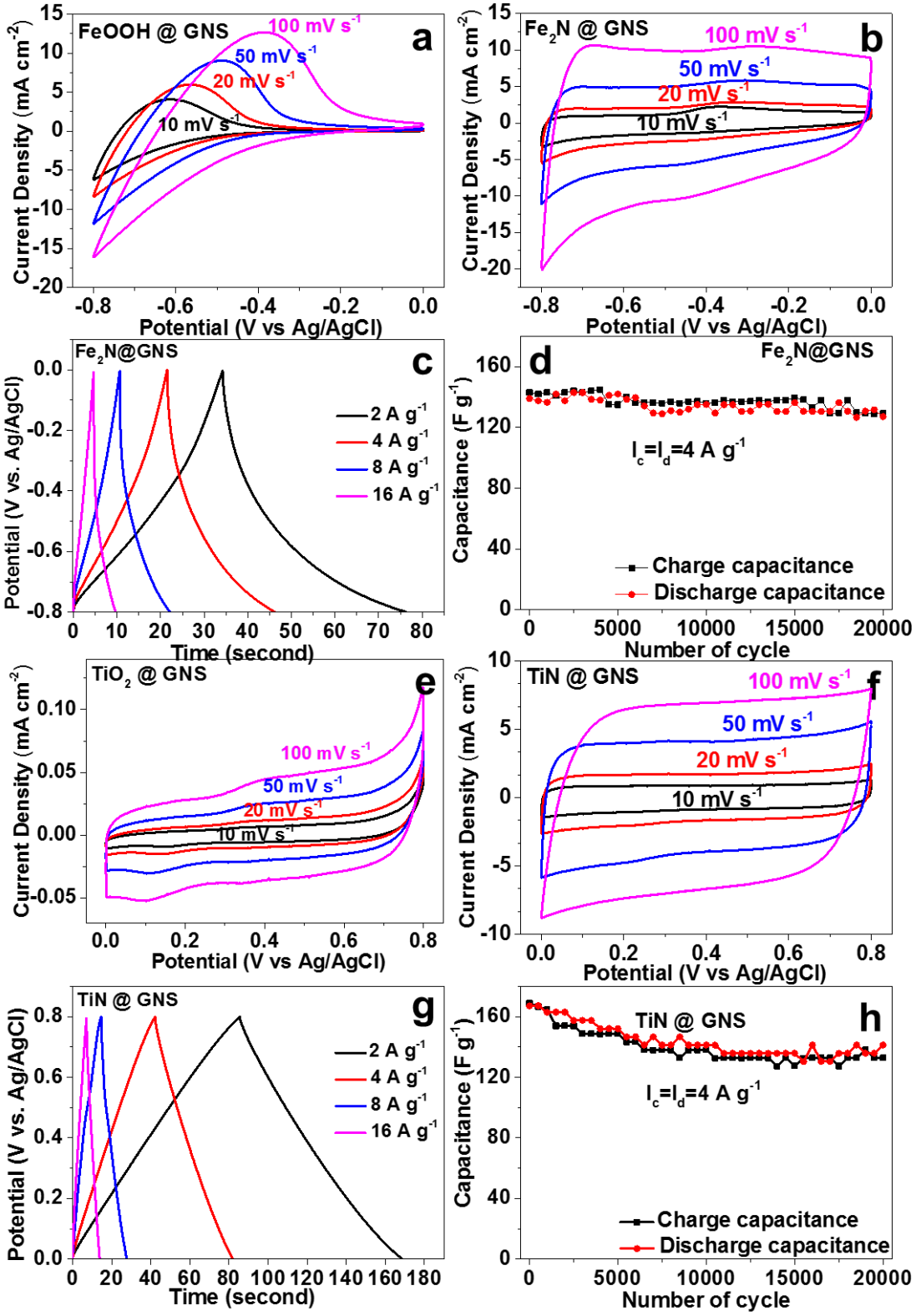

Figure 3.1.5 Electrochemical properties of single electrodes. CV curves of a) FeOOH@GNS, b) Fe_2N@GNS, e) TiO_2@GNS and f) TiN@GNS at different scan rates of 10, 20, 50, and 100 mV s^{-1}. Charge-discharge curves of c) Fe_2N@GNS and g) TiN@GNS at different current density of 2, 4, 8,

and16 A g^{-1}. Cycling performance of d) Fe_2N@GNS and h) TiN@GNS at 4 A g^{-1}. (All the electrochemical tests were conducted in a standard three electrode testing system with Ag/AgCl as reference electrode, Pt as counter electrode and related electrodes as working electrode, testing in 1 M LiCl electrolyte)

Figure 3.1.5a, b, e and f shows the CV curves of electrode source materials and electrodes (Anode source material FeOOH@GNS and Fe_2N@GNS anode were tested between -0.8 and 0 V vs. Ag/AgCl while cathode source material TiO_2@GNS and TiN@GNS cathode were tested between 0 and 0.8 V vs. Ag/AgCl) at different scan rate (10, 20, 50 and 100 mV s^{-1}). The comparison shows that the CV curves of precursor FeOOH (Figure 3.1.5a) and TiO_2 (Figure 3.1.5e) have much smaller curve area. The capacitances estimated from the CV curves for the source materials are about ten times lower than the corresponding electrodes. Both anode and cathode show quasi-rectangular shapes at different scan rates which indicates that the majority capacitance should be contributed by capacitive behavior. After calculating with the method discussed in Chapter 1.4.3, the capacitive contribution in anode and cathode are summarized and plotted in Figure 3.1.6. With no doubts, the capacitive contribution ratios increase with the scan speed. Further, under varied scan rates, the majority capacitance (over 50 %) are come from the capacitive behavior. The linear slopes and triangle shape of both anode (Figure 3.1.5c) and cathode (Figure 3.1.5g) corroborates the dominating capacitive property of the electrodes which is consistent with the conclusions made from the CV curves. Moreover, both electrodes exhibit high stability (capacitance retentions ~ 90 %) in long cycles of 20000 times with current density of 4 A g^{-1} (Figure 3.1.5d and h).

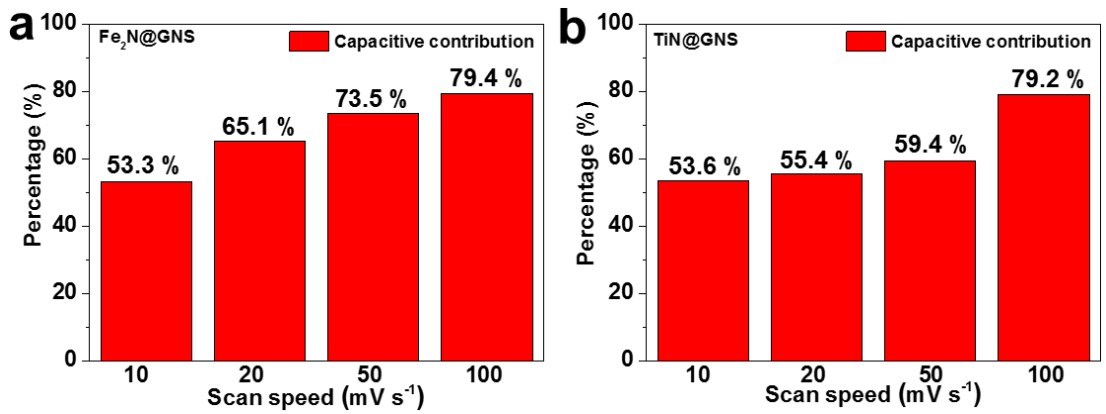

Figure 3.1.6 Capacitive behavior contribution to total capacitance of a) Fe_2N@GNS anode and b) TiN@GNS cathode under difference scan rate.

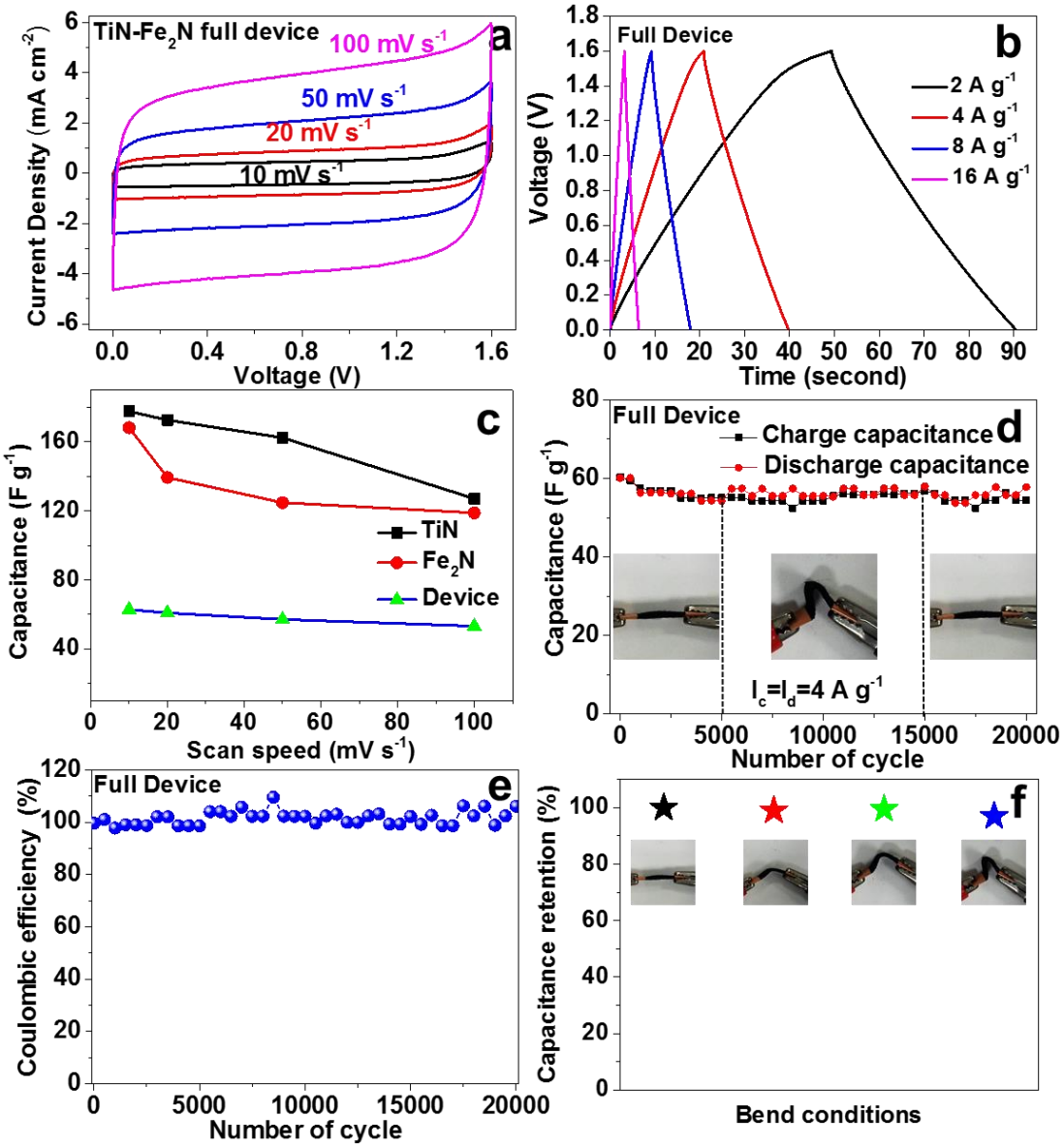

Figure 3.1.7 Electrochemical properties of Full device. a) CV curves, b) Charge-discharge curves, d) Cycling performance, e) Coulombic efficiency and f) Capacitance retention under different bending conditions of the full device. c) Capacitance comparison of TiN@GNS cathode, Fe_2N@GNS anode and full device at different scan rates of 10, 20, 50, and 100 mV s^{-1}. (The electrochemical tests of the full device were conducted with Fe_2N@GNS as anode, TiN@GNS as cathode, and LiCl-PVA quasi-solid-gel as electrolyte; The capacitances in Figure 3.1.7c are calculated based on Figure 3.1.5b for Fe_2N@GNS anode, Figure 3.1.5f for TiN@GNS cathode and Figure 3.1.7a for the full device; The mass here is the total mass of TiN and Fe_2N for calculation.)

Electrochemical performance of the ASC device is tested with Fe_2N as anode, TiN as cathode and PVA/LiCl as electrolyte in the range from 0 to 1.6 V at different scan rates (Figure 3.1.7a and b). CV curves of full device are of standard rectangle shape and the charge-discharge curves are of triangle shapes without obvious IR drop. Gravimetric capacitance at different scan rates were calculated based on Figure 3.1.5b, Figure 3.1.5f and Figure 3.1.7a and plotted in Figure 3.1.7c. In aqueous solution (1 M LiCl), the individual Fe_2N and TiN electrodes show high capacitance retention of ~ 77 % and ~ 80 %, respectively, with the scan rate increases from 10 to 100 mV s^{-1}. For the full device, a stable capacitance around 60 F g^{-1} is obtained with negligible capacity decay (less than 2 %) scanned from 10 to 100 mV s^{-1}. Regarding the cyclability test of the full device, the cycling performance was tested with ~ 70^o bending condition from 5000th to 15000th cycles and then recovered to flat state in the last 5000 cycles (Figure 3.1.7d). The capacitance value is nearly kept the same with or without bending of the reversible capacitance ~ 58 F g^{-1} in 20000 cycles. More bending tests were conducted and the capacitance retention is plotted in Figure 3.1.7f. As can be concluded from Figure 3.1.7d and f, bending has no effect towards the device cycling. Moreover, during the long cycles test, the full device kept the high coulombic efficiency of ~ 99 % which should be resulted from the ultra-high structural stability of the electrode active materials in the gel electrolyte as was mentioned in the introduction part of 3.1.1.

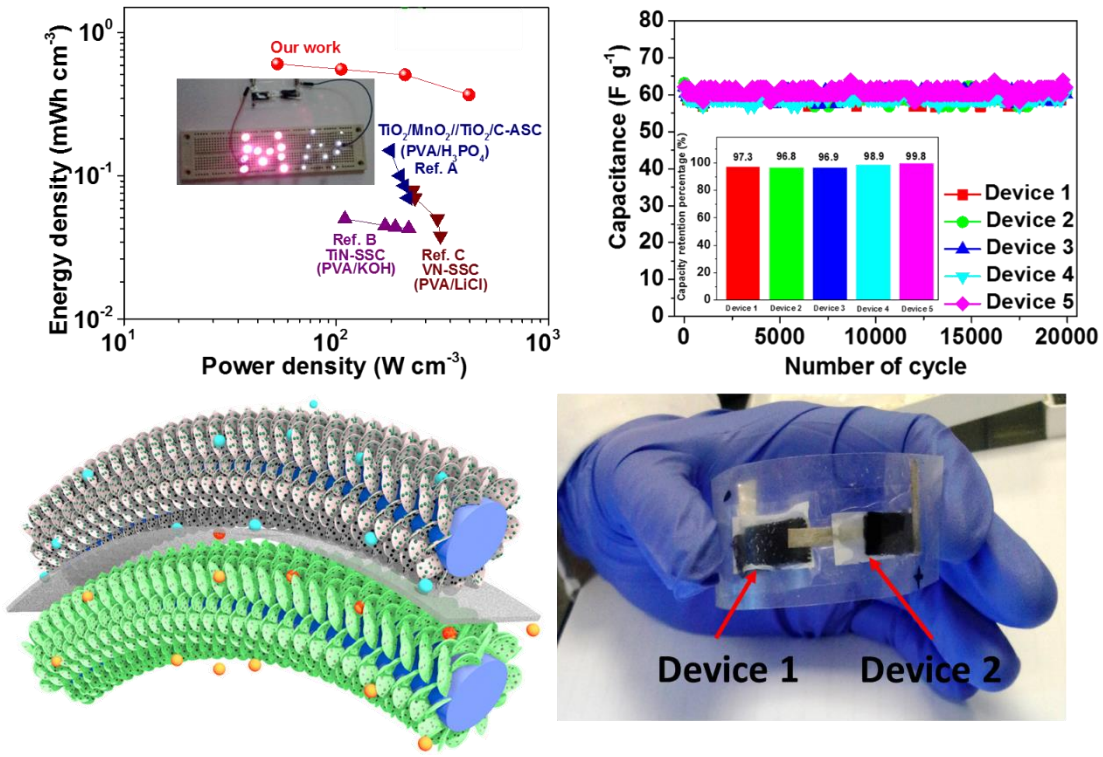

Figure 3.1.8 a) Ragone plot of ASC device comparing to other PVA-based SSCs and ASCs (Inset: pink and white LEDs in parallel with the profile of "MN" are lit up by two full devices in series). b) Cycling performance of five parallel devices tested at 4 A g^{-1} in 20000 cycles (Inset: figure of capacity retention percentage of each device). c) and d) the illustration and real photo of the ASC full device with Fe_2N@GNS as anode, TiN@GNS as cathode in a quasi-solid-state electrolyte of LiCl-PVA. (Reference A[181], B[182] and C[183])

Regarding the full device performance comparison, energy density and power density are of key importance. As was listed in table 3.1.2 and plotted in the Ragone plot (Figure 3.1.8a), we compared our ASC full device with other devices based on PVA electrolyte. The inset figure in Figure 3.1.8 shows two devices in tandem that light up 10 white (working voltage: ~ 3.1 V) and 11 pink LEDs (working voltage: ~ 1.9 V) connected in parallel. At current density of 2, 4, 8, 16 A g^{-1}, the volumetric energy density and power density (calculated based on Figure 3.1.7b) are 0.61, 0.55, 0.51, 0.37 mWh cm^{-3} and 52.9, 105.7, 211.4, 422.7 mW cm^{-3}, respectively. Though our nitride-based ASC delivers lower energy density than that of PANI//WO_x-MO_x ASC[184] due to the intrinsic high capacitance of the latter material, the values of both energy density

and power density are higher than other solid state PVA-based devices. A series of devices were measured together and their cyclability data in 20,000 cycles were plotted in Figure 3.1.8b to test the repeatability of the experimental methodology. As can be seen, within 20,000 cycles, all the devices show very stable and similar specific capacitance ~ 58 F g^{-1} and high capacity retentions (varying from 96.8 to 99.8%). The results demonstrate the high repeatability and reliability of the fabrication method. The device illustration and real photo are presented in Figure 3.1.8c and d for clearer understanding of the full device.

Table 3.1.2 Comparisons of PVA-based solid state asymmetric supercapacitors.

Device (Cathode||Anode)	Rate performance	Cycling performance	Energy density	Power density	Electrolyte	Ref.
β-$Ni(OH)_2$||activated carbon	71.7 % gravimetric capacitance retention from 2 to 10 mA	76 % capacitance retention after 2000 cycles @ 5 mA	9.8 Wh kg^{-1}	154 W kg^{-1}	KOH-PVA	[185]
$NiOOH/Ni_3S_2$||Fe_3O_4	71.7 % gravimetric capacitance retention from 5 to 50 mV s^{-1}	27 % capacitance retention after 2000 cycles @ 1 A g^{-1}	82.5 Wh kg^{-1}	930 W kg^{-1}	KOH-PVA	[186]
CNT||CNT/WO_3		93.2 % capacitance retention after 10000 cycles @ 1 mA cm^{-2}	0.59 mWh cm^{-3}	30.6 mW cm^{-3}	H_2SO_4-PVA	[187]
α-MnO_2||Fe_2O_3	58.6% of volumetric capacitance retention from 2 to 10 mA cm^{-2}	84% capacitance retention after 5000 cycles @ 2 mA cm^{-2}	0.32 mWh cm^{-3}	139.1 mW cm^{-3}	LiCl-PVA	[188]
H-TiO_2@MnO_2||H-TiO_2@C	56 % volumetric capacitance retention from 10 to 400 mV s^{-1}	91.2% capacitance retention after 5000 cycles @ 100 mV s^{-1}	0.30 mWh cm^{-3}	230 mW cm^{-3}	LiCl-PVA	[181]
WO_{3-x}/MoO_{3-x}||polyaniline	63.6% of areal capacitance retention from 2 to 20 mA cm^{-2}	75% capacitance retention after 5000 cycles @ 5 mA cm^{-2}	1.1 mWh cm^{-3}	730 mW cm^{-3}	H_3PO_4-PVA	[184]
VO_x||VN	74.7% capacitance retention from 0.5 to 5 mA cm^{-2}	87.5% capacitance retention after 10000 cycles @ 100 mV s^{-1}	0.61 mWh cm^{-3}	850 mW cm^{-3}	LiCl-PVA	[183]
Co_9S_8|| Co_3O_4@RuO_2	35.3 % volumetric capacitance retention from 2.5 to 50 mA cm^{-2}	90.2 % capacitance retention after 2000 cycles @ 10 A g^{-1}	1.44 mWh cm^{-3}	890 mW cm^{-3}	KOH-PVA	[189]
This work	**98% capacitance retention from 10 to 100 mV s^{-1}**	**98% capacitance retention after 20000 cycles @ 4 A g^{-1}**	**0.51 mWh cm^{-3}**	**211.4 mW cm^{-3}**	**LiCl-PVA**	

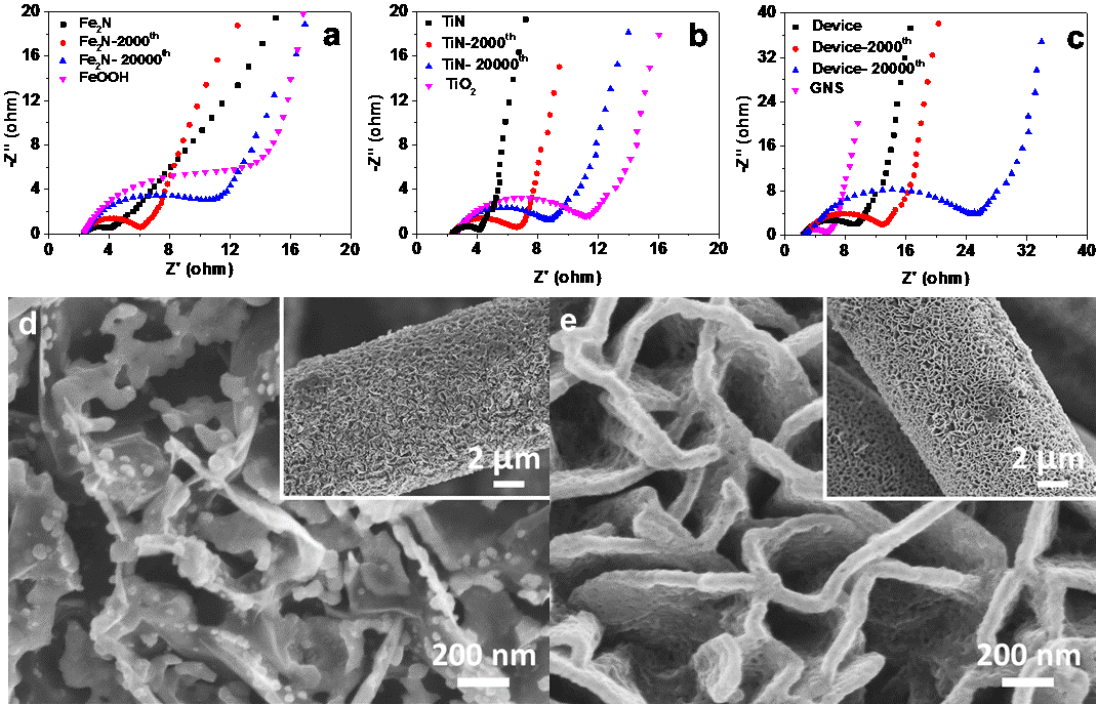

Figure 3.1.9 Electrochemical impedance tests and electrode structural stability study. Nyquist plots of a) anode and b) cathode (tested in a standard three-electrode system) and c) full device (An AC voltage with 5 mV amplitude in a varied frequency from 50 mHz to 100 kHz). SEM images of d) anode and e) cathode materials (insets are the SEM images at low magnification).

As can be concluded from Figure 3.1.5 and 3.1.7, the Fe_2N anode, TiN cathode and ASC full device exhibit rectangle-shaped CV curves and triangle-shaped charge-discharge curves; this should be ascribed to the high conductivity of the electrode materials both in aqueous and gel electrolyte. To confirm this, electrochemical impedance of single electrodes and the full device at different cycling stages were tested and plotted in Nyquist plots (Figure 3.1.9a-c). Both the single electrode and full device are with small electrochemical impedance values (less than 5 Ω). After cyclings (2000 and 20000 times), the impedance values of both single electrodes and the full device increase slightly and are still acceptably low. Compared with their oxyhydroxide/oxide source materials, the nitride electrodes exhibit smaller impedance, demonstrating the successful material design. The high performance (high capacity retention: ~ 98% in 20000 cycles; and rate capability: ~ 99 % capacity maintenance when rate increases

from 10 to 100 mV s^{-1}) of the full device can be ascribed to the structure stability of the electrode material. To figure out the reasons, the morphology of the ASCs anode and cathode after 20, 000 cycles were checked with SEM (Figure 3.1.9d and e). It is found that the entire electrode structure is well maintained (see insets in Figure 3.1.9d and e). Meanwhile, the fine structure of Fe_2N anode (nanoparticle morphology) and TiN cathode (porous structure) are well kept although slight aggregation of Fe_2N is observed. This verified the estimation that both electrode materials are with high structure stability.

3.1.4 Reaction mechanisms prediction and analysis

Regarding the Faradic reaction mechanisms of metal nitrides in aqueous solutions, Lu[182] proposed the possible reaction mechanism for VN in their previous work. Inspired by their proposal, we propose the Faradic reaction mechanisms for Fe_2N and TiN as follows:

$$Fe_{\frac{3x+2y}{2}}N_xO_y + zLi^+ + ze^- \leftrightarrow Fe_{\frac{3x+2y-z}{3}}N_xO_yLi_z \quad ; \quad Ti_{\frac{3x+2y}{2}}N_xO_y + zLi^+ + ze^- \leftrightarrow Ti_{\frac{3x+2y-z}{4}}N_xO_yLi_z$$

We suspect that the changes of valence states of Fe and Ti(Fe: +2 to +3; Ti: +2 to +4) should be responsible for the pseudo-capacitance in metal nitrides. In addition, previous work reported the possible oxidation reaction of TiN with H_2O and O_2 ($TiN + 2H_2O \rightarrow TiO_2 + \frac{1}{2}N_2 + 4H^+ + 4e^-$, $2TiN + 2O_2 \rightarrow 2TiO_2 + N_2$) in the aqueous electrolyte and indicated that using PVA based gel electrolyte would alleviate the oxidation problem because of the reducing of water content in the electrolyte.[182] In our suspect, we consider both contributions from these two aspects. To track the materials shifts on both electrodes, we characterized the pristine electrode material and the cathode and anode (from the full device) after 2000 and 20000 cycles with detailed XPS and Raman characterization. The typical peaks of Fe_2N[148] (centered at 170, 300, 420 and 600 cm^{-1}) were weaken with the cycles while those of Fe_2O_3 (220, 290, 490 and 593 cm^{-1})[190] become dominant (Figure 3.1.10a and b). Regarding the cathode, similar phenomenon was observed. The Raman spectra from 100 to 3000 cm^{-1} (Figure 3.1.10c) for TiN@GNS shows the typical peaks of 200 and 558 cm^{-1} caused by the first-order transverse acoustic and transverse optical modes of TiN.[166, 191] In a narrow

wavelength range (Figure 3.1.10d) of 100–1000 cm^{-1}, the fade of TiN peaks from the pristine sample to the one after 20000 cycles can be clearly observed. Meanwhile, peaks centered at 147, 465 and 610 cm^{-1} which belongs to TiO_2 raised obviously with the cycling.[182] This indicates that TiO_2 forms during the cyclings. To have more solid proofs of materials changes, XPS characterization was introduced to test the electrodes at different cycling situations. For anode, the weaken of N 1s signal in Figure 3.1.11b and elevating of O 1s (Figure 3.1.11c) demonstrated the transfer from Fe–N to Fe–O–N. Moreover, Figure 3.1.11d-f exhibited the binding energy changes and intensity shifts of Ti 2p, N 1s and O 1s at different cycles. It is noted that the binding energy of Ti–O (458.3 eV) shifts to higher value (459 eV)[166, 192, 193] indicating the charging state become stronger with longer cycles. While the intensity ratio of Ti–O to Ti–N become bigger which demonstrates that the ratio of Ti at +4 valence state becomes dominant. In addition, the intensity decrease of N 1s (Figure 3.1.11e) and increase of O 1s (Figure 3.1.11f) further verified the valence state increase of Ti. Therefore, we suspect that both valence states of Ti and Fe have increased during cycling which should be the source of pseudo-capacitance.

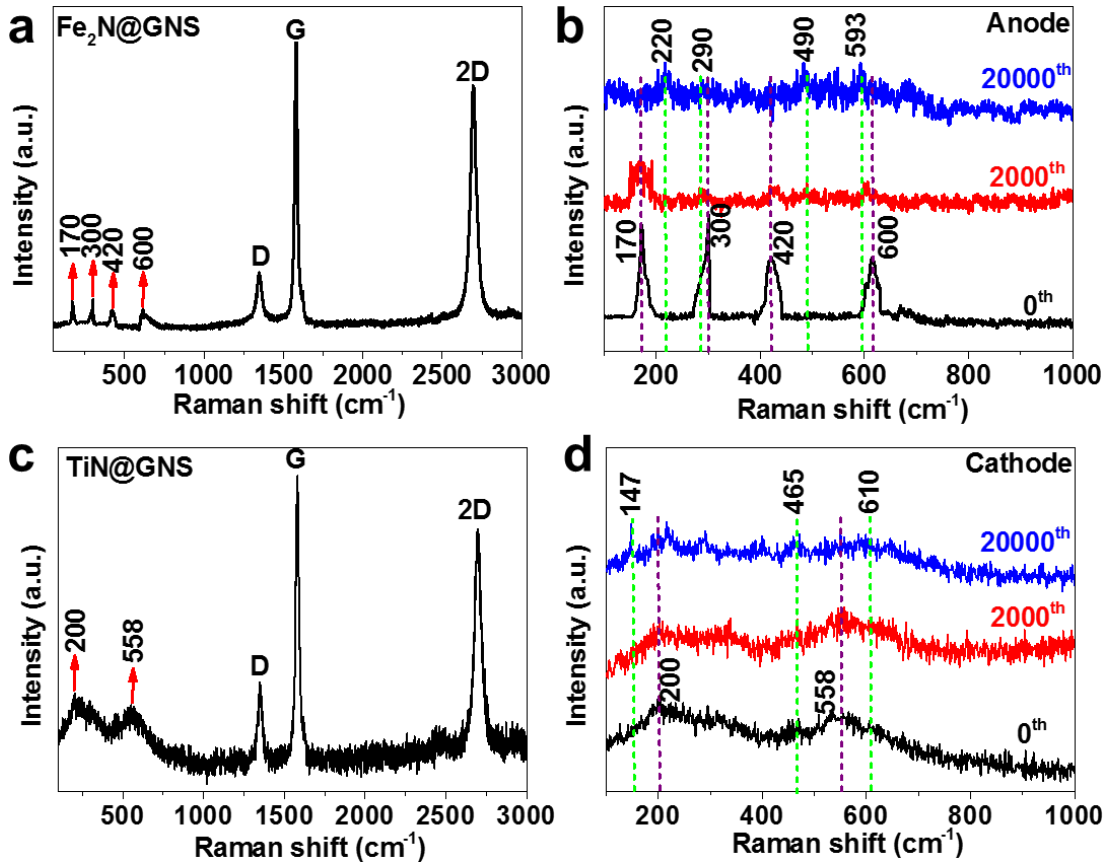

Figure 3.1.10 Raman characterization of electrode materials at different cycles. Raman spectra of Fe_2N@GNS anode from a) 100 to 3000 cm^{-1} and b) 100 to 1000 cm^{-1} at different cycles (0^{th}, 2000^{th} and 20000^{th}); Raman spectra of TiN@GNS cathode from a) 100 to 3000 cm^{-1} and b) 100 to 1000 cm^{-1} at different cycles (0^{th}, 2000^{th} and 20000^{th}).

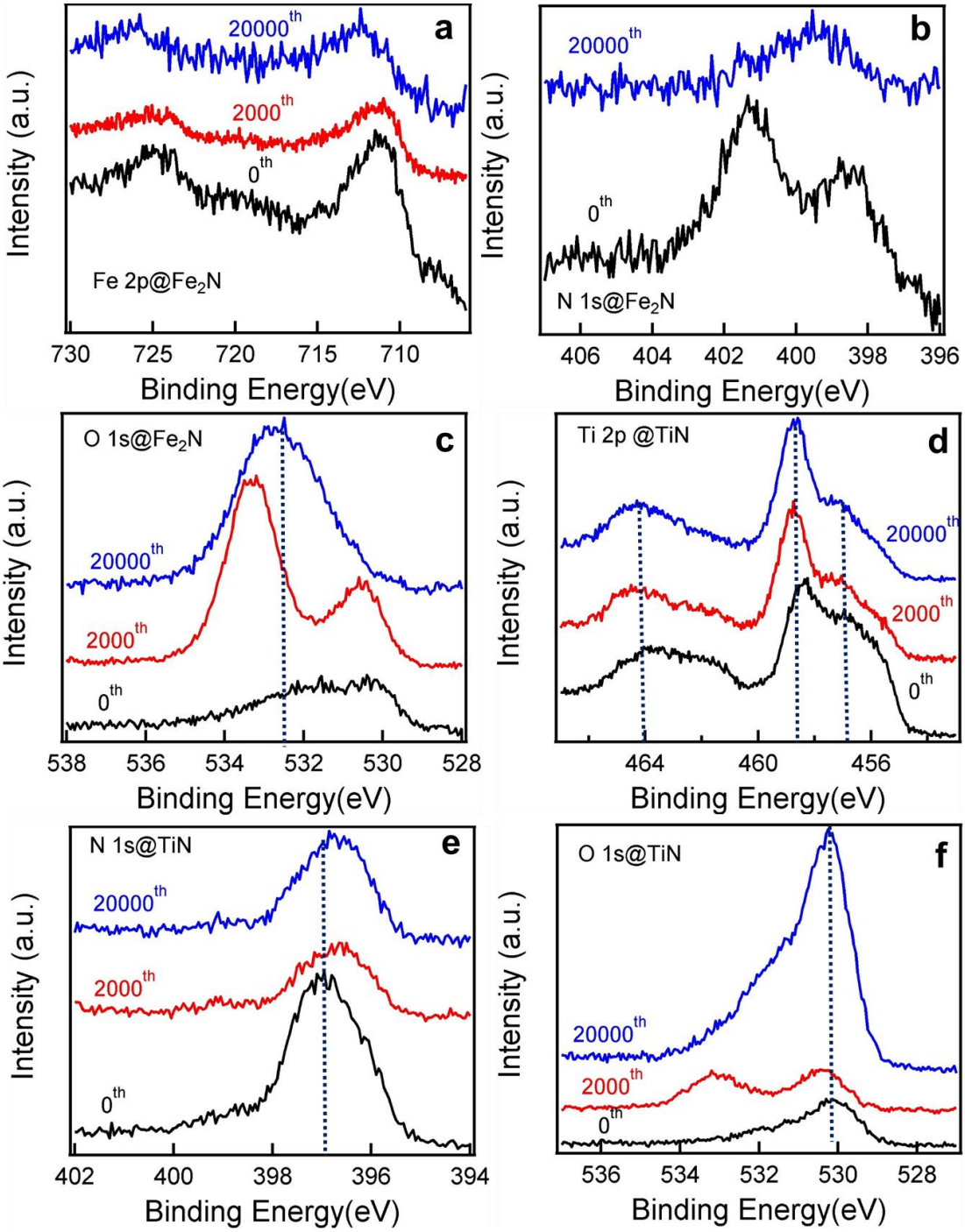

Figure 3.1.11 XPS characterization of electrode materials at different cycles. XPS spectra of a) Fe 2p, b) N 1s and c) O 1s signal changes of Fe_2N@GNS anode and d) Ti 2p, e) N 1s and f) O 1s signal changes of TiN@GNS cathode at different cycles (0^{th}, 2000^{th} and 20000^{th}).

3.1.5 Conclusion

As can be concluded here, we successfully fabricated metal nitride-based, quasi-solid-state asymmetric supercapacitors device with Fe_2N anode, TiN cathode and PVA/LiCl neutral gel electrolyte. The uniform coverage of Fe_2N nanoparticles and porous structure of TiN on the highly conductive GNS substrates are important merits that resulting in the outstanding stable cycles (~ 98% capacity retention within 20000 cycles) and high rate capability (~ 99 % capacity maintenance from 10 to 100 mV s^{-1}) of the devices. The high repeatability is verified with five devices cycling tests which shows nearly overlapping cycling curves. Typical high values of power density ~ 6.4 kW kg^{-1} (211.4 mW cm^{-3}) and energy density ~ 15.4 Wh kg^{-1} (~ 0.51 mWh cm^{-3}) and are obtained. To demonstrate the real application, two devices in series are connected and are able to power 21 pink and white LEDs. The methodology of combining ALD and ammonia annealing can be extended to fabricate other metal nitrides or metal nitrides core-shell structure for electrochemical energy storage applications.

3.2 $Fe_2N@Ti_2N$ core-shell nanoarrays for symmetric supercapacitors

3.2.1 Introduction

Though with high power density and ultra-long cycles, the low energy density remains to be the obstacle for supercapacitor applications.[194-196] Regarding supercapacitor energy density, it can be expressed in $E = 0.5\ CU^2$, where C is the capacitance while U is the working potential of a supercapacitor,[197, 198]. Therefore, efforts have been input to increase the supercapacitor energy density in mainly two aspects: First is to increase the overall capacitance by searching for high-capacitance electrode materials and do structural optimization with nano fabrication technic.[199] Second is to widen the working potential of the supercapacitor device. Previously, researchers have explored kinds of organic electrolytes because of their promising higher working potential (~ 2.7 V) compared with water-based electrolytes which are always less than 1 V limited by water decomposition reactions.[197-201] However, organic electrolytes usually suffer from lower ion/electron mobility which will lead to big electrochemical impedance thus cause bad rate performance. Worse still, organic electrolytes are toxic and high cost which obeys our research idea of finding better green energy resources.[202, 203] Hence, recently, research efforts have been shifted more to aqueous electrolyte based supercapacitors by enlarging the working potential of supercapacitor device.[204-209] Fortunately, with efforts input, high working voltages like 1.6 and 1.8 V have been realized on state-of-art materials RuO_2[209] and Ru,[210] respectively. But still, problem of the high cost is remained. Researcher have figured out ways for working voltage determination based on ionic electrolyte system,[211, 212] but regarding the aqueous-based electrolytes, water decomposition problem should be considered as the key factor to determine the stable working voltage of the supercapacitor devices. Thus, materials that have high oxygen and hydrogen over-potential and therefore can stand high voltage water decomposition are suitable to

be capacitive electrode material candidates. Previous work reported the carbon based materials as supercapacitors which are proven to have high working voltage up to 2 V but the capacitance is not very high.[197, 198, 213] Whereas, the research experience that with heteroatoms (nitrogen) doping, the carbon materials can have much increased electrode material over-potential against both oxygen and hydrogen can be grafted to other similar research.[199, 200]

Also, it is proved in these literatures that higher nitrogen doping level in oxides can lead to higher capacitance due to the fact that doping can generate defects and these defects will facilitate electron donor properties of the electrode composites.[214-217] Inspired the results, we consider to have a full substitution with nitrogen to the oxygen by high temperature ammonia annealing to convert the metal oxides/oxyhydroxides source materials to their nitride counterparts. Besides, metal nitrides are proven to be good supercapacitor electrode ascribe to their high electron conductivity (4000–55500 S cm^{-1})[143, 144, 218] and ultra-stability in water-based electrolytes.[219] To follow our previous work, we continue to use Fe_2N as study object because it has high specific capacitance ~ 160 F g^{-1} in 1 M LiCl electrolyte.[13] In previous studies, the Fe_2N transferred from FeOOH or Fe_2O_3 are always in the form of aggregated particles whatever the morphology of the precursors.[147, 148, 179] According to the discussion in chapter 1, the two dimensional nanorod structure is more favored due to the direct ion/charge transport paths which will lead to high rate performance and capacitance .[220]

Thus, in this chapter, we are going to discuss how to achieve high-voltage supercapacitors with the Fe_2N nanorod electrode as example. The electrode active material of the Fe_2N@Ti_2N (FTN) core@shell nanorods are realized through a shape-preserved process and applied as both electrodes in a symmetric supercapacitor device system. With 1 M LiCl-PVA as electrolyte, the quasi-solid state capacitive device exhibits a high stable working voltage of 2.0 V. Also, the device shows comparably high capacitance (~ 86 F g^{-1}) at a high current density of 2.7 A g^{-1} in long-terms cycling.

3.2.2 Experimental details

Materials Synthesis

Substrate pretreatment: Carbon cloth (thickness: ~ 0.1 mm; carbon fiber diameter: ~ 10 μm) was utilized as substrate in this work. Due to the hydrophobic property, carbon cloth substrates were pretreated with oxygen plasma for 10 minutes (plasma power: 200 W; pressure: 70 mTorr; O_2 gas flow: 100 sccm.) to clean the substrates as well as make the substrates surface hydrophilic.

Source material growth: The FeOOH core source material was synthesized through a hydrothermal process. First, the pretreated carbon substrates are pasted to a glass plate holder (2.2×4.3 cm^2). Second, 0.24 g Na_2SO_4 and 0.4 g $FeCl_3 \cdot 6H_2O$ were resolved in 35 ml distilled water under magnetic stir for 10 mins as reaction solution. The solution was transferred to the autoclave and put under 120 °C for 6 h. The as synthesized FeOOH is of nanorod morphology as was verified by SEM.

Fabrication of Fe_2N@Ti_2N (FTN) core@shell electrodes: The hydrothermal synthesized FeOOH nanoarray was rinsed with DI water for 10 mins and dried under 80 ºC for 12h. Then the shell source material TiO_2 (20 nm) was coated through atomic layer deposition (ALD) method. Finally, the sample of FeOOH@TiO_2 was annealed in pure ammonia atmosphere for 1 h at 800 °C under a gas flow of 50 sccm. The heating rate is 20 °C per minute and cooling is with the oven.

Fabrication of control samples: Ti_2N control samples were prepared by first deposition of 20 nm TiO_2 source material on the pretreated carbon cloth. The, bare carbon cloth, FeOOH@carbon cloth, and TiO_2@carbon cloth were annealed in NH_3 atmosphere under the same condition as the core-shell electrode as comparison with the FTN.

Structural and Morphology Examination

The structural information of the electrode active material was identified with X-ray diffraction (XRD) (RigakuD/Max-2550 with Cu Kα radiation) and X-ray photoelectron spectroscopy in a VG ESCALAB 220i-XL system with monochromatic Al Ka1 as source (1486.6 eV). The morphology information of all the samples was

characterized by scanning electron microscopy (SEM) (JEOL 2100) at 5 kV, and transmission electron microscopy (TEM) (JEOL JEM-2010F) at 200 kV.

Electrochemical Performance Test of Device and electrode

Single electrode properties study was conducted in a standard three-electrode testing system with core@shell nanoarray, Fe_2N particle and Ti_2N thin film and carbon cloth-N as working electrode, Ag/AgCl as reference electrode and Pt as counter electrode in 1 M LiCl electrolyte. Full devices were assembled with the as synthesized core@shell nanoarray as electrode, direct-purchased NKK membrane as separator and 1 M LiCl-PVA as the gel electrolyte (The LiCl-PVA gel electrolyte ware prepared by resolving 6 g PVA and 12.6 g LiCl in 100 ml DI water and stirring under 85 ^{o}C oil bath for 2 h).

Active Material Mass Loading Determination

The substrates were weighed after oxygen plasma treatment. After the growth of FTN arrays, we weigh the sample again and subtract the mass of the bare substrate. After calculation, the active material mass loading is about 1 mg cm^{-2}.

3.2.3 Results and Discussion

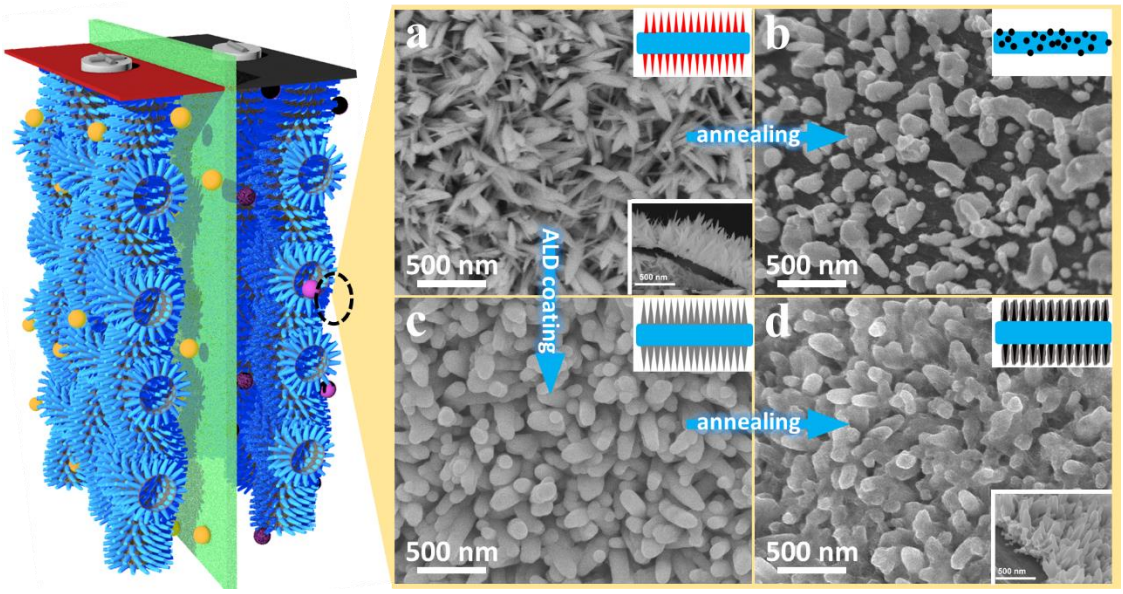

Figure 3.2.1 Illustration and morphology of the growth process of electrode material. SEM of a) source material FeOOH, b) sample after annealing a) in ammonia under 800 ºC for 1h.

Figure 3.2.1 shows the entire growth process of the FTN and control sample of Fe_2N nanoparticles. The FeOOH nanorods acting as source material of the core were synthesized through a hydrothermal reaction process as was reported;[221] As can be seen in Figure 3.2.1a, the as synthesized FeOOH nanorods are homogeneously distributed on the substrate with length ~500 nm (Figure 3.2.1a inset) and diameter ~50 nm. After annealing directly in ammonia, these as obtained FeOOH nanorods turn into particles aggregated on the carbon fiber (Figure 3.2.1b) with some areas of the carbon fiber surface even exposed indicating the collapse and drop off of the active material from the substrate. Fortunately, with 20 nm ALD TiO_2 coating (Figure 3.2.1c), the nanorod structure is successfully inherited after the high temperature ammonia annealing (Figure 3.2.1d). The final Fe_2N-Ti_2N core-shell nanorods (FTN) are with length ~ 500 nm as clearly showed in Figure 3.2.1d inset.

Detailed structural characterization was conducted to confirm the FTN composition after transformation of FeOOH@TiO_2 source material. The FTN core-shell structure can be easily seen in Figure 3.2.2a and d (FTN nanoarrays are with

diameter ~ 80 nm, length ~ 500 nm and the shell layer thickness ~ 15 nm). The lattices of Ti_2N (111) (d-spacing 2.30 Å), (212) (d-spacing 1.45 Å), and (301) (d-spacing 1.47 Å) are detected in the near-edge area (Figure 3.2.2b). And the lattice fringes in the middle areas (Figure 3.2.2c) correspond well to Fe_2N (121) (d-spacing 2.11 Å) and (221) (d-spacing 1.63 Å). All these information pointed out the face-centered-cubic structure of Fe_2N and Ti_2N and are well in accordance with the X-ray diffraction (XRD) patterns (Figure 3.2.3a) showing the typical fcc structure of Fe_2N core and Ti_2N shell according to JCPDS card 50-0958 and JCPDS 17-0386, respectively. Meanwhile, The X-ray photoelectron spectroscopy (XPS) results of FTN further verified the structure (Fe 2p peak located at 711.4eV is the Fe-N bonding; Ti 2p located at 457.0eV is due to the N-Ti-O bonding while the strong peak settled at 458.9eV should be the Ti-N bond, indicating the majority composition of Ti_2N; In N 1s spectra, the peak is mainly located at 396.9Ev. This is consistent with Fe-N and Ti-N bonding and the negligible peak located at 398.5eV is due to N-Me-O (N-Fe-O or N-Ti-O) bonding. The slight observed N-Me-O peaks should be due to the small amount oxidation of FTN resulting from the sample left in air for long time; O 1s peak at 530.5eV should be due to H_2O while the neglectable peak located at 532.2eV is due to metal oxides). In addition, the homogeneous element distribution profiles of Fe, Ti and N are also in accordance with the profile in Figure 3.2.2e, demonstrating the successful transformation of FeOOH@TiO_2 source to the final FTN nanoarrays with a good structure inherited.

Previous work reported that N doping can obviously increase the capacitance of a carbon-based electrode.[222-225] To subtract the capacitance contributed by the bare carbon cloth and have a clear view of the single core/shell material capacitance, the cyclic voltammetry (CV) curves of the bare carbon cloth annealed in ammonia (as called carbon cloth-N), Ti_2N thin film, Fe_2N nanoparticle, and FTN nanoarrays are plotted together in Figure 3.2.3f. Calculated based on the CV curve area, the capacitance contribution from the carbon cloth-N to the whole electrode is ~ 0.05 % thus can be neglected. Moreover, both the CV curves areas of Ti_2N thin film and bare Fe_2N nanoparticles are comparably small compared with that of FTN electrode,

indicating the benefits of core-shell nanorod structure.

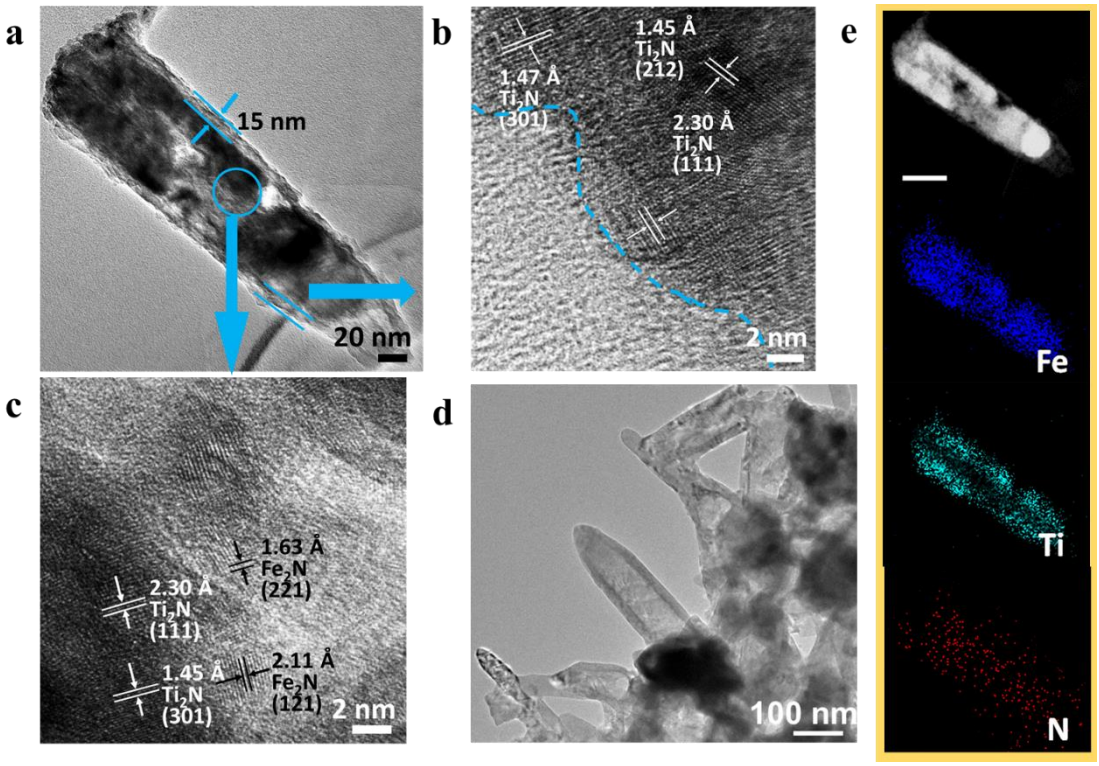

Figure 3.2.2 Detailed structure characterization of the FTN electrode. a) TEM image of FTN, b) and c) HRTEM images shown the lattice fringes of the related area pointed out by the blue arrows in a), d) TEM image of FTN under low magnification. e) TEM element mapping of FTN nanorod arrays in a) shown the profile of Fe, Ti and N distribution.

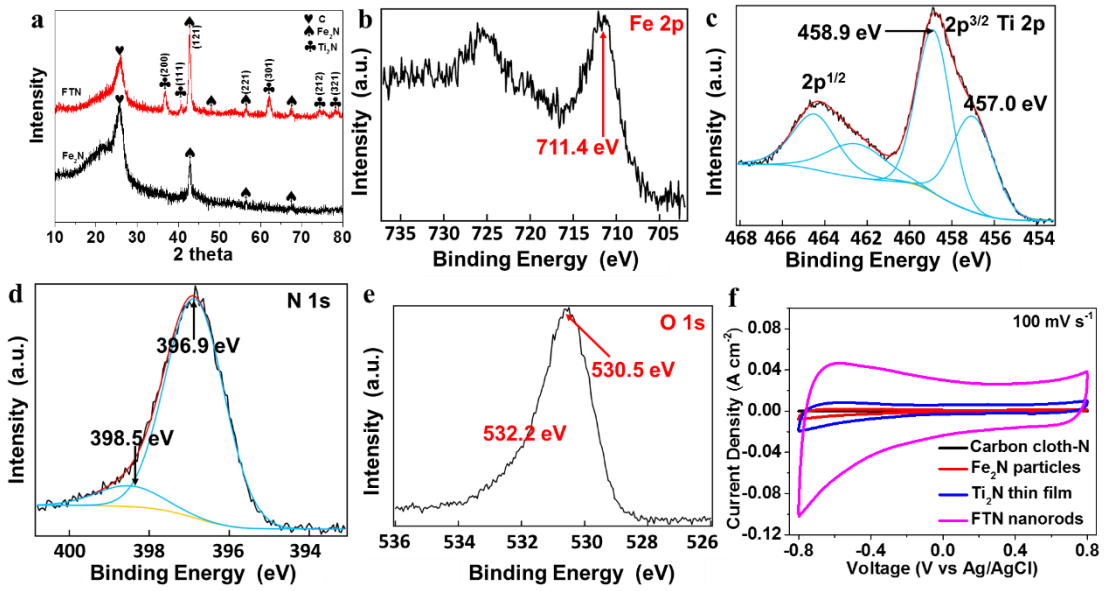

Figure 3.2.3 Crystal structure and charge state study. a) XRD pattern of Fe_2N nanoparticle and the FTN nanoarrays shown the related face centered cubic phase of Fe_2N core and Ti_2N shell, XPS spectra of b) FTN core-shell nanorods, c) Ti 2p, d) N 1s and e) O 1s peak. f) Cyclic voltammetry curves of FTN nanorods compared with control samples of Ti_2N thin film, Fe_2N particles and carbon cloth-N at scan speed of 100 mV s^{-1}.

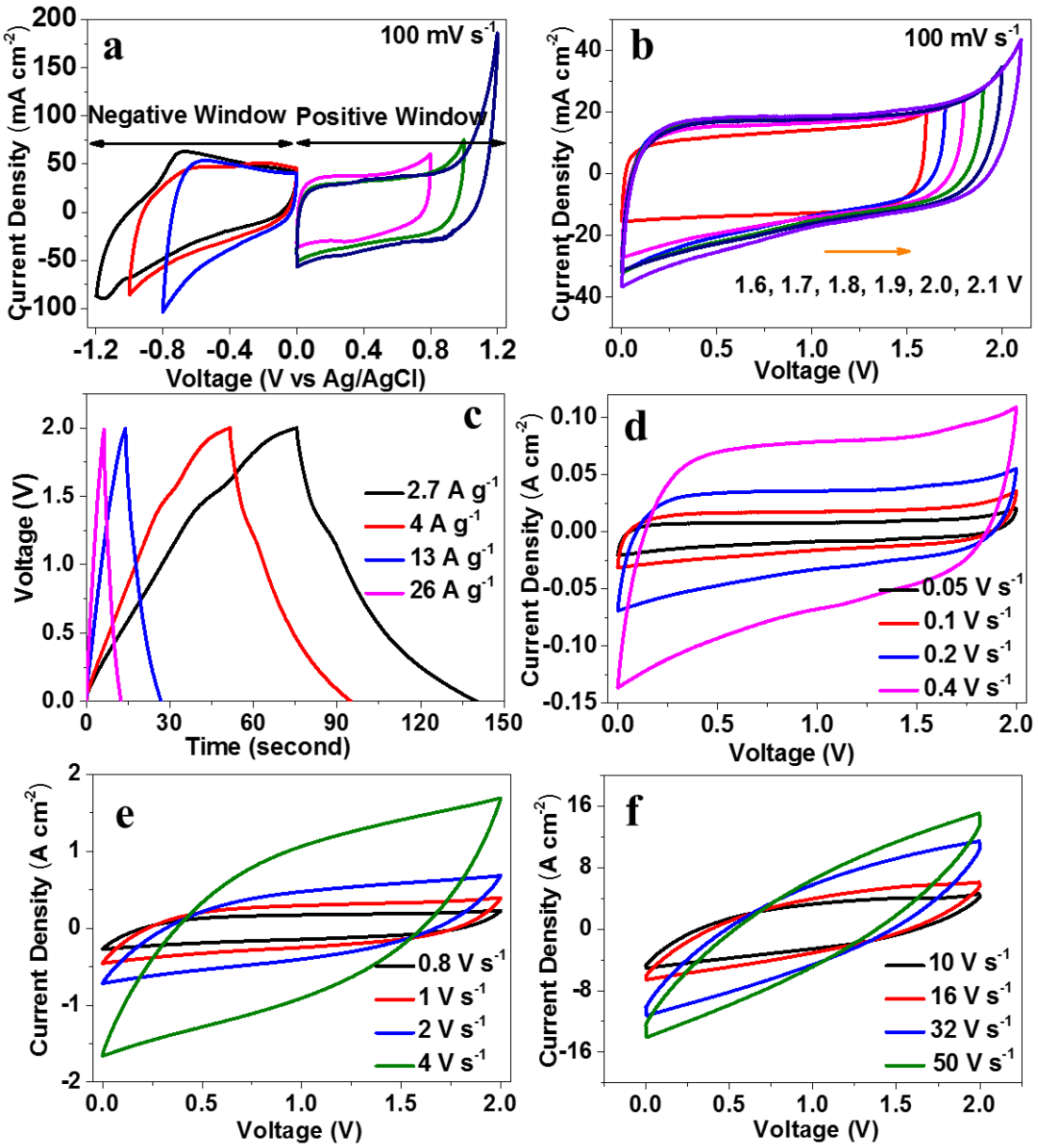

Figure 3.2.4 Electrochemical performance of the solid-state symmetric supercapacitor device. CV curves of a) single electrode at different negative and positive voltage range and b) device from varied voltage range 0 to 1.6-2.1 V working potential, c) charge-discharge curves, and d-f) CV curves of the device at different scans speed from 50 mV s^{-1} to 50 V s^{-1}.

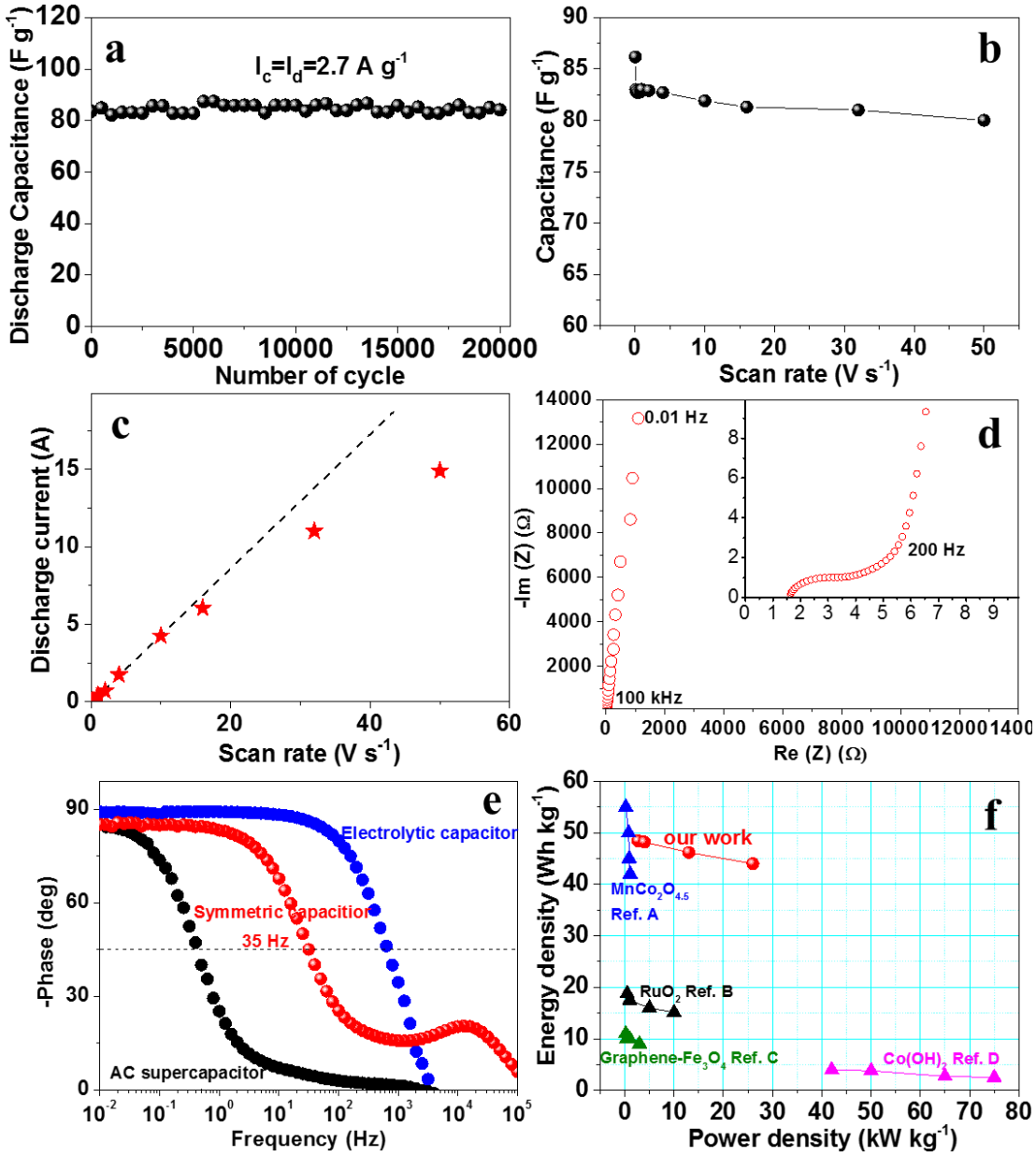

Figure 3.2.5 a) Cycling and b) Rate performance of the full device, c) Evolution of the discharge current against scan speed, d) Electrochemical impedance spectra of the full device with the inset magnified figure shown the impedance at high frequency range, e) Phase angle versus frequency curves comparison of the full device, commercial electrolytic capacitor and the AC supercapacitor,[219] and f) Ragone plot of quasi-solid state symmetric supercapacitor device compared with other reported symmetric devices with working voltage over 1 V. (Reference A[204], B[207, 209], C[207] and D[205])

All the electrochemical test of single electrode was conducted in a standard three-electrode testing system with the FTN electrode as working electrode, Ag/AgCl and Pt plate as reference and counter electrode, respectively. In order to figure out the maximum working voltage of the full device, FTN single electrodes was scanned at different working windows versus Ag/AgCl reference electrode (negative range: −1.2 ~ −0.8 to 0 V; positive range: 0 to 0.8 ~ 1.2 V) (Figure 3.2.4a). In 1 M LiCl electrolyte, the CV curves of the FTN electrode are quasi-rectangle shape at voltage range up to wide working windows (−1 ~ 0 V for negative range; 0 ~ 1 V for positive range). However, current leaps appear with the expands of working voltage at ±1.2 V. These current leaps indicate the water decomposition (current leap at negative potential area should be caused by the hydrogen evolution reaction;[209, 210] current leap at positive area should be caused by the oxygen evolution reaction[209, 210]) at these voltages.

Following the single electrode voltage range research, full device working window exploring was conducted with the FTN nanorods as both cathode and anode and LiCl-PVA as quasi-solid electrolyte. The full device was tested at working window from 0 to 2.1 V (Figure 3.2.4b). Within 2.0 V, CV curves are mostly in a standard rectangle shape which indicates a major capacitive behavior. However, beyond 2.0 the current leaps appeared due to the gas evolution reaction (water decomposition, H_2 and O_2 released).[203] Meanwhile, slight plateaus (~ 1.5 V Figure 3.2.4c) are observed at low charge-discharge current density of 2.7 and 4 A g^{-1} which should result from the redox reactions ($Ti_{\frac{3x+2y}{2}}N_xO_y + zLi^+ + ze^- \leftrightarrow Ti_{\frac{3x+2y-z}{4}}N_xO_yLi_z$; $Fe_{\frac{3x+2y}{2}}N_xO_y + zLi^+ + ze^- \leftrightarrow Fe_{\frac{3x+2y-z}{3}}N_xO_yLi_z$).[13]

The device was scanned at a voltage range of 0 ~ 2.0 V with different scan rate from 50 mV s^{-1} to 50 V s^{-1}. Beneath 400 mV s^{-1}, the CV curves are in standard rectangle shape indicating the good capacitive behavior (Figure 3.2.4d). Moreover, the device exhibit excellent reaction towards high scan speed from 0.8 to 50 V s^{-1} (Figure 3.2.4e and f).

The cycling performance of the full device was tested with current density of 2.7 A g^{-1}. Within 20000 cycles, the full device delivers a stable capacitance ~ 86 F g^{-1} and a high capacitance retention up to 99 % (Figure 3.2.5a). The calculated capacitance based on Figure 3.2.4 d-f shows a sharp drop from 50 to 100 mV s^{-1}. But after 100 mV

s^{-1}, scarcely capacitance drop can be observed even as high as 50 V s^{-1} (Figure 3.2.5b). The curve of evolution of the discharge current against scan speed is plotted in Figure 3.2.5c. It is easily to notice that the linear dependence of discharge current on the sweep speed goes up to 16 V s^{-1} (Figure 3.2.5c).

To figure out the reasons for the high-rate properties of the FTN nanoarrays electrode, the electrochemical impedance spectroscopy (EIS) measurement was introduced. As can be seen from the Nyquist plot (Figure 3.2.5d), the full device exhibits a closed 90° slope that begins at 200 Hz demonstrating the capacitive behavior at high frequencies caused by the highly conductive surface of the core-shell electrode. From the equivalent series resistance plot, we can see that the intercept of the curve with the real axis is only 1.6 Ω. In addition, the charge transfer resistance is only 2.0 Ω. These small values of electrochemical impedance manifest the low internal resistance and good electric conductivity of the full device. Moreover, at the phase angle of −45°, the characteristic frequency f_0 is 35 Hz (Figure 3.2.5e). Though the characteristic frequency of the device is slightly lower compared with the commercial supercapacitors, it is much higher than that of the electrolytic capacitors. These results explain the fast charge/discharge capability and the high power properties. The excellent performance of the full device verifies itself to be applicable in electric hybrid vehicles which require rapid instantaneous delivering of the stored energy and harvesting of the wasted mechanical energy.

To have a full understanding of the device performance, the energy density against power density was plotted in the Ragone plot comparing with other symmetric devices. As can be seen clearly from the Figure 3.2.5f, both the energy density and power density of the full device can be considered high among other devices. To figure out the real status of our research, we listed full comparison of the long-term cyclability, working voltage, power density, and energy density and in Table 3.2.1. It can be seen that though the specific capacitance of our device is at the same level with other devices, benifitted by the highest working voltage, the energy density of our device stands out to be the highest value.

Table 3.2.1 Comparison of aqueous electrolyte-based symmetric supercapacitors with working voltage > 1.0 V

Material	Working voltage (V)	Device capacitance	Capacitance Retention	Power density (kW kg^{-1})	Energy density (W h kg^{-1})	Ref.
Nanocrystalline hydrous RuO_2	1.6	52.66 F g^{-1} @ 2.5 A g^{-1}	92 % after 2000 cycles @ 2.5 A g^{-1}	10	15.1	[209]
Nanocrystalline Ru thin film	1.8	68 mF cm^{-2} @ 1 mA cm^{-2}	99 % after 2000 cycles @ 1 mA cm^{-2}			[210]
$MnCo_2O_{4.5}$ nanoneedle/carbon hybrid	1.5	235 F g^{-1} @ 2 A g^{-1}	86 % after 5000 cycles @ 2 A g^{-1}	2	40	[204]
$Co(OH)_2$ thin film	1.2	44 F g^{-1} @ 5 mV s^{-1}		42	3.96	[205]
MnO_2 nanowire	1.2	394 F g^{-1} @ 0.5 A g^{-1}	95 % after 2000 cycles @ 0.5 A g^{-1}	0.3	2.9	[206]
graphene/magnetite composite	1.0	72 F g^{-1} @ 3.57 A g^{-1}	99 % after 100000 cycles @ 0.5 A g^{-1}	3	9	[207]
$ZnCo_2O_4$/carbon nanofoam composite	1.2	77 F g^{-1} @ 5 mV s^{-1}	99 % after 100000 cycles @ 5 mV s^{-1}	1.2		[208]
N-rich carbon	1.5	710 F g^{-1} @ 20 A g^{-1}	99 % after 10000 cycles @ 20 A g^{-1}	1.5	75	[226]
FTN in this work	**2.0**	**87.21 F g^{-1} @ 2.7 A g^{-1}**	**99 % after 20000 cycles @ 2.7 A g^{-1}**	**2.7**	**48.45**	

3.2.4 Reaction mechanisms prediction and analysis

The high working voltage is the intrinsic reason for the high energy density that makes this work outstanding. Though we cannot give a very certain answer to this working potential enlargement mechanism and there is no previous study showing the precise explanation. But we do design our experiments with the inspiration from some literature which, though, did not directly indicate the working potential enlargement. Our original design is mainly based on the following considerations: First, nitrogen doping is proven to increase the working potential of supercapacitor devices based on carbon related materials. The reason has been given that the N is a good heteroatom to carbon because it helps to increase the surface defects during the N-doping process. We hope this can be grafted to our material; Second, as was proposed by previous work,[13, 182, 183] metal nitride is easy to react with water and ions in the LiCl electrolyte ($TiN + 2H_2O \rightarrow TiO_2 + \frac{1}{2}N_2 + 4H^+ + 4e^-$, $2TiN + 2O_2 \rightarrow 2TiO_2 + N_2$, $Ti_{\frac{3x+2y}{2}}N_xO_y + zLi^+ + ze^- \leftrightarrow Ti_{\frac{3x+2y-z}{4}}N_xO_yLi_z$, $Fe_{\frac{3x+2y}{2}}N_xO_y + zLi^+ + ze^- \leftrightarrow Fe_{\frac{3x+2y-z}{3}}N_xO_yLi_z$, $V_{x+\frac{2y}{3}}N_xO_y + zM^+ + ze^- \rightarrow V_{x+\frac{(2y-z)}{3}}N_xO_yM_z{}^{z+}$ (M^+=Li$^+$, H^+)). These reactions will compete with the oxygen/hydrogen evolution reactions making the water decomposition more difficult as was observed in fuel cell research.[227] As a result, the cell working potential can be enlarged. Third, according to the hydrogen evolution reaction (HER) study, it is more difficult to form Ti-H bonds than Fe-H since the former requires higher exchange current to form. Therefore, when Fe_2N is wrapped by Ti_2N, the hydrogen evolution reaction is harder to take place which in other way round will increase the water decomposition voltage. All the above are just our speculations. The increase of working voltage though is still not well explained can be figured out with more specific experimental study and computational work.

The high rate capability is due to the fast ion transport in the electrolyte, fast electrochemical reaction on the nanoarray surfaces, and fast electron transport direct from the nanoarrays down to the carbon current collector.[219] This careful design should benefit the device performance in the following points: first, the core-shell FTN nanoarrays active materials are directly nucleated on the carbon surface thus have a tight connection with the carbon current collector resulting in fast charge transportation of electrons to the substrate. Together with the low electrochemical charge transfer resistance, the high scan rates and high power of the device can be secured. Second, the

Ti_2N shell can preserve the nanorod structure of the core material and help to maintain the entire structure of the core-shell FTN nanorods during long-run cycles. Third, as was discussed in the introduction part, the full substitution of O with N can effectively improve the over-potential of both oxygen and hydrogen evolution reactions. As a result, the whole electrode is more stable in the aqueous electrolyte and ensures a wider working voltage which is the key to the high energy density of our device.

3.2.5 Conclusion

In summary, the as obtained Fe_2N-Ti_2N core-shell nanorods arrays directly grew on carbon cloth substrates in a shape-preserved high temperature ammonia annealing conversion from FeOOH-TiO_2. The as synthesized FTN electrode is proved to be good active material as symmetric supercapacitor device electrode. With the full N substitution from its oxides core-shell source material, the working potential is markedly enlarged duo to the effect of increasing the electrode over-potential of water decomposition. As a result, the FTN core-shell arrays electrodes which are applied as both cathode and anode in the device exhibit excellent electrochemical performance such as high working voltage (2.0 V), fast reaction towards ultrahigh scan rate (50 V s^{-1}), high power density (~ 27 kw kg^{-1}) and extremely high energy density (~ 48 Wh kg^{-1}).

Chapter 4 Summary and Future Work

4.1 Summary of the thesis

In this thesis, basic knowledge of lithium-ion battery and supercapacitor are introduced from the working mechanism, research status, suitable electrode materials and evaluation methods. Examples are given of the synthesis of transition metal oxides/nitrides, their optimization by forming nano-architecture composites with other metal oxides/nitrides or carbon related materials and their related applications in lithium-ion batteries and supercapacitors are discussed.

Metal oxides are usually suitable as anode materials for lithium-ion battery due to their high energy density. Chapter 2 gives two examples of conversion-type LIB anode materials and different optimization methods with other oxides and graphene quantum dots, respectively.

The example of TiO_2 nanotube SnO_2 nanoflake core-branch nanoarrays demonstrate the novelty of provide space for the volume expansion of high-volume-expansion anode material against the traditional way of suppressing the volume expansion and will thus loss the high capacity advantage of these kind of anode material such as Sn and Si related materials. In this case, by providing a highly structural stable bone material, and with a wise selection of materials which have face-preference pairing, the entire design successfully inherits both the structural stability of the low volume expansion material and the high capacity of the high volume expansion material and skillfully avoid the disadvantage of the former by lowering its mass ratio and that of the latter by providing buffering space for its expansion.

The innovative idea of bring graphene quantum dots into lithium-ion battery application to improve both the anode material conductivity and its stability proves to be successful on modifying CuO anode. Comparing to a single metallic Cu enhancement, the GQDs anchoring to the anode surface exhibits longer protection in ultra-long cycles up to even 1000 times. The triaxial structure in the anode

(CuO+Cu+GQDs) delivers higher electrochemical performance in high initial coulombic efficiency, capacity retention in long cycles and rate capability. The metallic Cu and GQDs layer together makes these advantages possible.

While debating still exists regarding the issue that whether metal oxides should be qualified as supercapacitor electrode material due to its trend to show battery performance in low scan speed, metal nitrides stand out ascribe to their higher conductivity and better structural stability. Rectangle shaped CV curves are always the standard sign of a major capacitive behavior. In this consideration, high surface area is always preferred in a supercapacitor device.

By introducing the vertically aligned graphene which grown on conductive carbon as substrate, the new system successfully avoids the stacking problem of the graphene which usually cause the low usage of graphene-related substrate surface. The atomic layer deposition assisted fabrication of the electrode material further secures the fully usage of the substrate surface making the asymmetric device with TiN as cathode and Fe_2N as anode in a solid state electrolyte functions well.

The occasional combination of Fe_2N and Ti_2N which is originally to fabricate nanostructured Fe_2N turns out to be an effective way to form high voltage electrode materials. Though not completely proved, the nitrogen substitution of oxygen in the material is truly efficient in enhance the electrode supercapacitor performance. The core-shell nanorod structure of Fe_2N@Ti_2N reaches as high as 2.0 V in the aqueous symmetric supercapacitor device and makes the whole device stand out among other reported work with the ultra-high energy density. This study also points out the direction to build a high work voltage electrode by going to the opposite orientation of finding good catalyst for the oxygen/hydrogen evolution reaction since bad effect for the ORR and OER means high over-potential against oxygen/hydrogen evolution reactions which makes the aqueous electrolyte based device able to sustain higher working voltage since water decomposition reaction is more difficult to happen in this systems and thus more stable.

The methodology in the first LIB work of forming core-shell by exposure high

capacity material outside as the shell (SnO2) has the advantage of fully take the high capacity of the shell material while in the inner core, the void spaces between the tubes can accommodate the volume expansion during charge-discharge. The disadvantage is this types of structure cannot sustain ultra-long cycling up to 1000 cycles. In the second LIB work, the highly stable GQDs coating can provide long-term cycling up to 1000 cycles but the capacity is limited in this way.

The methodology in first Supercapacitor work is innovative by combing two types of metal nitrides to take advantage of both of them. While the aggregated anode Fe_2N particle is insufficient to reach high capacitance in this case. Thus it is beneath the one in the second Supercapacitor work where Fe_2N nanoarrays can be obtained. Also, this combination of two working window favored materials show another advantage of enlarging the working voltage of the whole device making this work more successful that the first work.

4.2 Future Work

Regarding the future study of nanostructured materials application in energy storage systems, two directions can be considered.

First, searching for energy storage systems that are scarcely touched by nano, mainly some traditional battery systems such as Zn-MnO_2 batteries. The Zn-MnO_2 battery are recently proven to be rechargeable and there is seldom report of nanostructures in this battery application. Work can be done regarding both the anode and cathode. By introducing nano into the metallic Zn anode and MnO_2 cathode. All the nano benefit should be demonstrated in this battery application. Regarding the Zn anode, synthesis method can be direct growth of Zn nanoforest in a conductive substrate or grow ZnO nanostructure first. Method can be hydrothermal, electrodeposition and chemical vapor deposition. Then transfer the ZnO to metallic Zn by annealing in reductive atmosphere like CO/H_2 or by electrochemically discharge the ZnO to Zn. Moreover, carbon substrate such as 3 D graphene nanosheets can be considered as an interesting substrate or promising encapsulates to enhance the Zn anode stability. Regarding the MnO_2 cathode, making the nanoarchitecture is already very mature. Since MnO_2 has mainly four types of phases α, β, γ and δ, attention needs to be paid towards the phase transformation during the battery charge-discharge processes. Raman fitting can be quite useful to differentiate different MnO_2 phases and the reaction products. Furthermore, reaction mechanisms of this battery system can also be an interesting topic. In-situ techniques such as in-situ Raman and in-situ XRD are useful skills to track the materials transferring during battery cycling process.

Second, theoretical work on working voltage determine of supercapacitor electrode material. Now, the way to determine the supercapacitor electrode working potential is normally a trial and error process based on the decomposition voltage of the electrolyte. But after introducing of nano materials, some surprising results usually come up. Worse still, there is no valuation standard for the rationality of the working voltage setting. Several modes are proposed but still the method is not unified. Thus it

is of great importance to explain the working mechanism of the voltage shift and it will be a huge progress if the way to increase working voltage can be concluded. Hopefully, computational calculation can be utilized to figure out the proofs of voltage control.

References

[1] H. Ibrahim, A. Ilinca, J. Perron, Renewable and Sustainable Energy Reviews, 12 (2008) 1221-1250.

[2] F. Rahman, S. Rehman, M.A. Abdul-Majeed, Renewable and Sustainable Energy Reviews, 16 (2012) 274-283.

[3] A.S. Arico, P. Bruce, B. Scrosati, J.-M. Tarascon, W. van Schalkwijk, Nat Mater, 4 (2005) 366-377.

[4] Q. Zhang, E. Uchaker, S.L. Candelaria, G. Cao, Chemical Society Reviews, 42 (2013) 3127-3171.

[5] X. Chen, C. Li, M. Gratzel, R. Kostecki, S.S. Mao, Chemical Society Reviews, 41 (2012) 7909-7937.

[6] L. Dai, D.W. Chang, J.-B. Baek, W. Lu, Small, 8 (2012) 1130-1166.

[7] P.G. Bruce, B. Scrosati, J.-M. Tarascon, Angewandte Chemie International Edition, 47 (2008) 2930-2946.

[8] Y.-G. Guo, J.-S. Hu, L.-J. Wan, Advanced Materials, 20 (2008) 2878-2887.

[9] M.S. Whittingham, MRS Bulletin, 33 (2008) 411-419.

[10] M. Sawangphruk, M. Suksomboon, K. Kongsupornsak, J. Khuntilo, P. Srimuk, Y. Sanguansak, P. Klunbud, P. Suktha, P. Chiochan, Journal of Materials Chemistry A, 1 (2013) 9630-9636.

[11] J. Cheng, B. Zhao, W. Zhang, F. Shi, G. Zheng, D. Zhang, J. Yang, Advanced Functional Materials, 25 (2015) 7381-7391.

[12] X. Li, G. Wang, X. Wang, X. Li, J. Ji, Journal of Materials Chemistry A, 1 (2013) 10103-10106.

[13] C. Zhu, P. Yang, D. Chao, X. Wang, X. Zhang, S. Chen, B.K. Tay, H. Huang, H. Zhang, W. Mai, H.J. Fan, Advanced Materials, 27 (2015) 4566-4571.

[14] H. Wu, G. Zheng, N. Liu, T.J. Carney, Y. Yang, Y. Cui, Nano Letters, 12 (2012) 904-909.

[15] J.-B. Park, K.-H. Lee, Y.-J. Jeon, S.-H. Lim, S.-M. Lee, Electrochimica Acta, 133 (2014) 73-81.

[16] C. Zhu, X. Xia, J. Liu, Z. Fan, D. Chao, H. Zhang, H.J. Fan, Nano Energy, 4 (2014) 105-112.

[17] L. Suo, O. Borodin, T. Gao, M. Olguin, J. Ho, X. Fan, C. Luo, C. Wang, K. Xu, Science, 350 (2015) 938-943.

[18] M.R. Palacín, Chemical Society Reviews, 38 (2009) 2565-2575.

[19] B.E. Conway, Electrochemical Supercapacitors: Scientific Fundamentals and Technological Applications, Kluwer Academic / Plenum, New York, 1999.

[20] V. Augustyn, P. Simon, B. Dunn, Energy Environ. Sci., 7 (2014) 1597-1614.

[21] X. Lu, M. Yu, G. Wang, Y. Tong, Y. Li, Energy Environ. Sci., 7 (2014) 2160-2181.

[22] F. Béguin, E. Frąckowiak, Supercapacitors: Materials, Systems, and Applications, Wiley-VCH Verlag GmbH & Co. KGaA, Weinheim, 2013.

[23] F.C. Krebs, Nat. Mater., 7 (2008) 766-767.

[24] P. Yang, W. Mai, Nano Energy, 8 (2014) 274-290.

[25] A. Du Pasquier, I. Plitz, S. Menocal, G. Amatucci, Journal of Power Sources, 115 (2003) 171-178.

[26] J. Come, V. Augustyn, J.W. Kim, P. Rozier, P.-L. Taberna, P. Gogotsi, J.W. Long, B. Dunn, P. Simon, J. Electrochem. Soc., 161 (2014) A718-A725.

[27] V. Augustyn, J. Come, M.A. Lowe, J.W. Kim, P.-L. Taberna, S.H. Tolbert, H.D. Abruña, P. Simon, B. Dunn, Nat. Mater., 12 (2013) 518-522.

[28] P. Simon, Y. Gogotsi, B. Dunn, Science, 343 (2014) 1210-1211.

[29] C. Zhu, Y. Sun, D. Chao, X. Wang, P. Yang, X. Zhang, H. Huang, H. Zhang, H.J. Fan, Nano Energy, 26 (2016) 1-6.

[30] P. Lu, D. Xue, H. Yang, Y. Liu, International Journal of Smart and Nano Materials, 4 (2012) 2-26.

[31] L.L. Zhang, X.S. Zhao, Chemical Society Reviews, 38 (2009) 2520-2531.
[32] H. Helmholtz, Annalen der Physik, 165 (1853) 211-233.
[33] G. Gouy, J. phys, 9 (1910) 457-467.
[34] D.L. Chapman, The London, Edinburgh, and Dublin philosophical magazine and journal of science, 25 (1913) 475-481.
[35] O. Stern, Z. Elektrochem, 30 (1924) 1014-1020.
[36] M.S. Park, G.X. Wang, Y.M. Kang, D. Wexler, S.X. Dou, H.K. Liu, Angew. Chem. Int. Ed., 46 (2007) 750-753.
[37] X. Xia, D. Chao, X. Qi, Q. Xiong, Y. Zhang, J. Tu, H. Zhang, H.J. Fan, Nano Lett., 13 (2013) 4562-4568.
[38] X. Li, A. Dhanabalan, L. Gu, C. Wang, Adv. Energy Mater., 2 (2012) 238-244.
[39] G. Yu, X. Xie, L. Pan, Z. Bao, Y. Cui, Nano Energy, 2 (2013) 213-234.
[40] S. Zhou, X. Yang, Y. Lin, J. Xie, D. Wang, ACS Nano, 6 (2012) 919-924.
[41] X.W. Lou, Y. Wang, C. Yuan, J.Y. Lee, L.A. Archer, Advanced Materials, 18 (2006) 2325-2329.
[42] Y. Idota, Science, 276 (1997) 1395-1397.
[43] J. Liu, Y. Li, X. Huang, R. Ding, Y. Hu, J. Jiang, L. Liao, J. Mater. Chem., 19 (2009) 1859.
[44] R. Mukherjee, R. Krishnan, T.-M. Lu, N. Koratkar, Nano Energy, 1 (2012) 518-533.
[45] P. Meduri, C. Pendyala, V. Kumar, G.U. Sumanasekera, M.K. Sunkara, Nano Lett., 9 (2009) 612-616.
[46] V. Aravindan, K.B. Jinesh, R.R. Prabhakar, V.S. Kale, S. Madhavi, Nano Energy, 2 (2013) 720-725.
[47] J.S. Chen, L.A. Archer, X. Wen Lou, J. Mater. Chem., 21 (2011) 9912.
[48] L.B. Chen, X.M. Yin, L. Mei, C.C. Li, D.N. Lei, M. Zhang, Q.H. Li, Z. Xu, C.M. Xu, T.H. Wang, Nanotechnology, 23 (2012) 035402.
[49] X. Chen, J. Liang, Z. Zhou, H. Duan, B. Li, Q. Yang, Mater. Res. Bull., 45 (2010) 2006-2011.
[50] J. Lin, Z. Peng, C. Xiang, G. Ruan, Z. Yan, D. Natelson, M.T. James, ACS Nano, 7 (2013) 6001-6006.
[51] Z. Wang, D. Luan, F.Y. Boey, X.W. Lou, J. Am. Chem. Soc., 133 (2011) 4738-4741.
[52] S.J. Ding, J.S. Chen, G.G. Qi, X.N. Duan, Z.Y. Wang, E.P. Giannelis, L.A. Archer, X.W. Lou, J. Am. Chem. Soc., 133 (2011) 21-23.
[53] S.G. Hickey, C. Waurisch, B. Rellinghaus, A. Eychmuller, J. Am. Chem. Soc., 130 (2008) 14978-14980.
[54] X. Hou, X. Wang, B. Liu, Q. Wang, Z. Wang, D. Chen, G. Shen, ChemElectroChem, (2013) n/a-n/a.
[55] Y.-Y. Hu, Z. Liu, K.-W. Nam, O.J. Borkiewicz, J. Cheng, X. Hua, M.T. Dunstan, X. Yu, K.M. Wiaderek, L.-S. Du, K.W. Chapman, P.J. Chupas, X.-Q. Yang, C.P. Grey, Nat Mater, 12 (2013) 1130-1136.
[56] J.-H. Jeun, K.-Y. Park, D.-H. Kim, W.-S. Kim, H.-C. Kim, B.-S. Lee, H. Kim, W.-R. Yu, K. Kang, S.-H. Hong, Nanoscale, 5 (2013) 8480-8483.
[57] G. Ji, B. Ding, Y. Ma, J.Y. Lee, Energy Technology, 1 (2013) 567-572.
[58] J. Lei, W. Li, X. Li, E.J. Cairns, Journal of Materials Chemistry, 22 (2012) 22022-22027.
[59] Y.-M. Lin, R.K. Nagarale, K.C. Klavetter, A. Heller, C.B. Mullins, Journal of Materials Chemistry, 22 (2012) 11134-11139.
[60] Z. Wang, Z.C. Wang, S. Madhavi, X.W. Lou, Chemistry – A European Journal, 18 (2012) 7561-7567.
[61] M. Zhang, Y. Li, E. Uchaker, S. Candelaria, L. Shen, T. Wang, G. Cao, Nano Energy, 2 (2013) 769-778.
[62] J. Zhu, G. Zhang, X. Yu, Q. Li, B. Lu, Z. Xu, Nano Energy, 3 (2014) 80-87.
[63] Y.D. Ko, J.G. Kang, J.G. Park, S. Lee, D.W. Kim, Nanotechnology, 20 (2009) 455701.
[64] S.-Y. Chang, S.-F. Chen, Y.-C. Huang, The Journal of Physical Chemistry C, 115 (2011) 1600-1607.
[65] C. Cheng, H.J. Fan, Nano Today, 7 (2012) 327-343.
[66] D.V. Bavykin, J.M. Friedrich, F.C. Walsh, Advanced Materials, 18 (2006) 2807-2824.
[67] P. Roy, S. Berger, P. Schmuki, Angew. Chem. Int. Ed., 50 (2011) 2904-2939.

[68] H. Wang, D. Ma, X. Huang, Y. Huang, X. Zhang, Sci. Rep., 2 (2012) 701.
[69] Y.C. Qiu, K.Y. Yan, S.H. Yang, L.M. Jin, H. Deng, W.S. Li, ACS Nano, 4 (2010) 6515-6526.
[70] S.-C. Lee, Y.-S. Yang, H.-L. Chen, C.-c. Tsai, C.-S. Chuang, The 4th International Conference on Technological Advances of Thin Films & Surface Coating, (2008).
[71] X. Wu, S. Zhang, L. Wang, Z. Du, H. Fang, Y. Ling, Z. Huang, Journal of Materials Chemistry, 22 (2012) 11151-11158.
[72] Z.Y. Liu, D.D.L. Sun, P. Guo, J.O. Leckie, Nano Lett., 7 (2007) 1081-1085.
[73] Z. Wang, X.W. Lou, Adv. Mater., 24 (2012) 4124-4129.
[74] G. Du, Z. Guo, P. Zhang, Y. Li, M. Chen, D. Wexler, H. Liu, Journal of Materials Chemistry, 20 (2010) 5689-5694.
[75] J.S. Chen, D. Luan, C.M. Li, F.Y.C. Boey, S. Qiao, X.W. Lou, Chemical Communications, 46 (2010) 8252-8254.
[76] J.B. Goodenough, K.-S. Park, J. Am. Chem. Soc., 135 (2013) 1167-1176.
[77] L. Lu, X. Han, J. Li, J. Hua, M. Ouyang, Journal of Power Sources, 226 (2013) 272-288.
[78] C.-M. Park, J.-H. Kim, H. Kim, H.-J. Sohn, Chem Soc Rev, 39 (2010) 3115-3141.
[79] J.M. Tarascon, M. Armand, Nature, 414 (2001) 359-367.
[80] N.S. Choi, Z. Chen, S.A. Freunberger, X. Ji, Y.K. Sun, K. Amine, G. Yushin, L.F. Nazar, J. Cho, P.G. Bruce, Angewandte Chemie, 51 (2012) 9994-10024.
[81] X. Li, C. Wang, Journal of Materials Chemistry A, 1 (2013) 165-182.
[82] L. Ji, Z. Lin, M. Alcoutlabi, X. Zhang, Energy & Environmental Science, 4 (2011) 2682-2699.
[83] X. Wang, D.-M. Tang, H. Li, W. Yi, T. Zhai, Y. Bando, D. Golberg, Chem. Commun., 48 (2012) 4812-4814.
[84] C. Zhang, J. Chen, Y. Zeng, X. Rui, J. Zhu, W. Zhang, C. Xu, T.M. Lim, H.H. Hng, Q. Yan, Nanoscale, 4 (2012) 3718-3724.
[85] R. Wu, X. Qian, F. Yu, H. Liu, K. Zhou, J. Wei, Y. Huang, J. Phys. Chem. A, 1 (2013) 11126-11129.
[86] K. Chen, D. Xue, Phys. Chem. Chem. Phys., 15 (2013) 19708-19714.
[87] D. Liu, Z. Yang, P. Wang, F. Li, D. Wang, D. He, Nanoscale, 5 (2013) 1917-1921.
[88] Z. Yuan, Y. Wang, Y. Qian, RSC Adv., 2 (2012) 8602-8605.
[89] L. Wang, W. Cheng, H. Gong, C. Wang, D. Wang, K. Tang, Y. Qian, J. Mater. Chem., 22 (2012) 11297-11302.
[90] J.Y. Zheng, T.-K. Van, A.U. Pawar, C.W. Kim, Y.S. Kang, RSC Adv., 4 (2014) 18616-18620.
[91] L. Hu, Y. Huang, F. Zhang, Q. Chen, Nanoscale, 5 (2013) 4186-4190.
[92] S. Saadat, J. Zhu, D.H. Sim, H.H. Hng, R. Yazami, Q. Yan, J. Phys. Chem. A, 1 (2013) 8672-8678.
[93] C. Guan, Z. Zeng, X. Li, X. Cao, Y. Fan, X. Xia, G. Pan, H. Zhang, H.J. Fan, Small, 10 (2014) 300-307.
[94] Z. Zhang, R. Dua, L. Zhang, H. Zhu, H. Zhang, P. Wang, ACS Nano, 7 (2013) 1709-1717.
[95] X. Xia, D. Chao, Z. Fan, C. Guan, X. Cao, H. Zhang, H.J. Fan, Nano Lett., 14 (2014) 1651-1658.
[96] D. Chao, X. Xia, J. Liu, Z. Fan, C.F. Ng, J. Lin, H. Zhang, Z.X. Shen, H.J. Fan, Adv. Mater., (2014) 10.1002/adma.201400719.
[97] L. Chen, M. Zhang, W. Wei, J. Nanomater., 2013 (2013) 1-8.
[98] H. Huang, Q. Yu, Y. Ye, P. Wang, L. Zhang, M. Gao, X. Peng, Z. Ye, CrystEngComm, 14 (2012) 7294-7300.
[99] Y. Xu, G. Jian, M.R. Zachariah, C. Wang, J. Mater. Chem. A, 1 (2013) 15486-15490.
[100] Y. Hu, X. Huang, K. Wang, J. Liu, J. Jiang, R. Ding, X. Ji, X. Li, J. Solid State Chem., 183 (2010) 662-667.

[101] X. Chen, N. Zhang, K. Sun, J. Mater. Chem., 22 (2012) 13637-13642.
[102] F. Wang, W. Tao, M. Zhao, M. Xu, S. Yang, Z. Sun, L. Wang, X. Song, J. Alloys Compd., 509 (2011) 9798-9803.
[103] X. Xue, P. Deng, S. Yuan, Y. Nie, B. He, L. Xing, Y. Zhang, Energy Environ. Sci., 6 (2013) 2615.
[104] J.Y. Xiang, J.P. Tu, Y.Q. Qiao, X.L. Wang, J. Zhong, D. Zhang, C.D. Gu, J. Phys. Chem. C, 115 (2011) 2505-2513.
[105] X. Chen, N.Q. Zhang, K.N. Sun, J. Phys. Chem. C, 116 (2012) 21224-21231.
[106] J.Y. Xiang, J.P. Tu, Y.F. Yuan, X.H. Huang, Y. Zhou, L. Zhang, Electrochem. Commun., 11 (2009) 262-265.
[107] M. Bacon, S.J. Bradley, T. Nann, Part. Part. Syst. Charact., 31 (2014) 415-428.
[108] Z. Zhang, J. Zhang, N. Chen, L. Qu, Energy Environ. Sci., 5 (2012) 8869.
[109] W. Liu, X. Yan, J. Chen, Y. Feng, Q. Xue, Nanoscale, 5 (2013) 6053-6062.
[110] M. Dutta, S. Sarkar, T. Ghosh, D. Basak, J. Phys. Chem. C, 116 (2012) 20127-20131.
[111] P. Gao, K. Ding, Y. Wang, K. Ruan, S. Diao, Q. Zhang, B. Sun, J. Jie, J. Phys. Chem. C, 118 (2014) 5164-5171.
[112] J. Tian, H. Zhao, X. Quan, Y. Zhang, H. Yu, S. Chen, Sens. Actuators B: Chem., 196 (2014) 532-538.
[113] X. Zhou, Z. Tian, J. Li, H. Ruan, Y. Ma, Z. Yang, Y. Qu, Nanoscale, 6 (2014) 2603-2607.
[114] A. Ananthanarayanan, X. Wang, P. Routh, B. Sana, S. Lim, D.-H. Kim, K.-H. Lim, J. Li, P. Chen, Adv. Funct. Mater., 24 (2014) 3021-3026.
[115] Y. Li, Y. Hu, Y. Zhao, G. Shi, L. Deng, Y. Hou, L. Qu, Advanced materials, 23 (2011) 776-780.
[116] D. Pan, J. Zhang, Z. Li, M. Wu, Advanced materials, 22 (2010) 734-738.
[117] H. Hagemann, H. Bill, W. sadowski, E. Walker, M. François, Solid State Commun., 73 (1990) 447-451.
[118] H.F. Goldstein, D.-s. Kim, P.Y. Yu, L.C. Bourne, J.P. Chaminade, L. Nganga, Phys. Rev. B, 41 (1990) 7192-7194.
[119] T. Yu, X. Zhao, Z.X. Shen, Y.H. Wu, W.H. Su, J. Cryst. Growth, 268 (2004) 590-595.
[120] M.H. Chou, S.B. Liu, C.Y. Huang, S.Y. Wu, C.L. Cheng, Appl. Surf. Sci., 254 (2008) 7539-7543.
[121] R. Hawaldar, P. Merino, M.R. Correia, I. Bdikin, J. Grácio, J. Méndez, J.A. Martín-Gago, M.K. Singh, Sci. Rep., 2 (2012).
[122] W. Wang, Q. Zhou, X. Fei, Y. He, P. Zhang, G. Zhang, L. Peng, W. Xie, CrystEngComm, 12 (2010) 2232-2237.
[123] D.R. Dreyer, S. Park, C.W. Bielawski, R.S. Ruoff, Chem. Soc. Rev., 39 (2010) 228-240.
[124] D. Yang, A. Velamakanni, G. Bozoklu, S. Park, M. Stoller, R.D. Piner, S. Stankovich, I. Jung, D.A. Field, C.A. Ventrice Jr, R.S. Ruoff, Carbon, 47 (2009) 145-152.
[125] A. Débart, L. Dupont, P. Poizot, J.B. Leriche, J.M. Tarascon, J. Electrochem. Soc., 148 (2001) A1266.
[126] J. Wang, Y. Liu, S. Wang, X. Guo, Y. Liu, J. Mater. Chem. A, 2 (2014) 1224-1229.
[127] C. Zhu, X. Xia, J. Liu, Z. Fan, D. Chao, H. Zhang, H.J. Fan, Nano Energy, 4 (2014) 105-112.
[128] J. Luo, J. Liu, Z. Zeng, C.F. Ng, L. Ma, H. Zhang, J. Lin, Z. Shen, H.J. Fan, Nano Lett., 13 (2013) 6136-6143.
[129] Y.-Y. Hu, Z. Liu, K.-W. Nam, O.J. Borkiewicz, J. Cheng, X. Hua, M.T. Dunstan, X. Yu, K.M. Wiaderek, L.-S. Du, K.W. Chapman, P.J. Chupas, X.-Q. Yang, C.P. Grey, Nat. Mater., 12 (2013) 1130-1136.
[130] C. Peng, H. Chen, Q. Li, W. Cai, Q. Yao, Q. Wu, J. Yang, Y. Yang, J. Mater. Chem. A, 2 (2014) 13859.
[131] Z. Liu, J. Xu, D. Chen, G. Shen, Chem. Soc. Rev., 44 (2015) 161-192.

[132] G. Wang, L. Zhang, J. Zhang, Chem Soc Rev, 41 (2012) 797-828.
[133] D. Yu, Q. Qian, L. Wei, W. Jiang, K. Goh, J. Wei, J. Zhang, Y. Chen, Chem. Soc. Rev., 44 (2015) 647-662.
[134] Z. Yu, L. Tetard, L. Zhai, J. Thomas, Energy Environ. Sci., 8 (2014) 702.
[135] Q. Qu, S. Yang, X. Feng, Adv. Mater., 23 (2011) 5574-5580.
[136] M. Sevilla, A.B. Fuertes, ACS Nano, 8 (2014) 5069.
[137] Y. Shi, L. Pan, B. Liu, Y. Wang, Y. Cui, Z. Bao, G. Yu, J. Mater. Chem. A, 2 (2014) 6086.
[138] T.-W. Lin, C.-S. Dai, K.-C. Hung, Sci. Rep., 4 (2014) 7274.
[139] F. Wang, S. Xiao, Y. Hou, C. Hu, L. Liu, Y. Wu, RSC Advances, 3 (2013) 13059-13084.
[140] J. Yan, Z. Fan, W. Sun, G. Ning, T. Wei, Q. Zhang, R. Zhang, L. Zhi, F. Wei, Adv. Funct. Mater., 22 (2012) 2632-2641.
[141] Z. Fan, J. Yan, T. Wei, L. Zhi, G. Ning, T. Li, F. Wei, Adv. Funct. Mater., 21 (2011) 2366-2375.
[142] P. Tang, Y. Zhao, C. Xu, K. Ni, J. Solid State Electrochem., 17 (2013) 1701-1710.
[143] B. Avasarala, P. Haldar, Electrochim. Acta, 55 (2010) 9024-9034.
[144] I. Milošv, H.H. Strehblow, B. Navinšek, M. Metikoš-Huković, Surf. Interface Anal., 23 (1995) 529-539.
[145] M.-S. Balogun, W. Qiu, W. Wang, P. Fang, X. Lu, Y. Tong, J. Mater. Chem. A, 3 (2015) 1364-1387.
[146] J.H. Chae, K.C. Ng, G.Z. Chen, Proceedings of the Institution of Mechanical Engineers, Part A: Journal of Power and Energy, 224 (2010) 479-503.
[147] M.-S. Balogun, M. Yu, Y. Huang, C. Li, P. Fang, Y. Liu, X. Lu, Y. Tong, Nano Energy, 11 (2015) 348-355.
[148] P. Yu, L. Wang, F. Sun, D. Zhao, C. Tian, L. Zhao, X. Liu, J. Wang, H. Fu, Chemistry – A European Journal, 21 (2015) 3249-3256.
[149] S.A. Al-Thabaiti, R. Hahn, N. Liu, R. Kirchgeorg, S. So, P. Schmuki, S.N. Basahel, S.M. Bawaked, Chem. Commun., 50 (2014) 7960-7963.
[150] C. Shang, S. Dong, S. Wang, D. Xiao, P. Han, X. Wang, L. Gu, G. Cui, ACS Nano, 7 (2013) 5430-5436.
[151] Y. Xiao, G. Zhan, Z. Fu, Z. Pan, C. Xiao, S. Wu, C. Chen, G. Hu, Z. Wei, Electrochim. Acta, 141 (2014) 279-285.
[152] J.H. Bang, K.S. Suslick, Adv. Mater., 21 (2009) 3186-3190.
[153] T.T. Chen, H.P. Liu, Y.J. Wei, I.C. Chang, M.H. Yang, Y.S. Lin, K.L. Chan, H.T. Chiu, C.Y. Lee, Nanoscale, 6 (2014) 5106-5109.
[154] X. Lu, T. Liu, T. Zhai, G. Wang, M. Yu, S. Xie, Y. Ling, C. Liang, Y. Tong, Y. Li, Adv. Energy Mater., 4 (2014) 1300994.
[155] A. Achour, J.B. Ducros, R.L. Porto, M. Boujtita, E. Gautron, L. Le Brizoual, M.A. Djouadi, T. Brousse, Nano Energy, 7 (2014) 104-113.
[156] Z.L. Wang, Nano Today, 5 (2010) 540-552.
[157] F. Grote, H. Zhao, Y. Lei, J. Mater. Chem. A, 3 (2015) 3465-3470.
[158] X. Wang, V. Raju, W. Luo, B. Wang, W.F. Stickle, X. Ji, J. Mater. Chem. A, 2 (2014) 2901-2905.
[159] Y. Yue, P. Han, X. He, K. Zhang, Z. Liu, C. Zhang, S. Dong, L. Gu, G. Cui, J. Mater. Chem., 22 (2012) 4938-4943.
[160] Y. Qiu, K. Yan, S. Yang, L. Jin, H. Deng, W. Li, ACS Nano, 4 (2010) 6515-6526.
[161] F. Tian, Y. Xie, H. Du, Y. Zhou, C. Xia, W. Wang, RSC Adv., 4 (2014) 41856-41863.
[162] Z. Wen, S. Cui, H. Pu, S. Mao, K. Yu, X. Feng, J. Chen, Adv. Mater., 23 (2011) 5445-5450.
[163] M.-S. Balogun, C. Li, Y. Zeng, M. Yu, Q. Wu, M. Wu, X. Lu, Y. Tong, J. Power Sources, 272 (2014) 946-953.

[164] H. Pang, S.J. Ee, Y. Dong, X. Dong, P. Chen, ChemElectroChem, 1 (2014) 1027-1030.
[165] Z. Wang, Z. Li, J. Feng, S. Yan, W. Luo, J. Liu, T. Yu, Z. Zou, Phys. Chem. Chem. Phys., 16 (2014) 8521-8528.
[166] H. Du, Y. Xie, C. Xia, W. Wang, F. Tian, New Journal of Chemistry, 38 (2014) 1284-1293.
[167] C. Xia, Y. Xie, W. Wang, H. Du, Synthetic Metals, 192 (2014) 93-100.
[168] C. Xia, Y. Xie, Y. Wang, W. Wang, H. Du, F. Tian, J. Appl. Electrochem., 43 (2013) 1225-1233.
[169] Y. Xie, H. Du, C. Xia, Microporous Mesoporous Mater., 204 (2015) 163-172.
[170] X.H. Xia, D.L. Chao, Y.Q. Zhang, Z.X. Shen, H.J. Fan, Nano Today, 9 (2014) 785-807.
[171] R. Thomas, G. Mohan Rao, J. Mater. Chem. A, 3 (2014) 274-280.
[172] N. Li, S.X. Jin, Q.Y. Liao, C.X. Wang, ACS Appl. Mater. Interfaces, 6 (2014) 20590-20596.
[173] M. Liu, X. Li, S.K. Karuturi, A.I.Y. Tok, H.J. Fan, Nanoscale, 4 (2012) 1522-1528.
[174] X. Lu, M. Yu, T. Zhai, G. Wang, S. Xie, T. Liu, C. Liang, Y. Tong, Y. Li, Nano Lett., 13 (2013) 2628-2633.
[175] X. Lu, G. Wang, T. Zhai, M. Yu, S. Xie, Y. Ling, C. Liang, Y. Tong, Y. Li, Nano Lett., 12 (2012) 5376-5381.
[176] X. Xiao, X. Peng, H. Jin, T. Li, C. Zhang, B. Gao, B. Hu, K. Huo, J. Zhou, Adv. Mater., 25 (2013) 5091-5097.
[177] J. Liu, Y. Li, H. Fan, Z. Zhu, J. Jiang, R. Ding, Y. Hu, X. Huang, Chemistry of Materials, 22 (2009) 212-217.
[178] J. Liu, Y. Li, H. Fan, Z. Zhu, J. Jiang, R. Ding, Y. Hu, X. Huang, Chemistry of Materials, 22 (2010) 212-217.
[179] Q. Sun, Z.-W. Fu, Electrochem. Solid-State Lett., 11 (2008) A233-A237.
[180] H. Qi, X. Roy, K.E. Shopsowitz, J.K.H. Hui, M.J. MacLachlan, Angewandte Chemie International Edition, 49 (2010) 9740-9743.
[181] X. Lu, M. Yu, G. Wang, T. Zhai, S. Xie, Y. Ling, Y. Tong, Y. Li, Advanced Materials, 25 (2013) 267-272.
[182] X. Lu, G. Wang, T. Zhai, M. Yu, S. Xie, Y. Ling, C. Liang, Y. Tong, Y. Li, Nano letters, 12 (2012) 5376-5381.
[183] X. Lu, M. Yu, T. Zhai, G. Wang, S. Xie, T. Liu, C. Liang, Y. Tong, Y. Li, Nano letters, 13 (2013) 2628-2633.
[184] X. Xiao, T. Ding, L. Yuan, Y. Shen, Q. Zhong, X. Zhang, Y. Cao, B. Hu, T. Zhai, L. Gong, J. Chen, Y. Tong, J. Zhou, Z.L. Wang, Advanced Energy Materials, 2 (2012) 1328-1332.
[185] S.T. Senthilkumar, R. Kalai Selvan, Physical Chemistry Chemical Physics, 16 (2014) 15692-15698.
[186] T.-W. Lin, C.-S. Dai, K.-C. Hung, Sci. Rep., 4 (2014).
[187] P. Sun, Z. Deng, P. Yang, X. Yu, Y. Chen, Z. Liang, H. Meng, W. Xie, S. Tan, W. Mai, Journal of Materials Chemistry A, (2015).
[188] P. Yang, Y. Ding, Z. Lin, Z. Chen, Y. Li, P. Qiang, M. Ebrahimi, W. Mai, C.P. Wong, Z.L. Wang, Nano Letters, 14 (2014) 731-736.
[189] J. Xu, Q. Wang, X. Wang, Q. Xiang, B. Liang, D. Chen, G. Shen, ACS Nano, 7 (2013) 5453-5462.
[190] M.V. Reddy, T. Yu, C.H. Sow, Z.X. Shen, C.T. Lim, G.V. Subba Rao, B.V.R. Chowdari, Advanced Functional Materials, 17 (2007) 2792-2799.
[191] B. Subramanian, C.V. Muraleedharan, R. Ananthakumar, M. Jayachandran, Surface and Coatings Technology, 205 (2011) 5014-5020.
[192] G. Liu, H.G. Yang, X. Wang, L. Cheng, J. Pan, G.Q. Lu, H.-M. Cheng, Journal of the American Chemical Society, 131 (2009) 12868-12869.
[193] G.D. Moon, J.B. Joo, M. Dahl, H. Jung, Y. Yin, Advanced Functional Materials, 24 (2014) 848-856.

[194] V. Augustyn, P. Simon, B. Dunn, Energy & Environmental Science, 7 (2014) 1597-1614.
[195] P. Simon, Y. Gogotsi, Nat Mater, 7 (2008) 845-854.
[196] B.E. Conway, Journal of The Electrochemical Society, 138 (1991) 1539-1548.
[197] M.P. Bichat, E. Raymundo-Piñero, F. Béguin, Carbon, 48 (2010) 4351-4361.
[198] L. Demarconnay, E. Raymundo-Piñero, F. Béguin, Electrochemistry Communications, 12 (2010) 1275-1278.
[199] K. Fic, G. Lota, M. Meller, E. Frackowiak, Energy Environ. Sci., 5 (2012) 5842-5850.
[200] D. Hulicova-Jurcakova, A.M. Puziy, O.I. Poddubnaya, F. Suárez-García, J.M.D. Tascón, G.Q. Lu, Journal of the American Chemical Society, 131 (2009) 5026-5027.
[201] S. Shivakumara, B. Kishore, T.R. Penki, N. Munichandraiah, ECS Electrochemistry Letters, 4 (2015) A87-A89.
[202] Q. Liao, N. Li, S. Jin, G. Yang, C. Wang, ACS Nano, 9 (2015) 5310-5317.
[203] S.L. Candelaria, R. Chen, Y.-H. Jeong, G. Cao, Energy & Environmental Science, 5 (2012) 5619-5637.
[204] P. Hao, Z. Zhao, L. Li, C.-C. Tuan, H. Li, Y. Sang, H. Jiang, C.P. Wong, H. Liu, Nanoscale, 7 (2015) 14401-14412.
[205] A.D. Jagadale, V.S. Kumbhar, D.S. Dhawale, C.D. Lokhande, Electrochimica Acta, 98 (2013) 32-38.
[206] R.S. Kalubarme, H.S. Jadhav, C.-J. Park, Electrochimica Acta, 87 (2013) 457-465.
[207] K. Karthikeyan, D. Kalpana, S. Amaresh, Y.S. Lee, RSC Advances, 2 (2012) 12322-12328.
[208] K. Karthikeyan, D. Kalpana, N.G. Renganathan, Ionics, 15 (2009) 107-110.
[209] H. Xia, Y.S. Meng, G. Yuan, C. Cui, L. Lu, Electrochem. Solid-State Lett., 15 (2012) A60-A63.
[210] H. Xia, B. Li, L. Lu, RSC Advances, 4 (2014) 11111-11114.
[211] D. Weingarth, H. Noh, A. Foelske-Schmitz, A. Wokaun, R. Kötz, Electrochimica Acta, 103 (2013) 119-124.
[212] D. Weingarth, A. Foelske-Schmitz, R. Kötz, Journal of Power Sources, 225 (2013) 84-88.
[213] Y. Wang, J. Cao, Y. Zhou, J.-H. Ouyang, D. Jia, L. Guo, Journal of The Electrochemical Society, 159 (2012) A579-A583.
[214] F. Béguin, K. Szostak, G. Lota, E. Frackowiak, Advanced Materials, 17 (2005) 2380-2384.
[215] D. Hulicova, M. Kodama, H. Hatori, Chemistry of Materials, 18 (2006) 2318-2326.
[216] Y.J. Kim, Y. Abe, T. Yanagiura, K.C. Park, M. Shimizu, T. Iwazaki, S. Nakagawa, M. Endo, M.S. Dresselhaus, Carbon, 45 (2007) 2116-2125.
[217] D. Hulicova, J. Yamashita, Y. Soneda, H. Hatori, M. Kodama, Chemistry of Materials, 17 (2005) 1241-1247.
[218] Y. Zhong, X.H. Xia, F. Shi, J. Zhan, J. Tu, H.J. Fan, Adv. Sci., (2015).
[219] P. Yang, D. Chao, C. Zhu, X. Xia, Y. Zhang, X. Wang, P. Sun, B.K. Tay, Z.X. Shen, W. Mai, H.J. Fan, Adv. Sci., (2015).
[220] Z. Yu, L. Tetard, L. Zhai, J. Thomas, Energy Environ. Sci., 8 (2015) 702-730.
[221] W. Zhou, C. Cheng, J. Liu, Y.Y. Tay, J. Jiang, X. Jia, J. Zhang, H. Gong, H.H. Hng, T. Yu, H.J. Fan, Adv. Funct. Mater., 21 (2011) 2439-2445.
[222] L. Lai, H. Yang, L. Wang, B.K. Teh, J. Zhong, H. Chou, L. Chen, W. Chen, Z. Shen, R.S. Ruoff, J. Lin, ACS Nano, 6 (2012) 5941-5951.
[223] B. Guo, Q. Liu, E. Chen, H. Zhu, L. Fang, J.R. Gong, Nano Lett., 10 (2010) 4975-4980.
[224] L. Lai, J.R. Potts, D. Zhan, L. Wang, C.K. Poh, C. Tang, H. Gong, Z. Shen, J. Lin, R.S. Ruoff, Energy Environ. Sci., 5 (2012) 7936-7942.
[225] H. Wang, T. Maiyalagan, X. Wang, ACS Catalysis, 2 (2012) 781-794.

[226] M. Yang, Y. Zhong, J. Bao, X. Zhou, J. Wei, Z. Zhou, Journal of Materials Chemistry A, 3 (2015) 11387-11394.
[227] J. Sanabria-Chinchilla, K. Asazawa, T. Sakamoto, K. Yamada, H. Tanaka, P. Strasser, Journal of the American Chemical Society, 133 (2011) 5425-5431.